Hydrodynamics and Mass Transfer of Rotating Packed Beds for CO_2 Capture

PENG XIE

A thesis submitted to the University of Sheffield in partial fulfilment of the
requirement for the degree of Doctor of Philosophy

Department of Mechanical Engineering

University of Sheffield

February 2019

Declaration

The candidate confirms that the work submitted is his own, except where work which has formed part of jointly authored publications has been included. The contribution of the candidate and the other authors to this work has been explicitly indicated below. The candidate confirms that appropriate credit has been given within the thesis where reference has been made to the work of others.

The work performed in Chapter 3, Chapter 4 and Chapter 5 of this thesis has been published in *Chemical Engineering Science*. I performed the CFD simulations and drafted the papers. My supervisors, Professor Lin Ma, Professor Derek B. Ingham and Professor Mohammed Pourkashanian provided helpful guidance on my research, helped to revise the paper drafts and supported the publication process. Dr. Xuesong Lu, Dr. Xin Yang and Dr. Hongbing Ding provided helpful support in the CFD simulations and helped the proofreading of my papers published in *Chemical Engineering Science*. All the co-authors have permitted the inclusion of the published papers in the thesis.

Acknowledgements

First and foremost, I am profoundly grateful to my supervisors, Prof. Lin Ma, Prof. Derek B. Ingham and Prof. Mohamed Pourkashanian for their constant guidance, support and encouragement. Prof. Lin Ma provided me with many inspiring advices and gave me enough space for free thinking and exploration. His rigorous academic attitude and approachable style are my models to learn from. Prof. Derek B. Ingham helped me a lot on my research and paperwork with his profound knowledge and great patience. I am encouraged by his diligence, high-efficiency and enthusiasm. Prof. Mohamed Pourkashanian always encouraged me with his kindly smile and words, and supported me to attend academic-related activities. In addition, I would like to thank Dr. Xuesong Lu, Dr. Xin Yang, Dr. Hongbing Ding and Dr. Alastair Clements for their helpful suggestions and full discussions on various scientific issues throughout my PhD studies. I am honoured to spend my doctoral career in such a harmonious, efficient and academically rigorous research group and meet so many colleagues who are passionate about academic researches.

Further, I would like to take this opportunity to express my great gratitude to my parents and grandparents for their upbringing, love and endless support. Their attitude towards life and career inspires me to keep moving forward. I would like to thank all my previous teachers, who taught me knowledge and helped me grow. I would like to thank all my friends around and far away, who make me have a lot of fun in the hard study life.

Last but important, I acknowledge the financial support from the China Scholarship Council and the University of Sheffield for funding my PhD studies.

Publications and presentations

Part of this thesis has been published in the following peer-reviewed journal papers:

Xie P., Lu X., Yang X., Ingham D., Ma L., Pourkashanian M. Characteristics of liquid flow in a rotating packed bed for CO_2 capture: A CFD analysis. *Chemical Engineering Science* 2017; 172: 216-229.

Xie P., Lu X., Ding H., Yang X., Ingham D., Ma L., Pourkashanian M. A mesoscale 3D CFD analysis of the liquid flow in a rotating packed bed. *Chemical Engineering Science* 2019; 199: 528-545.

The author has contribution to the following journal papers:

Lu X., **Xie P.**, Ingham D., Ma L., Pourkashanian M. A porous media model for CFD simulations of gas-liquid two-phase flow in rotating packed beds. *Chemical Engineering Science* 2018; 189: 123-134.

Lu X., **Xie P.**, Ingham D., Ma L., Pourkashanian M. Modelling of CO_2 absorption in a rotating packed bed using an Eulerian porous media approach. *Chemical Engineering Science*; 2019; 199: 302-318.

Ding H., **Xie P.**, Ingham D., Ma L., Pourkashanian M. Flow behaviour of drop and jet modes of a laminar falling film on horizontal tubes. *International Journal of Heat and Mass Transfer*. 2018; 124: 929-942.

Presentations at conferences

Oral presentations:

Xie P., Lu X., Ingham D., Ma L., Pourkashanian M. Mass transfer characteristics of the liquid film flow in a rotating packed bed for CO_2 capture: A microscale CFD analysis. The 9th International Conference on Applied Energy, ICAE2017, 21-24 August 2017, Cardiff, UK

Xie P., Lu X., Ingham D., Ma L., Pourkashanian M. Multiscale CFD modelling and analysis of CO_2 absorption by MEA solutions in a rotating packed bed. The 6th International Conference on CO_2 Emission Control and Utilization, 15-18 June 2018, Hangzhou, China

Poster presentation:

Xie P., Lu X., Ingham D., Ma L., Pourkashanian M. CFD analysis of liquid behaviour in a rotating packed bed: liquid holdup and flow patterns. UKCCSRC Biannual Meeting, 11-12 April 2017, London, UK

Abstract

Post-combustion CO_2 capture (PCC) is an important technology for meeting the greenhouse gas control target. Rotating packed beds (RPBs), as a type of process intensification technology, have been proposed as an emerging technology to be used for PCC from the flue gas, and this is because of its high mass transfer coefficient and compact structure which may lead to energy and space savings. The purpose of this thesis is to investigate the hydrodynamics and mass transfer performance of RPBs for CO_2 capture through using CFD modelling methods. CFD models with different scales are developed to study the hydrodynamics of RPBs, and finally a multiscale modelling method is proposed to predict the performance of large-scale RPBs.

First of all, a 2D VOF-based CFD model with fine grids is built for analysing the characteristics of liquid flow within a laboratory-scale RPB. This model successfully captured the distinct liquid flow patterns in the entrance region and the bulk region of the RPB. The simulation results indicate that increasing the rotational speed dramatically decreases the liquid holdup and increases the degree of the liquid dispersion. Increasing the solvent concentration increases the liquid holdup but the degree of the liquid dispersion decreases.

In addition, a 3D representative elementary unit (REU) based mesoscale CFD model is built, which can be used to investigate the hydrodynamics of RPBs in greater detail and accuracy. The REU is used to study the flow at different locations within an RPB, so that the overall flow characteristics within the RPB can be assembled. The proposed approach enables the detailed prediction of the liquid holdup, droplets formation, effective interfacial area, wetted packing area and specific surface area of the liquid

within real 3D packing structures throughout the bed. Based on the data from the CFD simulations, new correlations to predict the liquid holdup and gas-liquid interfacial area in the RPB are proposed.

Finally, an Eulerian porous media CFD model is developed to analyse the CO_2 absorption by MEA solutions in an RPB. The new porous media model, the gas-liquid drag model, the reactive mass transfer model, the heat transfer model and the interfacial area model are integrated into the Eulerian model, and this model successfully simulates the CO_2 capture from the flue gas by MEA solutions in the RPB. The results obtained show that K_Ga increases significantly with the increasing of the liquid flow rate, MEA concentration, and the liquid inlet temperature, while it only increases slightly with the increasing of the rotational speed and the gas flow rate. In addition, the pressure drop significantly increases with the increasing of the rotational speed and the gas flow rate.

In this thesis, the CFD modelling is realised though using the ANSYS® Fluent software with user-defined functions (UDFs). For the VOF model, the settings of the inlet boundary conditions and the acquisition of the detailed parameters in the calculation domains are achieved through writing UDFs. For the Eulerian model, the specified submodels for RPBs, such as the porous media model, the gas-liquid drag model, the mass transfer model, the interfacial area model, etc. are implemented in ANSYS® Fluent through writing UDFs.

Contents

List of figures

List of tables

Nomenclature

Abbreviations

ANN	Artificial Neural Networks
CCS	Carbon Capture and Storage
CFD	Computational Fluid Dynamics
CSF	Continuum Surface Force
DEA	Diethanolamine
FAM	Finite Analytic Method
FDM	Finite Difference Method
FEM	Finite Element Method
FS	Factor of Safety
FVM	Finite Volume Method
GHG	Green House Gas
IGCC	Integrated Gasification Combined Cycle
IPCC	Intergovernmental Panel on Climate Change
LFR	Liquid Flow Rate
LSR	Least Squares Regression
MEA	Monoethanolamine
MDEA	Methyldiethanolamine
PCC	Post-combustion CO_2 Capture
PFD	Process Flow Diagram
PI	Process Intensification
PIV	Particle Image Velocimetry

ppm	Parts Per Million
RBFNN	Radial Basic Function Neural Network
REU	Representative Elementary Unit
RPB	Rotating Packed Bed
RSM	Reynolds Stress Model
RZB	Rotating Zigzag Bed
SM	Sliding Mesh
SVR	Support Vector Regression
TSNF-RPB	Two-stage Rotating Packed Bed with Nickel Foam Packing
UDF	User-Defined Function
VOF	Volume of Fluid

Roman alphabet

A	entrance area of the REU, m^2
A_e	effective interfacial area, m^{-1}
A_{GL}	gas-liquid interfacial area, m^2
A_{LS}	liquid-solid interfacial area, m^2
A_N	total area of the liquid nozzles in the REU, m^2
A_s	specific surface area of the liquid, m^{-1}
a_s	surface area of the packing per unit volume of the bed, m^{-1}
a_s'	specific area of the wet packing per unit volume of the bed, m^{-1}
A_w	wetted wall area, m^{-1}
C	concentration, $kmol \cdot m^{-3}$
D	diffusivity, $m^2 \cdot s^{-1}$

D_h	hydraulic diameter, m
d	width of the nozzle, m
d_p	equivalent sphere diameter of the wire mesh packing, m
d_w	diameter of the wire, m
d'_w	diameter of the wire and liquid film, m
E	energy, J
$E_{removal}$	CO_2 removal efficiency
E_x	enhancement factor
F_d	volume fraction of the droplets
F_{GL}	drag force between the gas and liquid, $N \cdot m^{-3}$
f	friction factor
f_{app}	Fanning friction factor for laminar flows
f_e	ratio of interfacial area to the packing surface area
f_t	Fanning friction factor for turbulence flows
g	gravitational acceleration, $m \cdot s^{-2}$
g_ω	centrifugal acceleration, $m \cdot s^{-2}$
H	Henry constant, $m^3 \cdot Pa \cdot mol^{-1}$
H_L	enthalpy of the liquid phase, $J \cdot mol^{-1}$
h	thickness of the packed bed, m
$h_{i,k}$	enthalpy of species *k* in phase *i*, $J \cdot mol^{-1}$
h_{GL}	heat transfer coefficient, $W \cdot m^{-2} \cdot K^{-1}$
I_d	liquid dispersion index, m^{-1}
J	diffusion flux of species, $kg \cdot m^{-2} \cdot s^{-1}$

k	curvature of the interface
K_Ga	overall gas phase mass transfer coefficient, $m \cdot s^{-1}$
k_b	reaction rate constant, $m^6 \cdot kmol^{-2} \cdot s^{-1}$
k_{eff}	effective conductivity, $W \cdot m^{-1} \cdot K^{-1}$
k_{GL}	total mass transfer coefficient between gas and liquid, $m \cdot s^{-1}$
k_L*	mass transfer coefficient in the liquid phase from film theory , $m \cdot s^{-1}$
k_i	mass transfer coefficient in the i phase, $m \cdot s^{-1}$
k_{-1}	reaction rate constant, $m^3 \cdot kmol^{-1} \cdot s^{-1}$
k_2	reaction rate constant, $m^3 \cdot kmol^{-1} \cdot s^{-1}$
L	liquid mass flux, $kg \cdot m^{-2} \cdot s^{-1}$
m	exponent of g_ω
$\dot{m}$	mass source, $kg \cdot m^{-3} \cdot s^{-1}$
m_{GL,CO_2}	CO_2 mass transfer between the gas and liquid, $kg \cdot s^{-1}$
M_w	molar mass, $g \cdot mol^{-1}$
N	rotational speed, rpm
n	exponent of ν
$\tilde{n}$	unit normal vector
P	distance metric to the asymptotic range
p	exponent of γ
Q_h	flow rate of enthalpy, W
Q_i	volume flow rate of the *i* phase, $m^3 \cdot s^{-1}$
q_L	volume flow rate of the liquid for feeding the REU, $m^3 \cdot s^{-1}$
q	exponent of U

R	gas constant, 8.314 J·K·mol^{-1}
R_j	net production rate of the *j* species by chemical reactions
R_K	convergence ratio
r	radial position in the RPB, m
r_i	inner radius of the packing region, m
r_o	outer radius of the packing region, m
r_{CO_2-MEA}	reaction rate between CO_2 and MEA
S_h	source of enthalpy, W·m^{-3}
S_i	momentum source, kg·m·s^{-2}
S_{GS}	interaction force between gas and solids, N
S_{LS}	interaction force between liquid and solids, N
S_m	mass source, kg·m^{-3}·s^{-1}
t	time, s
$\bar{t}$	mean residence time, s
T_i	temperature of the *i* phase, K
U	liquid superficial velocity, m·s^{-1}
U_G	grid uncertainty
u_0	liquid inlet velocity, m·s^{-1}
V	volume, m^3
v	velocity, m·s^{-1}
V_d	detached droplets volume in the data source region of the REU, m^3
V_L	liquid volume in the data source region of the REU, m^3
V_p	packing volume of the data source region in the REU, m^3

v_{rel}	relative velocity, m·s^{-1}
x	axial coordinate, m
Y	mass fraction of each species
$y_{CO2,in}$	molar fraction of CO_2 at the gas inlet
$y_{CO2,out}$	molar fraction of CO_2 at the gas outlet
z	tangential coordinate, m

Greek alphabet

α	volume fraction
$\chi+$	dimensionless channel length
γ	contact angle, deg
ℓ	diffusion layer thickness for mass transfer, m
κ	thermal conductivity, W·K^{-1}·s^{-1}
δ	error estimate
δ_{RE}	error estimate from the Richardson extrapolation method
ε	void fraction of packing
ε_i	volume fraction of the *i* phase
ε_L	liquid holdup
μ	dynamic viscosity, Pa.s
ν	kinematic viscosity, mm^2·s^{-1}
θ	angle of flow direction slop to the bed axis, deg
ρ	density, kg·m^{-3}
σ	surface tension coefficient, N·m^{-1}
τ	bed tortuosity factor

ω	angular speed, rad·s^{-1}

Subscripts

exp	experiment
G	Gas phase
i	phase index (=G, L)
j	coordination index (axial, radial or tangential coordinate)
k	species index
L	Liquid phase
r	radial coordinate
rel	relative value
S	solids phase for the packing materials
sim	simulation
w	wall
x	axial coordinate
z	tangential coordinate

Dimensionless Groups

Fr	Froude number
Ga	Galilei number
Ha	Hatta number
Ka	Kapitza number
Nu	Nusselt number
Re	Reynold number
Sc	Schmidt number

Sh	Sherwood number
We	Webber number

Chapter 1: Introduction

Summary

This chapter begins with an introduction of the research background, including CO_2 *emissions and the serious issues of climate change. This is followed by an introduction of the carbon capture and storage (CCS) technologies with a special focus on the post-combustion* CO_2 *capture. Then, the idea of using a rotating packed bed (RPB) as the process intensification equipment for post-combustion* CO_2 *capture is introduced, which is the research objective of this thesis. Also, the research motivation, research aims, novelties, scope and limitations of the thesis and the structure of this thesis are presented.*

1.1 Research background

1.1.1 CO_2 emissions and climate change

According to the *Climate Change 2014: Synthesis Report* provided by the Intergovernmental Panel on Climate Change (IPCC), recent anthropogenic emissions of greenhouse gases (GHG) are the highest in history [1]. Continued emissions of GHG will cause further global warming and increase the likelihood of serious impacts for people and ecosystems [1]. Among all the GHG emitted through human activities, carbon dioxide (CO_2) plays the most important role. The global mean volume fraction of CO_2 in the atmosphere is already over 400 ppm [2]. It is estimated by scientists that atmospheric CO_2 could reach 500 ppm by 2050 and 800 ppm by 2100 if we continue to emit

CO_2 at the current rate. To achieve the goal “limit global warming to less than 2°C relative to pre-industrial levels” set by IPCC requires a 40 to 70% reduction in GHG emissions by the year 2050 [1].

At present, burning fossil fuels such as coal, natural gas and petroleum is the leading cause of increased CO_2 concertation in the atmosphere and power generation is the single largest contributor. Global energy consumption keeps increasing due to the global economic development and population growth [3]. However, due to various immaturities and limitations, depending on renewable energy such as solar, wind and tidal to generate electricity has not been the main pathway in the world. Thermal power plants still account for the majority of the CO_2 emissions [4]. Therefore, taking some effective measures to reduce the CO_2 emission from power plants is very much in demand.

1.1.2 Carbon capture and storage technologies

Carbon Capture and Storage (CCS) is a type of important mitigation technology in which CO_2 from energy and industrial sources is captured, compressed and transported to a storage location for a long term isolation from the atmosphere [5]. These technologies are mainly applied on thermal power plants, or large-scale industrial processes, which have the biggest single CO_2 emission source compared to other CO_2 emission sources, such as vehicles or gas stoves. At present, CCS technologies are in the research and development stage. CO_2 capture, as the first step of the CCS process, is to produce a concentrated stream of CO_2 that can be readily transported to a CO_2 storage location. As shown in Figure 1-1, there are mainly four basic types of CO_2 capture systems for the use of fossil fuels and/or biomass: post-combustion CO_2 capture (PCC), pre-combustion CO_2 capture, oxy-fuel combustion CO_2 capture, and CO_2 capture from industrial process streams [6].

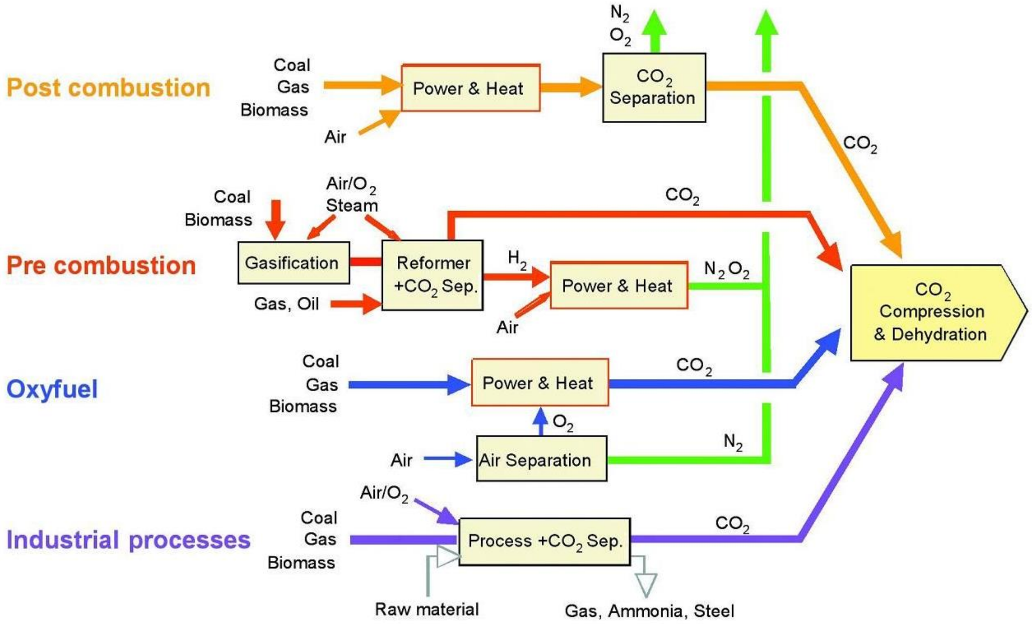

Figure 1-1 Overview of the CO_2 capture processes and systems [6].

Post-combustion CO_2 capture refers to the capture of CO_2 from flue gases produced by combustion of fossil fuels and/or biomass in air. The flue gas is passed through CO_2 separation equipment, which separates most of the CO_2 from the flue gas, and then the CO_2 is transported and fed to a storage reservoir and the remaining flue gas is discharged to the atmosphere. Chemical absorption or physical adsorption processes are normally used for CO_2 separation [6].

Pre-combustion CO_2 capture is usually applied to the Integrated Gasification Combined Cycle (IGCC), where the whole process involves reacting a fuel with oxygen or air and/or steam to generate a syngas composed of carbon monoxide (CO) and hydrogen. The CO is reacted with steam in a catalytic reactor to give CO_2 and more hydrogen, and then CO_2 is separated by a physical or chemical absorption process. This results in a hydrogen-rich fuel which can be used in many applications, such as boilers, gas turbines and engines [7].

Oxy-fuel combustion CO_2 capture is another CO_2 mitigation technology for power stations, where air is replaced by high purity oxygen mixed with recycled flue gases in order to produce a high concentrated CO_2 in the flue gas, which can be directly compressed and transported for storage and/or utilization [8].

Most of the techniques employed for CO_2 capture from process streams, such as production of hydrogen-containing synthesis gas for the manufacture of synthetic liquid fuels, are similar to those used in pre-combustion CO_2 capture. CO_2 could be captured from other industrial process streams, such as cement and steel production, using techniques that are similar to the post-combustion CO_2 capture, oxyfuel combustion CO_2 capture and pre-combustion CO_2 capture [6].

Among the three carbon capture technologies, post-combustion CO_2 capture based on chemical absorption is the most technologically mature and it can be used to retrofit the existing power stations or to be integrated with new power stations. Several large-scale CCS facilities based on the post-combustion CO_2 capture technologies are in operation or under construction [9]. Therefore, it has the potential to be popularized to large-scale power plants around the world in the near future.

1.2 Post-combustion CO_2 capture process

Figure 1-2 shows a simplified traditional PCC process. The emitted flue gas from a CO_2 source, such as a power plant, flows through an absorber, where the flue gas counter-currently contacts with a lean monoethanolamine (MEA) solvent. During the process of contact, the MEA solvent absorbs the CO_2 in the flue gas. After the absorption, the flue gas with a lower CO_2 concertation is exhausted to the atmosphere. The MEA rich solvent is regenerated in the stripper, where pure CO_2 is released from the top of the stripper, and it is compressed and transported for storage or utilization purpose. The regenerated lean MEA solvent is returned to the absorber, passing through a cross exchanger to recover heat with the rich MEA solvent from the absorber.

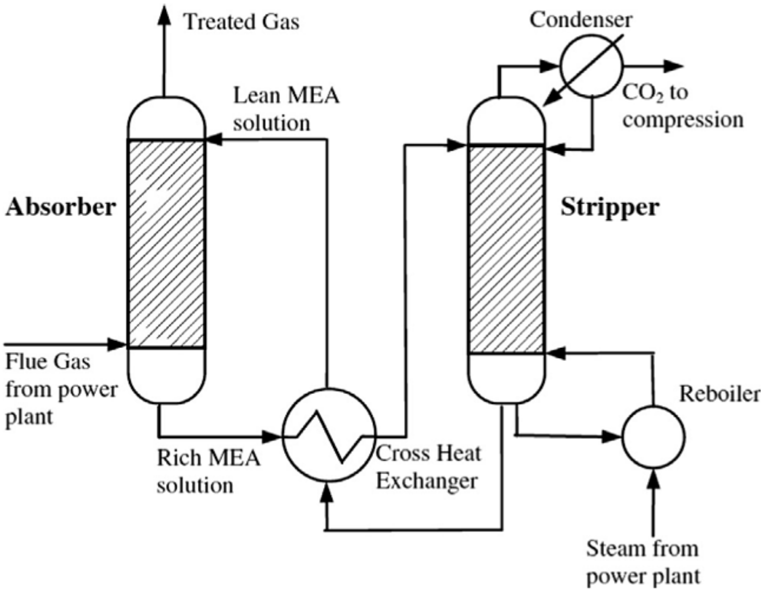

Figure 1-2 Simplified process flow diagram of the chemical absorption process for post-combustion carbon capture [10].

Employing solvent-based PCC for CO_2 mitigation has been shown to be technically feasible, while considerable capital investment and high thermal efficiency penalty due to the solvent regeneration are still the two main barriers for this technology to be extensively employed in commercial power stations [11]. At present, solvent-based PCC processes require very large packed columns to separate CO_2 from the flue gas, this is because the rate of CO_2 capture by amines through the conventional separation technology (i.e. packed columns) is limited by the relatively slow mass transfer process [12]. Lawal et al. [13] performed a dynamic modelling of a typical 500 MWe subcritical coal-fired power plant operating at 46% efficiency (LHV basis), which releases over 8000 tonnes of CO_2 per day. They showed that two absorbers of 17 m in packing height and 9 m in diameter are required to capture CO_2 from the emitted flue gas. These large packed columns result in a high investment in equipment. In addition, a huge amount of steam has to be used to regenerate solvents and this dramatically decreases the overall efficiency of the power generation system [11, 14]. Technical approaches, such as heat integration and inter-cooling of the packed columns, can reduce the operating cost slightly. However, they limit the flexibility of the power plant system and they make the operation and control more difficult [10]. 30 wt% aqueous MEA solution is typically used in the conventional packed columns, while it has been proved that higher concentrated solutions have a greater absorption capacity [15]. As a result, the mass flow rate of the liquid solvent would be reduced; therefore, the equipment size and energy consumption for solvent regeneration would be reduced. However, dealing with the high-concentrated MEA solution with a high viscosity is another challenge for the conventional packed columns, due to the poor liquid dispersion in the packed column. In addition, the corrosivity of the high-concentrated amine solutions require corrosion-resistant materials, such as stainless steel rather than carbon steel as the material of cylinders and internal components, which probably increases the material cost.

1.3 Rotating packed beds for CO_2 capture

In order to overcome the shortcomings of the traditional solvent-based PCC technology, such as the large equipment size and the high energy consumption for solvent regeneration, the process intensification (PI) technology, which aims at achieving a higher energy and space utilization efficiency, has the potential to address these issues successfully. Many PI technologies, including static mixer, spinning disc, micro reactor, rotating packed bed (RPB), etc. have been evaluated for application in CO_2 capture, and finally it was found that the RPB is the most suitable PI technology for CO_2 capture due to its great gas-liquid mass transfer performance [11].

A schematic diagram of a typical RPB is shown in Figure 1-3, and it was initially invented by Ramshaw and Mallinson [16] in 1981 for enhancing the gas–liquid mass transfer in chemical processes. Extensive research have been performed on RPB since the 1980s, and the researches on RPB can be divided into two categories: fundamental research and application research. Fundamental research on RPB mainly includes hydrodynamics research, mass transfer research and micro-mixing research. Application research includes separation process intensification using RPBs, e.g. absorption of CO_2 [17, 18], deoxygenation of water [19], desulfurization [20-25], polymer devolatilization [26], etc., reaction process intensification application using RPBs, e.g. polymerization of isobutylene-isoprene rubber (IIR) [27], diphenylmethane diisocyanate (MDI) production [28], and nanoparticles syntheses [29], etc.

In the application of the RPB for CO_2 capture, the lean amine solvent is radially injected into the packing region from the liquid distributor located at the centre of the bed, and the flue gas can be fed into the bed from the periphery or the centre of the bed to form a counter-current or co-current gas-liquid configuration, respectively. The rotating porous packing generates a high centrifugal field and turns the continuous liquid into thin films and tiny droplets through the shear action, which significantly increases the interfacial area and consequently promotes the absorption of CO_2 from the flue gas [30]. In addition, the high centrifugal field can easily disperse the liquid with a high viscosity, therefore the high-concentrated amine solutions can be employed in this system [30, 31]. This can reduce the ratio of the solvent to the flue gas, and thereby reduce the energy consumption for solvent regeneration.

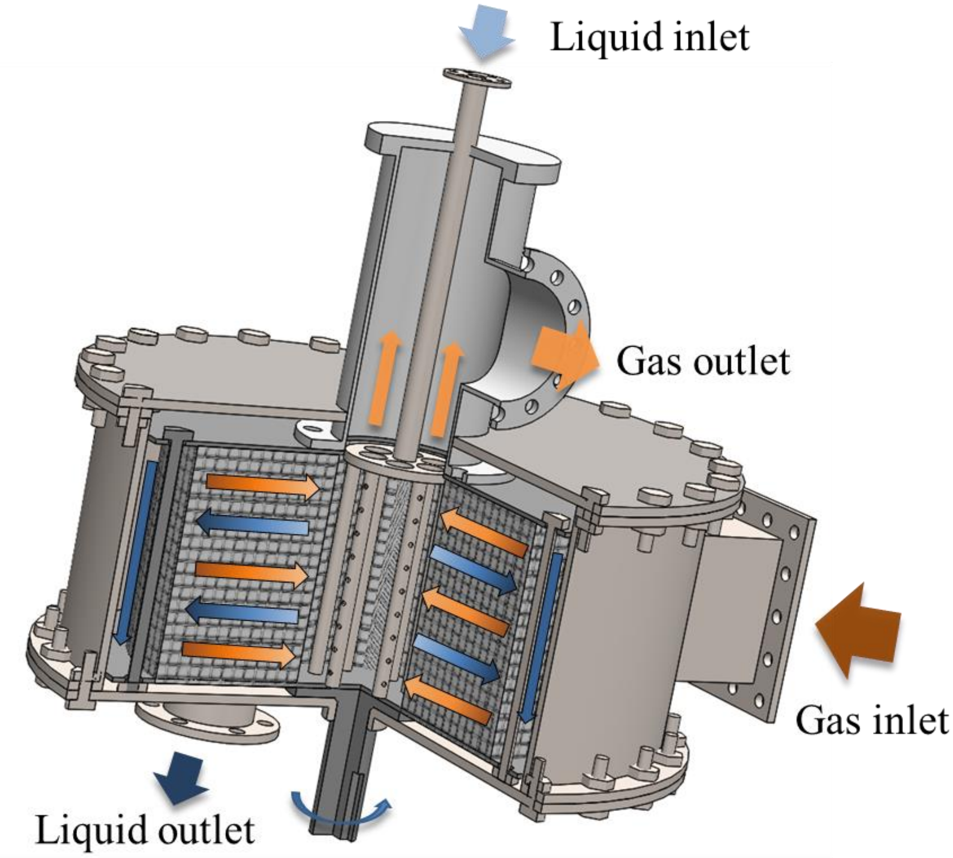

Figure 1-3 Schematic diagram of a typical RPB with a counter-current flow configuration.

Based on the RPB technology, a new process flow diagram (PFD) of the intensified PCC process has been proposed as shown in Figure 1-4 [11]. It was achieved through replacing the traditional CO_2 absorption column and desorption column with the RPB absorber and RPB stripper, respectively. Due to the flow rate of the flue gas from a power plant being very large, special attention should be paid to the design of the large industrial-scale RPBs.

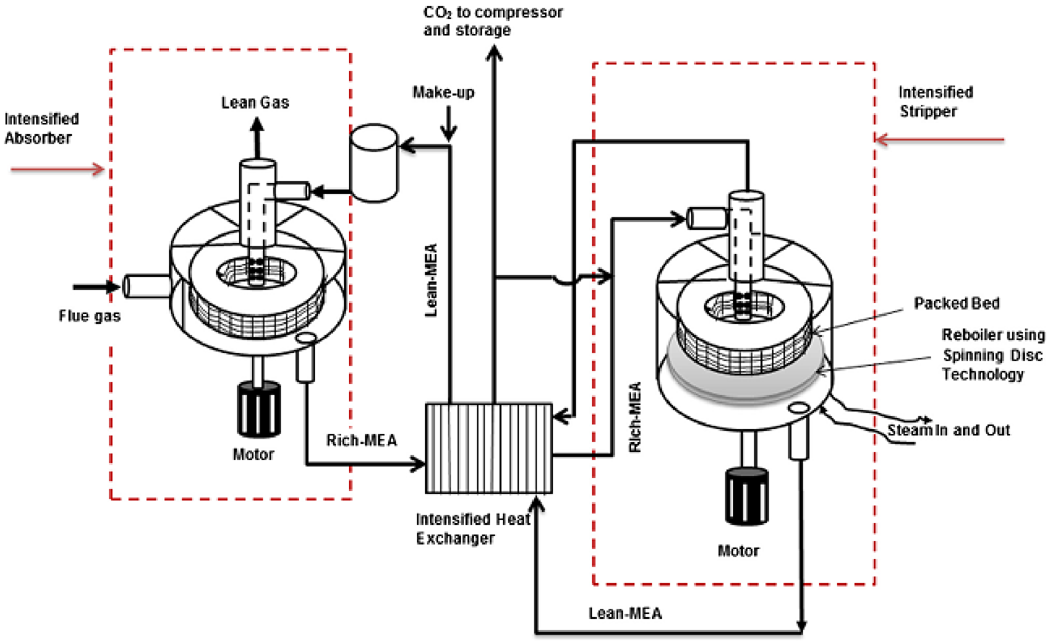

Figure 1-4 Simplified PFD of the intensified chemical absorption process for PCC [11].

At present, a few experimental investigations on CO_2 absorption by different solvents through using RPBs have been performed [31-35], however almost all of these investigations are performed on laboratory-scale RPBs that are far from the actual conditions of CO_2 capture from the massive amount of flue gas. Therefore, the investigation of scale-up design and energy efficiency is insufficient. In addition, based on the modelling and simulation technology, investigations on pilot-scale and industrial-scale RPBs for CO_2 capture have been performed [36-42], and comparisons between the preliminary designed RPBs and packed columns for CO_2 capture have been reported. For example, Agarwal et al. [40] indicated that the equipment volume reduces to 1/7 when using RPBs over conventional packed columns for CO_2 absorption by Diethanolamine (DEA) solutions. Joel et al. [39, 41] indicated that the volume of the absorber reduces to 1/12 and the volume of the regenerator reduces to about 1/10 when replacing the packed columns with the RPBs for CO_2 absorption by MEA solutions. Chamchan et al. [42] concluded that the volume of the intensified CO_2 absorber reduces the volume of the packed column by up to 35% when using the MEA solution. The difference in the volume reduction between the different investigations are due to the different designs, configurations and operational strategies of the employed RPBs for the CO_2 capture. In addition to a volume reduction of the equipment, the overall energy penalty in the CO_2 capture process is another important factor that influences the commercialization process. The energy penalty in the CO_2 capture process mainly includes (i) the thermal energy consumption in the solvent regeneration process, (ii) the consumed electric energy for driving the rotor of the RPB and the liquid cycling pump, and (iii) the kinetic energy loss of the flue gas. In-depth understandings and accurate predictions of the hydrodynamics and mass transfer characteristics of the RPB are necessary to achieve an optimal design of RPBs for the purpose of CO_2 capture.

1.4 Research motivation

In order to achieve the application of RPBs in the PCC process, the optimization design of the RPB for CO_2 capture and the operational strategy need to be carefully considered, and this highly depends on the detailed understanding of the hydrodynamic behaviours and the corresponding mass transfer performance within the RPB. At present, experimental research is the most common way to analyse the hydrodynamics and mass transfer performance of RPBs. Different measuring techniques have been used to measure the fluid dynamics in RPBs, which include (i) non-invasive measuring techniques, such as the high-speed photography [43-45], particle image velocimetry (PIV) [46], X-ray computed tomography [47], and (ii) invasive measuring techniques, such as tracking the liquid trajectories in the RPB by inserting papers [48] or wrapping paper tapes [49]. These experimental methods assist us in forming a better understanding of the liquid behaviour within RPBs. However, from a technical or economic perspective, they are very difficult to be employed for investigating the industrial-scale RPBs for CO_2 capture. In addition, there are still some great challenges for accurately describing the liquid flow in the RPB. In particular: (i) It is very difficult to accurately observe and measure the complex flow in the narrow packing space under high-speed rotational conditions by existing experimental approaches; (ii) It is very difficult to directly measure the gas/liquid and liquid/packing interfacial areas in the RPB with different gas/liquid/packing systems, which impedes the accurate prediction of the mass transfer and the drag force between them; (iii) There is no feasible method to obtain the volume ratio of the droplets to the liquid films at present, thus the flow model is not fully described. In addition, the accurate prediction of the pressure drop and mass transfer performance of RPBs is another challenge, and it is based on the accurate prediction of the hydrodynamic parameters, such as the interfacial areas between the gas, liquid and solids, the liquid residence time, etc.

In addition to the experimental methods, CFD simulations are always powerful tools in increasing the understanding of the hydrodynamics, and obtaining some of the most important parameters that are difficult to be obtained from experiments. In this way, CFD can assist the design of the chemical equipment and guide the operation optimization [8, 50, 51]. In comparison with the experiments, investigations of CO_2 absorption numerically could save the work force, time and material consumptions. Generally, the Volume of Fluid (VOF) method and the Eulerian method are used for modelling the gas-liquid flow dynamics and mass transfers in packed beds.

The transient VOF method is preferable to simulate the detailed gas-liquid hydrodynamic phenomenon, and this is due to the gas-liquid interface being more clearly captured. However, the VOF model requires a very dense computational grid to resolve the detailed structure of the packing and capture the details of the liquid flow in RPBs, and therefore it is very difficult to simulate large scale RPBs due to the limitations of computer resource and calculation time.

The Eulerian method uses a porous media model to express the resistance between the gas or liquid and the packing, and it uses an interfacial area model to estimate the interface between the gas and liquid. Therefore, the Eulerian method does not need to resolve the detailed structures of the packing, and it can simulate the gas-liquid flow through the bed with an appropriate computational grid size and with a low requirement in the computer resources. In addition, the Eulerian method can be used to quantitatively research the CO_2 absorption by the amine solutions in the RPB through incorporating the gas-liquid interfacial area model, mass transfer model, heat transfer model and reaction model.

Therefore, combining the strength of the VOF model and the Eulerian model, CFD methods can be used to research the most important performance aspects of RPBs, such as the liquid holdup, pressure drop, mass transfer, etc. Finally, it can achieve an improvement of the understandings of the hydrodynamics and predictions of the CO_2 absorption in RPBs.

1.5 Thesis structure

1.5.1 Research aims

The research aims of this research are as follows:

- To achieve an in-depth analysis of the hydrodynamics of the RPB for CO_2 capture through using CFD methods. Detailed flow patterns and important hydrodynamic parameters, such as liquid holdup, liquid residence time, gas-liquid interfacial area, etc. are to be investigated, which highly influence the performance of the RPB for CO_2 capture.
- To develop a CFD model in order to achieve an accurate prediction of the CO_2 absorption in pilot-scale and large-scale RPBs. The Eulerian model is the preferred CFD method to achieve this purpose. A comprehensive Eulerian model, which takes into account the flow dynamics, chemical reaction, mass transfer and heat transfer are developed and the effect of the operating parameters on the CO_2 absorption and the pressure drop in the RPB are analysed and discussed in detail.

1.5.2 Novelties

The novelties of this research are as follows:

- A new 2D CFD model with a fine grid has been proposed to investigate the liquid behaviour in an RPB. The bed is simulated in a rotating reference frame and the setting of the liquid inlet boundary condition is achieved through writing UDFs. The model has been verified through comparing the results obtained with the available experimental data and correlations. The simulation results indicate that this CFD modelling method is effective in analysing the detailed liquid flow patterns, the liquid holdup, the liquid residence time as well as the degree of liquid dispersion in an RPB. Both the overall and local liquid flow patterns in the RPB have been analysed and distinct flow patterns have been observed in different packing regions. Because of the acceptable computational accuracy and much smaller amount of computations compared to a 3D model, this method has the potential to be used to analyse the hydrodynamics of an industrial scale RPB.

- A new mesoscale 3D CFD model has been proposed for investigating the hydrodynamic performance of RPBs in greater detail and accuracy, which is based on small 3D representative elementary units (REUs), being implemented at different locations in an RPB. The proposed model enables the prediction of the volume fraction of the droplets, effective interfacial area, wetted packing area and specific surface area of the solvent with a real 3D packing structure throughout the bed. New correlations for predicting the liquid holdup, effective interfacial area, and specific surface area of the solvent in the whole RPB, which are critical for influencing the CO_2 capture, are developed based on the local simulation data.
- A new Eulerian multiphase CFD model has been proposed to predict the gas pressure drop and CO_2 absorption by MEA solutions in the RPB. In this model, the gas-liquid interfacial area is predicted by the interfacial area correlation that is based on the mesoscale 3D simulations. And, a new porous media model which is designed for wire mesh packings is employed to describe the drag force between the gas and packings and the liquid and packings. The porous media model incorporating the reactive mass transfer model and heat transfer model successfully simulates the CO_2 capture process with MEA solutions. Then, the effect of operating parameters and liquid properties on the mass transfer performance and the gas pressure drop in an RPB has been analysed.

1.5.3 Scope and limitation of the thesis

The first part of the research work in this thesis is focused on the analysis of the liquid flow in the RPB through using a 2D CFD model. This model adopts the real round cross-section of the wire mesh as the packing characteristics, and employs a non-uniform grid generation strategy in order to make the model available to capture both the liquid films on the packing surface and the liquid droplets. The effects of the rotational speed, liquid jet velocity, liquid viscosity and contact angle have been investigated in order to obtain an improved understanding of the detailed flow patterns, liquid holdup, liquid residence time, and the degree of liquid dispersion. However, due to the actual 3D wire mesh packings and the 3D droplets not being able to be totally represented in the 2D model, the resistance of the wire mesh packings and the surface tension of the liquid in the 2D model is probably different from that in the actual 3D packings, and this may cause some differences in the CFD predictions from what occurs experimentally.

The second part of the research work in this thesis is concerned with the liquid flow pattern, liquid holdup and interfacial area in RPBs through using a mesoscale 3D CFD model. This method is based on performing many local simulations using small representative elementary units (REUs) being implemented at different locations in an RPB. In this way, the hydrodynamic characteristics of RPBs can be obtained with greater detail and accuracy. Predictions of the volume fraction of the droplets, effective interfacial area, wetted packing area and specific surface area of the solvent with a real 3D packing structure throughout the bed have been achieved. New correlations for predicting the liquid holdup, effective interfacial area, and specific surface area of the solvent in the RPB have been developed based on the local simulation data. In addition, recommendations for scale-up and operation of an RPB for CO_2 capture are provided. However, the liquid flow in the entrance region of the RPB cannot be investigated using this model, and only one type of packing has been investigated in this investigation.

The third part of the research work in this thesis is focused on the simulation of CO_2 absorption by MEA solutions in RPBs. A comprehensive Eulerian CFD model is developed in order to analyse the overall pressure drop and CO_2 absorption in an RPB. The results obtained assist in the design and the operation optimization of the RPB for increasing the overall energy efficiency in the CO_2 capture process. However, this model only considers the CO_2 absorption that occurs in the packing region of the RPB, thus the CO_2 absorption that occurs in the cavity region of the RPB has not been investigated. Therefore, the predicted CO_2 capture efficiency should be lower than the actual CO_2 absorption efficiency. Further improvement of this model, that takes in to account the CO_2 absorption in the cavity zone, should be considered in future investigations.

1.5.4 Outline of the thesis

- In Chapter 1, a general introduction of the research background and motivation of the investigation of the RPB for CO_2 capture through using CFD methods is presented.

- In Chapter 2, a detailed literature review on the hydrodynamics and mass transfer investigations of RPBs is presented, which involves CFD methods.

- In Chapter 3, the theories and methodologies, which are used to achieve the investigation purpose, are described.

- Chapter 4 presents the numerical results and discussion on the 2D CFD analysis of the liquid flow in a small RPB. The effect of the rotating speed, liquid viscosity, and contact angle on the liquid holdup and liquid dispersion are analysed.
- Chapter 5 presents the numerical results and discussion on the 3D mesoscale CFD analysis of the liquid flow in a pilot-scale RPB. Detailed liquid flow patterns, correlations of the liquid holdup and interfacial area are presented.
- Chapter 6 presents the numerical results and discussion on the prediction of the overall CO_2 absorption and gas pressure drop in an RPB.
- In Chapter 7, the key findings and conclusions are presented and some suggestions for the possible future prospects of this thesis are discussed.

Chapter 2: Literature review

Summary

This chapter reviews key aspects of the hydrodynamics and mass transfer investigations of rotating packed beds (RPBs). In order to find the research gaps, the main strategies and challenges in the investigations are presented. For the investigation of the hydrodynamics of RPBs, different experimental measurement methods and prediction models for investigating the liquid flow pattern and important hydrodynamic parameters of the RPB have been reviewed. In addition, different methods for modelling and analysing the mass transfer in RPBs have been reviewed. Further, investigations of the hydrodynamics and mass transfer through using CFD methods are introduced, and the knowledge gas for investigating RPBs using CFD methods is summarized.

2.1 Hydrodynamics of RPBs

Due to the high centrifugal environment created by the high rotational speed of the rotor, the hydrodynamic characteristics of RPBs are much different from the traditional packed beds and any other reactors. The high centrifugal environment leads to a great impact on the gas–liquid mass transfer through changing the hydrodynamics of the RPBs, such as the patterns of the flow, the amount of liquid holdup, the degree of the liquid dispersion, and the effective interfacial area for mass transfer to take place. Therefore, an in-depth understanding of the hydrodynamics of the RPB is essential for understanding the mass transfer performance of the RPB, and it is the basis for accurately establishing the hydrodynamics and mass transfer models. Due to the above reasons, numerous studies on the hydrodynamic characteristics of the RPB have been performed, which include liquid flow patterns, liquid distributions, liquid holdup, liquid residence time, gas pressure drop, etc.

2.1.1 Liquid flow pattern

So far, different experimental methods have been employed to analyse the characteristics of the liquid flow in the RPB. For instance, Burns and Ramshaw [44] and Guo et al. [45] obtained the flow patterns in the packing region of RPBs experimentally by employing a fixed camera and a synchronously rotational video camera with the packing, respectively. As illustrated in Figure 2-1, it is generally believed that there are mainly three flow regimes in the packing region of the RPB, i.e. the pore flow within the packing voids, the discrete droplet flow, and the film flow on the packing surface. In addition, distinct liquid maldistribution is also observed. This indicates that the actual liquid flow within an RPB is very complex and far from being a uniform film flow, which was assumed in some existing mass transfer models for RPBs [52-54].

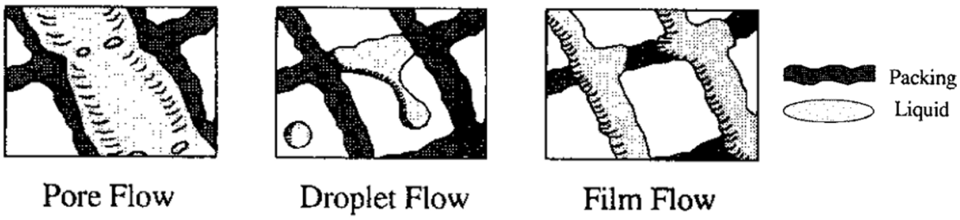

Figure 2-1 Schematic of three types of liquid flows within an RPB [44].

Further, Guo et al. [45] observed different flow patterns between the liquid entrance region and the bulk region of the packing. They have attempted to measure the liquid film thickness on the packing surface of an RPB. However, due to the image speed limitations of the video camera employed, liquid droplets and filaments were difficult to be distinguished from films in the stream across the voids. Yan et al. [48] employed a trajectory tracking method to obtain the liquid flow characteristics in an RPB with random packing. They observed the dynamics of droplets in RPBs, such as droplet–droplet collisions, droplet-packing collisions, deformation and breakup of liquid droplets. This further confirmed the complexity of the flow and they affirmed that there is a certain proportion of turbulence flow even within the liquid film flow. However, this method is only suitable for random packings. Other experimental techniques, such as the visual experimental method have been developed by Guo et al. [49] through observing the ink marks on paper tapes that were wrapped around the packing, in order to investigate the depth of the end-effect zone of the packing in an RPB. In addition to the packing region, the liquid flow pattern in the cavity zone also has been investigated [43]. Due to easier observation of the liquid flow, the criteria of the flow pattern transition has been obtained and the correlation for average droplet diameter has been proposed. However, due to the complexity of liquid flow in the porous packing and the difficulty of its observations, there are still no models that are able to predict the liquid flow pattern in the packing region of RPBs.

2.1.2 Liquid holdup

The liquid holdup (ε_L) of RPBs refers to the rate of liquid volume that is hold in the packing region to the volume of the porous packing region during the running state. It is an important parameter to reflect the resistance of the packing to the liquid in RPBs and it is closely related to the liquid flooding, the pressure drop and the effective interfacial area for mass transfer. Liquid holdup of the RPB is affected by many factors, such as the structure and surface property of the packing, the rotational speed of the bed, the gas velocity, etc. It has been studied by some researchers and several correlations of the liquid holdup of RPBs have been proposed based on experiments, as listed in Table 2-1.

Table 2-1 Correlations for the liquid holdup of RPBs.

Reference	Packing	Correlation for the liquid holdup
Basic and Dudukovic [55]	Glass beads; Voidage: 0.348-0.354	$\varepsilon_L = 2.65\tau_f \left(\frac{a_P d_P}{\varepsilon}\right)^{0.37} Re^{0.67} Ga^{-0.485}$ $Re = U\rho/a_P\mu;$ $Ga = gd_P^3/\nu^2$
Burns et al. (2000) [56]	Reticulated foam; Voidage: 0.953 Specific surface area: 786 m^{-1}	$\varepsilon_L = 0.039 \left(\frac{g}{g_0}\right)^{-0.5} \left(\frac{U}{U_0}\right)^{0.6} \left(\frac{\nu}{\nu_0}\right)^{0.22}$ For water only: $\varepsilon_L = 0.034 \left(\frac{g}{g_0}\right)^{-0.38} \left(\frac{U}{U_0}\right)^{0.62}$ $g_0 = 100\ m/s^2;\ U_0 = 0.01\, m/s;$ $\nu_0 = 10^{-6}\, m^2/s$
Lin et al. (2000) [57]	Plastic grains; Specific surface area: 524 m^2/m^3 -1027 m^2/m^3 Voidage: 0.389-0.533	$\varepsilon_L = 1.2\ Re^{0.545} Ga^{*-0.42} \left(\frac{\alpha_P d_P}{\varepsilon}\right)^{0.65} \varepsilon$ Counter-current: $Ga^* = d_P^3\rho\left(\rho g - \frac{\Delta P}{r_o - r_i}\right)/\mu^2$ Co-current: $Ga^* = d_P^3\rho\left(\rho g + \frac{\Delta P}{r_o - r_i}\right)/\mu^2$
Chen et al. (2004) [58]	Stainless steel wire mesh; Specific surface area: 793-840 m^2/m^3 Voidage: 0.954-0.956	$\varepsilon_L = 21.3u_{L,1}^{0.646} u_{G,2}^{-0.015} \omega^{-0.148}$
Yang et al. (2015) [47]	Wire mesh; 497 m^2/m^3 Voidage: 0.95	For wire mesh packing: $\varepsilon_L = 12.159 Re^{0.923} Ga^{-0.610} Ka^{-0.019}$ For nickel foam packing: $\varepsilon_L = 12.159 Re^{0.479} Ga^{-0.392} Ka^{-0.033}$ $Re = U\rho_L/a_p\,\mu_L\ \ Ga = g{d_p}^3/\nu^2$ $Ka = \mu^4\, g/\sigma^3\rho$
	Nickel foam 1098 m^2/m^3 Voidage: 0.8	

At the early stage, due to the lack of understanding of the liquid flow in RPBs, it is assumed to be only film flow [52, 54]. Based on this assumption, Basic and Dudukovic [55] proposed a theoretical liquid holdup model in analogy with the previous investigations on conventional packed beds [59, 60]. However, they found that the liquid holdup cannot be precisely predicted based on the film flow assumption. Also, they measured the liquid holdup in RPBs using the electrical resistance measurement method, and they proposed a semi-empirical correlation based on the experimental data from RPBs with low porosity glass bead packings [55]. In addition, Burns measured the liquid holdup of an RPB with high porosity packings through using an electrical resistance measurement method and a response time measurement method. Based on the experimental data, Burns [56] proposed two empirical correlations, one of which considered the effect of the operating parameters (g and U) and liquid viscosity (ν), and the other one was only suitable for water. Lin et al. [57] analysed the relationship between the gas pressure drop and the liquid holdup in the RPB, and they proposed a liquid holdup correlation using the pressure drop data. Due to it dependents on the data of pressure drop, this model has a very strong limitation in the practical utilization. Chen et al. [58] came up with a direct method to obtain the liquid holdup in RPBs, which determines the liquid holdup by weighting the amount of retained liquid in the RPB after stopping running. They proposed a correlation and took the influence of the gas flow into consideration; however, it shows that the effect of the gas flow on the liquid holdup is weak. More recently, Yang et al. [47] employed an X-ray CT technique to examine the liquid distribution and liquid holdup in the RPBs with wire mesh packing and nickel foam packing. They developed two correlations for the wire mesh packing and nickel foam packing, respectively. Although experiments can obtain important information, long experimental periods, constrains in the technology and expensive cost limit these methods from being extensively employed for engineering design.

2.1.3 Liquid residence time

Generally, the liquid residence time is an important parameter for determining the application scope of a reactor. For CO_2 absorption, the residence time of the solvent should match well with the mass transfer speed for achieving an optimal design of the RPB. Both direct and indirect measurement methods have been employed to measure the liquid residence time in RPBs. For example, Kenvany and Gardner [61] directly measured the residence time of the liquid in an RPB through using a stimulus-response technology, that is, mounted two sensor probes close to the inner periphery and outer periphery of the bed respectively to detect the time interval of the tracer liquid when it flows through the bed. From their measurements, the mean residence time was between 0.4-1.8 s with different liquid flow rates and rotating speeds. In addition, Guo et al. [45] obtained the liquid residence time through using a similar stimulus-response technology, and they found that the residence time of the liquid in the packing region was between 0.2-0.8 s. As an alternative, Yang et al. [47] indirectly calculated the mean residence time of the liquid in an RPB through using the measured liquid holdup (ε_L), and the calculation equation is as follows:

$$\bar{t} \approx \frac{r_0 - r_1}{U/\varepsilon_L} \tag{2-1}$$

where r_0 is the outer diameter of the packed bed, r_1 is the inner diameter of the packed bed, U is the superficial velocity of the liquid, and ε_L is the liquid holdup. Through using this method, the liquid holdup and the mean residence time can be obtained simultaneously in a measurement. Therefore, the predictions of the mean liquid residence time can be achieved through using the liquid holdup models.

2.1.4 Effective interfacial area

The effective interfacial area (a_e) within the RPB is the gas-liquid interfacial area where the mass transfer occurs. Therefore, it is an important parameter to reflect the mass transfer performance of an RPB. Usually, it is obtained based on the chemical absorption of CO_2 into a NaOH aqueous solution, which is a fast pseudo-first-order reaction system and the kinetics of this system is well-studied [34, 62-67].

In addition, several correlations of the effective interfacial area in RPBs have been proposed, as listed in Table 2-2. Initially, the Onda correlation [68], which is designed for packed columns, has been used to predict the effective interfacial area in RPBs through replacing the gravitational constant g with the centrifugal acceleration $r\omega^2$. In addition, Rajan et al. [63] proposed two correlations to predict the effective interfacial area in an RPB with split Ni-Cr metal foam packings driven by two motors at the co-rotation and current-rotation conditions, respectively. Luo et al. [66] fitted an effective interfacial area correlation using the data from an RPB with a series of stainless steel wire mesh packings. In their correlation, the diameter of the wire mesh and pore size was taken into considered. Further, Luo et al. [69] investigated the effective interfacial area in an RPB with structured stainless steel wire mesh packings, and they fitted a new correlation by including the effect of the gas flow rate on the effective interfacial area.

Table 2-2 Correlations for the effective interfacial area of RPBs.

Reference	Packing	Correlation for the effective interfacial area
Onda et al. (1968) [68]	Raschig rings, Berl saddles, Spheres and rods	$\frac{a}{a_s} = 1 - exp\left[-1.45\left(\frac{\sigma_c}{\sigma}\right)^{0.75} {Re_L}^{0.1}{We_L}^{0.2}{Fr_L}^{-0.05}\right]$ $Re_L = \frac{\rho_L v_L}{a_S \mu_L};\ We_L = \frac{{v_L}^2 \rho_L}{a_S \sigma};\ Fr_L = \frac{{v_L}^2 a_S}{g_\omega};\ g_\omega = r\omega^2.$
Rajan et al. (2011) [63]	split Ni-Cr metal foam	Co-rotation: $\frac{a}{a_s} = 54999 Re_L^{-2.2186} We_L^{1.3160} Fr_L^{-0.1748}$ Counter-rotation: $\frac{a}{a_s} = 11906 Re_L^{-1.8070} We_L^{0.9896} Fr_L^{-0.0601}$ $Re_L = \frac{\rho_L Q_L d_p}{(2\pi rz)\mu_L}; Fr_L = \frac{Q_L^2}{r\omega^2\ (2\pi rh)^2 d_p}; We_L = \frac{Q_L^2 \rho_L d_p}{\sigma\ (2\pi rh)^2}$
Luo et al. (2012) [66]	stainless steel wire mesh	$\frac{a}{a_s} = 66510 Re_L^{-1.41} We_L^{1.21} Fr_L^{-0.12} \varphi^{-0.74}$ $Re_L = \frac{Q_L d_p}{(2\pi rz) v_L}; Fr_L = \frac{Q_L^2}{r\omega^2\ (2\pi rh)^2 d_p}; We_L = \frac{Q_L^2 \rho_L d_p}{\sigma (2\pi rh)^2};$ $\varphi = \frac{c^2}{(c+d)^2}$
Luo et al. (2017) [69]	structured stainless steel wire mesh	$\frac{a}{a_s} = 15.17 Re_G^{0.16} Re_L^{-0.38} We_L^{0.45} Fr_L^{-0.13} \varphi^{-0.29}$ $Re_L = \frac{Q_L d_p}{(2\pi rz) v_L}; Re_G = \frac{Q_G d_p}{(2\pi rz) v_G}; Fr_L = \frac{Q_L^2}{r\omega^2\ (2\pi rh)^2 d_p};$ $We_L = \frac{Q_L^2 \rho_L d_p}{\sigma (2\pi rh)^2}; \varphi = \frac{\emptyset^2}{(\emptyset+d)^2}$

Due to these correlations being derived from a specific RPB and almost all the data used are measured through using the CO_2-NaOH system, the applicability of these correlations to predict the effective interfacial area in different gas-liquid systems has not been verified. For example, using the aqueous MEA solutions of different concentrations to absorb CO_2, the surface tensions and viscosities of the aqueous MEA solutions are different from each other and also they are different from the NaOH aqueous solution. Therefore, the effective interfacial area for these gas-liquid systems may be different from the CO_2-NaOH system in the same RPB reactor. In addition, it is difficult to obtain the effective interfacial area at different radial positions within an RPB by the chemical absorption method.

2.1.5 Gas pressure drop

The gas pressure drop reflects the energy loss of the gas flow in the RPB. Accurately predicting the pressure drop in the RPB is essential for assessing the energy efficiency when adopting the RPB for CO_2 capture. Generally, the pressure drop in an RPB comes from three regions, that is, the gas inlet and casing region (I), the packing region (II), and the gas outlet region (III), as shown in Figure 2-2. Among the three regions, the pressure drop in the packing region is the most difficult to predict due to the complicated flow in the porous packing. There are mainly three reasons that cause the pressure drop: (i) the frictional resistance from the packing and liquid, (ii) the centrifugal force, and (iii) the pressure drop caused by velocity variation induced by the change in cross-sectional area. Investigations show that frictional resistance is the dominant factor for influencing the pressure drop, which accounts for 40–70% of the total pressure drop in a counter-current flow configuration [35]. The second important factor is the centrifugal force, which accounts for 12–20% of the total pressure drop. Therefore, accurate prediction of the frictional resistance in the porous packing is essential.

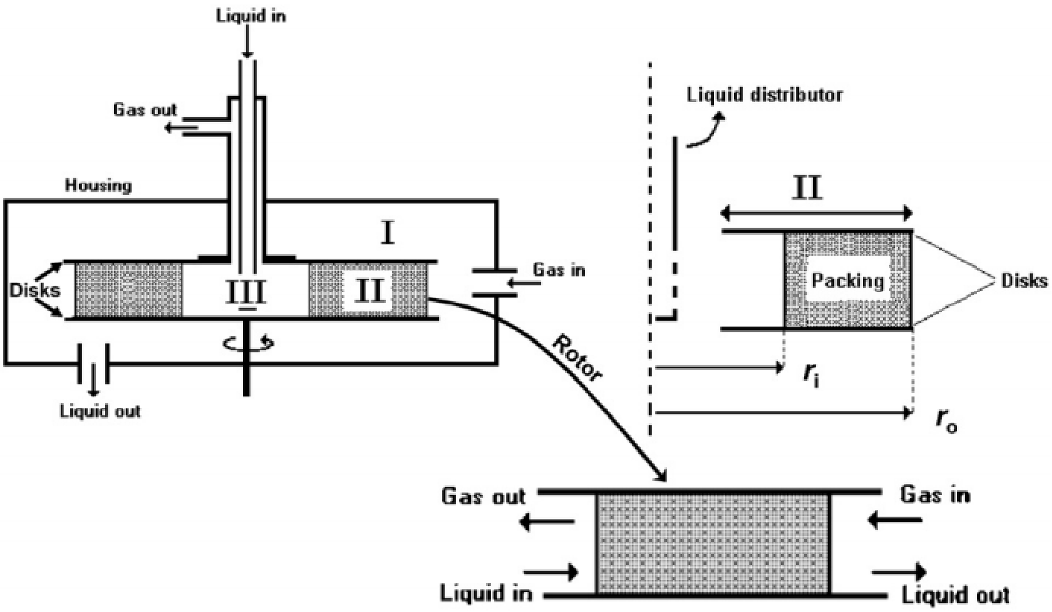

Figure 2-2 Schematic diagram of an RPB and corresponding segmentation [70].

Experimental measurements are the most common way to explore the pressure drop in RPBs. For example, Keyvani and Gardner [61] measured the gas pressure drop in an RPB with aluminum foam packing. Kumar and Rao [54] measured the gas pressure drop in an RPB with wire mesh packing. Liu et al. [71] investigated the effect of the rotational speed, gas flow rate and liquid flow rate on the pressure drop using rectangular and elliptical random packings. The basic consensus is that the pressure drop changes with the rotational speed, gas and liquid flow rate, and it is highly influenced by the packing structure. In addition, different theoretical models [72-74] and semi-empirical correlations [71, 75, 76] have been proposed to describe the gas pressure drop in various RPBs. However, due to each correlation being usually derived from a specific RPB with a fixed structure and dimensions and limited packing materials, the feasibility of these correlations to predict the pressure drop in different RPBs was not verified. CFD simulation is an alternative method to predict the pressure drop in new designed RPBs without using too much cost and time compared with experimental tests [70, 77-79].

2.2 Modelling and analysis of mass transfer in RPBs

Superior gas-liquid mass transfer performance is the prominent advantage of the RPBs compared to the traditional packed columns for CO_2 capture. Generally, the overall gas phase mass transfer coefficient ($K_G a$) and the CO_2 removal efficiency ($E_{removal}$) are used to represent the CO_2 capture efficiency in the RPB and they are calculated as follows:

$$K_G a = \frac{Q_G}{\pi({r_o}^2 - {r_i}^2)h} ln\left(\frac{y_{CO_2,in}}{y_{CO_2,out}}\right) \tag{2-2}$$

$$E_{removal} = \frac{y_{CO_2,in} - y_{CO_2,out}}{y_{CO_2,in}} \times 100\% \tag{2-3}$$

where Q_G is the volumetric flow rate of the feed gas stream (m^3/s), $y_{CO_2,in}$ and $y_{CO_2,out}$ are the mole fraction of CO_2 in the gas inlet and gas outlet, respectively.

Experimental methods have been extensively used to obtain the $K_G a$ of RPBs through measuring the mole fraction of the CO_2 in the gas inlet and gas outlet of the RPBs. For example, Jassim et al. [30] and Lee et al. [31] investigated the CO_2 absorption by MEA solutions in RPBs and the overall gas-phase mass transfer coefficients were obtained and analysed. Sheng et al. [80] systematically investigated the effects of the operation conditions on the CO_2 absorption in an RPB using the diethylenetriamine (DETA) and piperazine (PZ) absorbents. It was found that $K_G a$ may be affected by the liquid flow rate, gas flow rate, L/G ratio, rotational speed, temperature, etc [30, 31, 80]. Different prediction models have been proposed to express the relationships between the influence factors and the overall mass transfer coefficients.

2.2.1 Theoretical models

Modelling and predicting the gas-liquid mass transfer in RPBs is very difficult, and this is mainly due to the difficulties in predicting the effective interfacial area for mass transfer and the local mass transfer coefficient. At present, predictions of the mass transfer are mainly based on the theoretical models and semi-empirical correlations. Usually, the theoretical models are based on the three classical gas-liquid mass transfer theories: two-film theory [81], penetration theory [82], and surface renewal theory [83]. Due to the actual flow in the RPB being very complex, flow simplification hypotheses are usually used for developing the theoretical models. For example, Tung and Mah [52] and Munjal et al. [53] developed gas-liquid mass transfer models based on the penetration theory, and the liquid flows in the RPBs were assumed to be fully developed laminar film flows. Yi et al. [18] developed a mechanism model to predict the CO_2 absorption by a Benfield solution in an RPB, where the liquid is assumed to be in the form of spherical droplets only. These theoretical models as mentioned above can be verified by some special experiments. However, due to the oversimplification of the real flow patterns, physicochemical processes and packing geometries, the applicability and accuracy of these models to predict the mass transfer in different RPBs was not verified.

2.2.2 Semi-empirical correlations

In addition to the theoretically proposed mechanism models, semi-empirical correlation is another popular way to predict the mass transfer coefficient of an RPB. Generally, it was achieved through a statistic regression analysis using the experimental data and the selected influencing parameters. For example, Chen et al. [84] proposed a correlation of $k_L\alpha$ from experimental data with Newtonian and non-Newtonian fluids. Then, they [85] proposed a new correlation to take into account the end effect of the RPB. Jiao et al. [86] correlated the volume mass transfer coefficients with the dimensionless numbers Re_G, We_L, and Ga, which included the effects of the gas flow rate, liquid flow rate, centrifugal acceleration, structure of the packing, surface tension, etc. The semi-empirical correlations do not require rigorous theories, and they do not rely on the detailed description of the liquid flow in the RPB. Therefore, they reduced some of the difficulties in modelling compared with the theoretical models. However, the semi-empirical correlation heavily depend on the experimental data and selected fitting function. Thus, the obtained correlations are difficult to be generalized for different RPBs and/or at different operating conditions.

2.2.3 Intelligent models

With the development of intelligent algorithms, predictions of the mass transfer in RPBs using intelligent models have been proposed in recent years [36, 87, 88]. The intelligent models are trained using the measured data and the selected influencing factors. Artificial neural network (ANN) was the first to be employed to predict the mass transfer coefficient in a physical absorption system [87]. In this model, operating parameters, such as the gas flow rate, liquid flow rate and rotating speed, were used as the independent variables, and the overall gas mass transfer coefficient was used as the dependent variable. In addition, a support vector regression (SVR)-based model has been proposed to predict the CO_2 capture using RPBs [36], and they concluded that the SVR model is better than the multiple nonlinear regression and the ANN models. Essentially, the intelligent model is a data driven-based black-box model and it does not have the theoretical basis of gas-liquid flow, mass transfer and chemical reaction in RPBs. Due to the flow phenomena in different scale RPBs being very different, this method cannot be guaranteed to be used for equipment scaling up.

2.2.4 Mass transfer process analysis

Commercial process modelling softwares, such as gPROMS and Aspen Plus, are very friendly to engineers to perform process analysis. However, due to the immaturity of the RPB mass transfer model, the RPB module has not been integrated into these softwares. However, if we replace the default mass transfer correlations for packed columns with the new developed correlations for RPBs, then these softwares can be used to analyse the mass transfer process in RPBs.

So far, several comprehensive models have been developed to simulate the CO_2 capture in RPBs based on commercial process modelling softwares [38, 41, 89, 90]. For example, Joel et al. [41, 90] modelled the CO_2 absorption by MEA solutions in an RPB absorber using the Aspen Plus rate-based absorber model with its default correlations replaced by new correlations that are suitable for the RPB. The implementation process of this method is shown in Figure 2-3. The new correlations were written in the visual FORTRAN compiler, and they were dynamically linked to the Aspen Plus rate-based model as the subroutines. Similarly, Kang et al. [89] developed a model to analyse the absorption of CO_2 by MEA solutions in an RPB absorber using the gPROMS simulator, and the mass transfer model was based on the two-film theory. Effects of the gas-liquid flow rate and MEA concentration on the CO_2 capture efficiency were analysed.

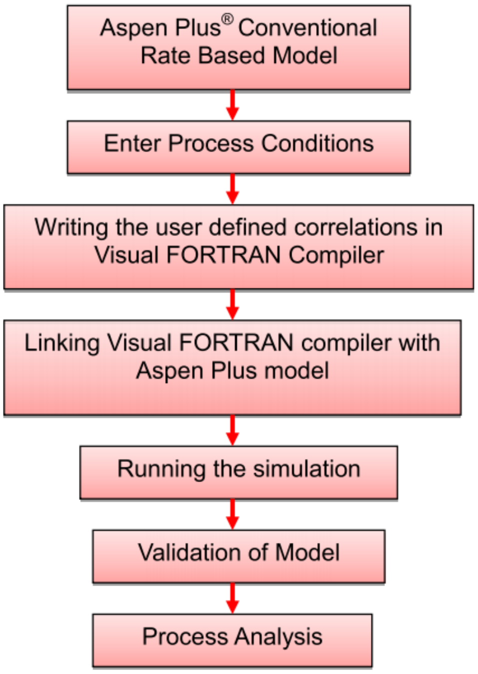

Figure 2-3 Schematic of the methodology used in Joel et al.'s papers [41, 90].

The new developed models include the RPB correlations of the liquid phase mass transfer coefficient, gas phase mass transfer coefficient, interfacial area and liquid holdup. Compared to the correlations of traditional packed columns, these correlations reflect the effect of the centrifugal field that is present in the RPBs. The above-mentioned method is easier to integrate, utilize and generalize the existing correlations for comprehensively predicting and assessing the mass transfer performance of an RPB. Further, the RPB unit model can be connected to other units in the power generation system in order to achieve an overall analysis of the new power plant with the RPB CO_2 capture unit. However, the prediction accuracy of this method heavily depends on the availability and accuracy of the existing correlations. Therefore, the development of reliable correlations is the basis for accurately simulating the mass transfer process using commercial process modelling softwares.

2.3 CFD modelling of RPBs

Difficulties in the prediction of the mass transfer in RPBs are originally from the difficulties in predicting the hydrodynamics in RPBs. Due to both the complicated packing geometry and the centrifugal acceleration, understandings of the gas-liquid flows in the RPB is not enough. Therefore, the flow in the RPB has not been fully described, which limits the development of the mass transfer model. With the development of CFD technology, it has become an effective tool to assist in the understanding of the flow behaviour. In addition, it can be used for the scale up and operation optimization of the chemical reactors. On the one hand, CFD can visually present some detailed flow characteristics on the internals of the chemical equipment, which is often difficult to obtain through experimental measurements [78]. On the other hand, CFD can be used to perform “virtual experiments” at different conditions for obtaining data, which is faster and more economical than experimental methods [51]. However, due to the difficulties that arise from the complex packing structure, the rotational motion and the multiscale flow characteristics, only a few CFD simulations of RPBs have been performed until now. This section demonstrates a review on the CFD modelling of the RPB from single-phase flow to multiphase flows, from hydrodynamic simulations to mass transfer simulations.

2.3.1 Single gas phase flow simulation

Single gas phase flow simulations have been performed, which is the strength of CFD and it is more mature than multiphase flow simulations. For instance, Llerena-Chavez and Larachi [70] and Yang et al. [79] simulated the single gas phase flow in RPBs using three-dimensional (3D) porous media models and the dry pressure drop and gas flow maldistribution in the RPBs were investigated. However, without resolving the packing geometry in the simulation, it is very difficult to obtain the detailed information of the gas flow that is influenced by the structure of the packing. As an improvement, Liu et al. [78] simulated the single-phase flow using the actual 3D wire mesh geometry models. The detailed gas flow inside the RPB was obtained and they observed the gas-side end effect at the outer annular packing region of the RPB. The single-phase simulations provide us the important understanding of the gas flow in the RPB. However, without considering the significant behaviour of the discrete liquid in the RPB, the limitations of these CFD models are clear.

2.3.2 Gas-liquid two-phase flow simulation

2.3.2.1 VOF methods

At present, the CFD modelling of the gas-liquid flow in RPBs mainly focuses on the VOF method, and the wire mesh packing is simplified as small blocks in 2D models or small pillars in 3D models. Although the VOF method has the potential to resolve the details of the droplets and films in RPBs, due to the limitations in the grid generation technology and the number of the grids, currently, the developed CFD models are not able to capture the thin films in the RPB. For example, Shi et al. [91] developed a 2D VOF method to simulate the liquid flow in an RPB. Further, Guo et al. [92] employed the VOF-based method and based on the geometry model of Shi et al. [91] to investigate the micromixing efficiency in the RPB. In these models [91, 92], only the liquid droplets can be observed in the RPB, which is much different from the observed flow patterns in the experiments [44, 45]. This is due to the computational grid in the vicinity of the packing surface being not small enough to capture the thin liquid films. Yang et al. [93] employed the VOF model to analyse the vacuum deaeration process in RPBs. However, due to the coarse computational grids, the gas-liquid interface is difficult to be accurately captured in the RPB. In addition, in the aforementioned VOF-based CFD models [91-93], all the wires used in the wire mesh packing are assumed to have square cross-sections, which is mainly for reducing the difficulty of generating the computational grids. However, in reality, wire meshes having a round cross-section are the most common packing materials. For the wires that directly knock and split the liquid, the cross-section shape has a great influence on the liquid flow characteristics in the RPB. In addition, Guo et al. [94] simulated the liquid flow in an RPB through employing a 3D VOF model, where the wire mesh packing is simplified as small cylinders. Compared to the 2D VOF model, the 3D VOF model is more accurate in simulating the liquid flow in the RPB; however, due to the extremely complexed structure and small scales of the pores in the RPB, it requires an extremely large number of computational grids to resolve the pore structure. Although the VOF method theoretically allows the resolution of the detailed geometry of the RPB, it is very difficult to meet the requirement of performing transient calculations for the full 3D simulation of even laboratory-scale RPB with appropriate accuracy [94]. In summary, although the VOF-based models have achieved some progress in simulating the gas-liquid flows in RPBs, there is still a big space for improving this modelling method to obtain a detailed and accurate prediction of the liquid flow characteristics in RPBs.

2.3.2.2 Eulerian methods

Unlike the VOF model, the Eulerian model does not require very refined grids to resolve the detailed interfaces between the gas, liquid and solid phases, therefore it is suitable for simulating the gas-liquid flow and interphase mass transfer in large-scale packed beds or RPBs. For the Eulerian model, it is very important to employ a suitable porous media model to express the resistance of the packing to the gas and liquid. At present, there are three popular multiphase porous media models: the Attou model [95], based on the spherical packing; the Lappalainen model [96], based on the spherical packing and wettability factor; and the Iliuta model [97], based on the structured packing and wettability factor. These models have been used to develop the Eulerian CFD models in order to simulate the gas-liquid flow and mass transfer in large-scale packed beds [98-100]. However, there are rare numerical simulations of the multiphase flow in RPBs using Eulerian multiphase models. This is because (i) the current available porous media models are not suitable for the wire mesh packings, which are popular packing materials being used in RPBs; (ii) the gas-liquid interfacial area in RPBs is very difficult to be effectively predicted by current models. Recently, Lu et al. [101] proposed a new multiphase porous media model for describing the resistance force between the wire mesh packings and the gas or liquid, which can be employed in CFD models to simulate the gas-liquid flow in RPBs. However, accurate predictions of the gas-liquid interfacial area in the RPB with a particular wire mesh packing is still a challenge. In addition, performing mass transfer, heat transfer and chemical reaction calculations on the basis of the porous media multiphase flow model is still challengeable. All these challenges mush be solved in order to achieve a successful simulation of the CO_2 capture by amine solutions in RPBs.

2.3.3 Multiscale CFD modelling methods

2.3.3.1 Macroscale CFD models

At present, simulating the gas-liquid flow and mass transfer in packed beds through using a porous media model can be considered as the macroscale CFD modelling method. This method does not resolve the geometrical structure of the packing in the packed beds, and therefore it can be used to simulate large-scale packed beds without using too much computing resources. For example, Pham et al. [98] and Asendrych et al. [102] developed a macroscale CFD model to analyse the pressure drop, liquid dispersion and reactive mass transfer in the packed beds. This model can correctly predict the liquid holdup and the concentration of CO_2 in the gas phase along the axial direction of the packed beds. For RPBs, only the dry pressure drops have been simulated through using porous media models [70, 77, 79, 101], which can be considered as the macroscale CFD modelling of the RPBs. However, for gas-liquid two-phase flow in RPBs, the lack of a suitable multiphase porous media model and interfacial area model limits the development of the macroscale multiphase CFD modelling of the RPBs.

2.3.3.2 Microscale CFD models

Microscale modelling of the gas-liquid flow in packed beds focuses on the flow regime near the packing surface using simple and small computational domains. The VOF model is usually used to track the interface between the gas and liquid. In order to obtain detailed flow information, a sufficiently fine mesh has to be applied in the regions where large gradients occurred, for example, an order of magnitude smaller than the thickness of the liquid film is usually required. In fact, such a degree of detail provided by a very refined mesh near the wall could not be attained in the meso- or large-scale domains. In addition, in order to make the main influence factors prominent and save calculation resources, the complex packings can be simplified to some basic geometries while they still can reflect the main features of the packings. For example, corrugated plate packings can be simplified as inclined plane plates [103, 104], inclined plates with surface texture [105, 106], or inclined plates with a bend [107], wetted-wire column can be investigated through a single vertical wire [108, 109], layered wire gauze packing can be investigated by focusing on the wire intersections [110], etc. In this way, the detailed liquid behaviour, such as the formation of wave liquid films, rivulet flows and droplets can be observed, and the important flow parameters, such as the liquid film thickness, liquid holdup can be obtained. In addition, some microcosmic influence factors, such as the geometric texture on the packing surface or different surface properties can be investigated in this scale [103-116].

The analysis of the hydrodynamics at the microscale can be carried out with 2D or 3D simulations. As for a falling liquid film flow, when assuming the flow to be fully developed and no transverse flow occurs, 2D simulations offer the possibility to investigate the flow behaviour. For example, Raynal and Royon-Lebeaud [51] attempted to use 2D microscale VOF models to determine the liquid holdup on structured packings. The influence of the texture patterns on the packing surface can be taken into consideration and the development of the falling liquid film, i.e. velocity profiles and liquid film thickness, can be obtained. The liquid holdup is thus obtained from multiplying the simulated liquid film thickness by the specific area of the packing. This is based on the assumption that a fully developed liquid film covers all the surface of the packing. The 2D simplification used shows an obvious disadvantage because of the oversimplified geometry and flow pattern. Further, 3D models extend the capabilities of the 2D models, thus allowing us to assess the formation of liquid irregularities, such as rivulets and droplets, which strongly influence the magnitude of effective interfacial area on which the mass transfer occurred [103, 104, 106, 112, 113].

In addition, microscale simulations present an adequate technique to implement mass transfer [104, 114, 117]. An implementation of mass transfer using the VOF method allows us to reproduce the concentration profile of a species along the thickness of the liquid film, which provides a higher degree of detail. For example, some attempts have been made by Haroun et al. [114, 117] and Haelssig et al. [118] to describe the reactive mass transfer of a gas species into liquid films. These microscale simulations can save computing resources and assist in obtaining the detailed information of the flow and mass transfer. However, how to relate the microscale models to the actual reactors and use the obtained information to optimise the design of RPB reactors needs serious consideration.

2.3.3.3 Mesoscale CFD models

Mesoscale CFD modelling of a packed bed refers to the CFD simulation of the flow at a scale that is comparable to the dimensions of a typical packing unit [51, 119-123]. The characteristics of the liquid flow in the mesoscale affect both the performance of the microscale mass transfer and overall performance of the RPB, such as the overall pressure drop and the liquid flooding.

At present, the analysis of the dry pressure drop in the packing has been one of the targets of the mesoscale CFD simulations. Due to the structured packings being repeatedly arranged in the PBs, many researchers have used a small number of REUs to calculate the pressure drop per unit length [124-127], then the dry pressure drop in the large-scale PBs can be calculated based on the pressure drop per unit length.

In addition, researchers have implemented the mesoscale CFD modelling of the gas-liquid flow in a structured packing [120] (as shown in Figure 2-4) and wire gauze packing [110], which allows the possibility of visualizing the effect of gravity and surface tension on the formation of the liquid films in actual commercial packing geometries. Further, both the liquid holdup and the interfacial area per unit volume of the packing can be calculated directly. For example, Haroun et al. [113] managed to track the interface between fluids using the VOF method on a metallic sheet of MontzPak B1-250. They reproduced the experimental results concerning the gas-liquid interfacial area and the film thickness in a limited set of REUs of the commercial packing. These investigations constitute a substantial improvement with respect to previous studies at the mesoscale , which focused only on the dry pressure drop.

In the RPB, the packing structure is usually repeatable and the flow is dominated by the packing, which are similar to the packed column. One clear difference is that the centrifugal force changes along the radial direction of the RPB. Therefore, some new strategies should be proposed to perform the mesoscale modelling of the RPB.

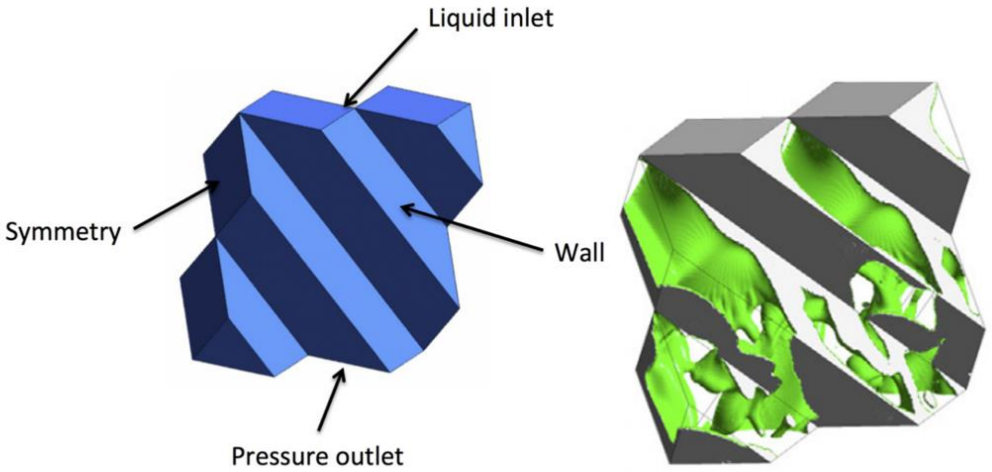

Figure 2-4 Mesoscale CFD simulation of a structure packing: left: boundary conditions right: simulation results [120].

2.3.3.4 Interconnection strategies between different scales

Different scale CFD models have their respective advantages and focus on different issues. In addition, detailed information obtained from a microscale or mesoscale simulation could complement the missing information of the macroscale models. Different multiscale interconnection strategies have been proposed in order to simulate the large-scale packed bed reactors [51, 119, 121, 122]. For example, as shown in Figure 2-5, Raynal and Royon-Lebeaud [51] proposed a three-scale method to predict the pressure drop in a structured packed column. In the microscale model, a 2D computational domain in the range of millimetres was used to obtain the detailed hydrodynamics information by the VOF model, which includes the liquid film thickness, liquid holdup and velocity profiles. In the mesoscale model, single gas-phase simulations were performed in a smallest periodic element, and the wet pressure drop can be estimated through using a correction factor, which takes into account the effect of the liquid. The behaviour of the liquid was obtained from the microscale CFD simulations. Then, in the macroscale CFD model, the entire column geometry was built up by assuming the structured packing as a porous media with the pressure drop characteristics from the mesoscale CFD simulations. The macroscale CFD simulations can be used to investigate the effect of the macroscale geometrical features, such as the liquid distributors and walls, on the entire flow characteristics.

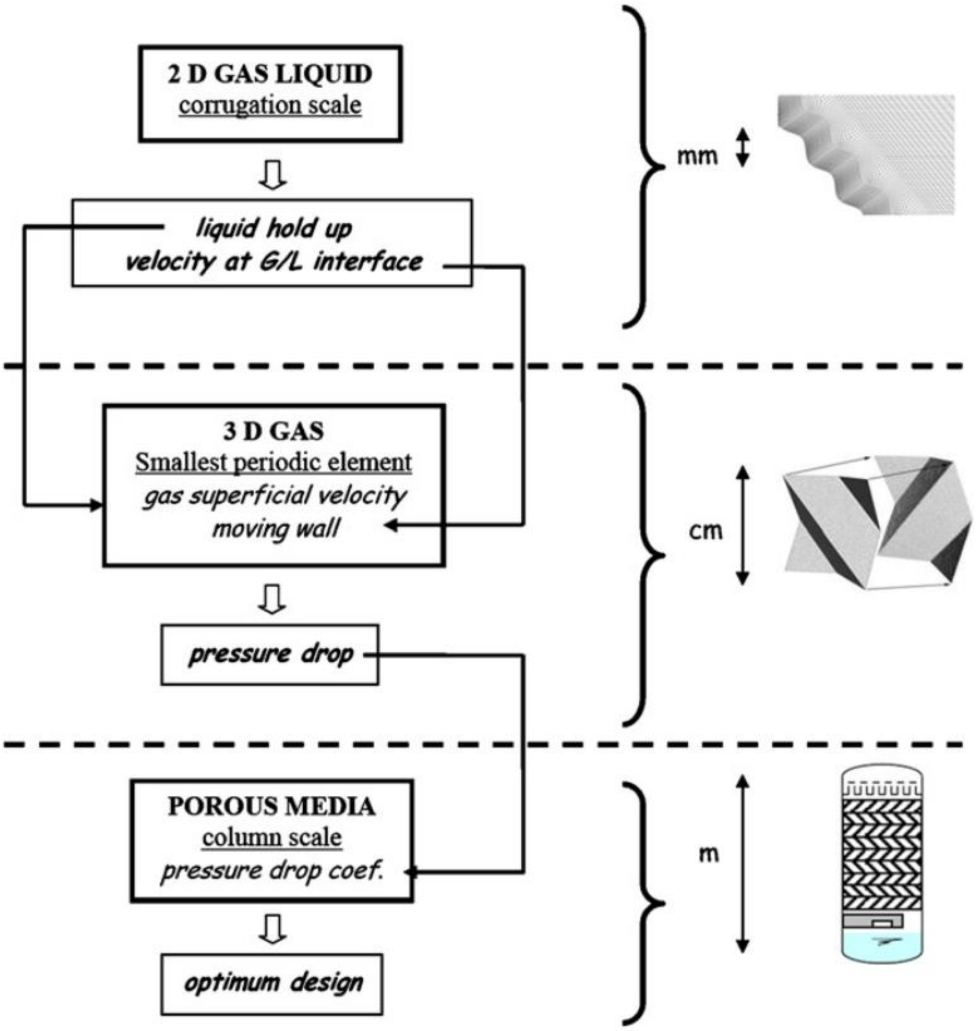

Figure 2-5 Schematic of the three-scale strategy for CFD modelling of a structured packed column [51].

Another example of the interconnection between different scale CFD models has been presented by Li et al. [121], who estimated the liquid holdup in the packed column through multiplying the film thickness and the effective wetting area, which was obtained from the 2D microscale simulation and 3D mesoscale simulation, respectively. Then the obtained liquid holdup was considered in the macroscale simulation using the single gas-phase porous media model, and the effect of the liquid on the pressure drop can be evaluated.

In addition to the pressure drop, the multiscale modelling strategies have been used to predict the overall liquid distribution in packed columns. For example, Sun et al. [119] combined a mesoscale CFD model and a unit network model to analysis the liquid holdup and the liquid distribution in the entire packed column (see Figure 2-6). Then the calculation results can guide the optimum design of the packed column. Similarly, Liu et al. [122] investigated the liquid distribution on a perforated structured packing sheet using a new proposed multiscale model. The effect of the gas flow and openings on the liquid distribution was discussed.

In addition, the multiscale CFD modelling method can be used to investigate the RPB. However, due to the different structure between RPB and PB, new interconnection strategies should be proposed.

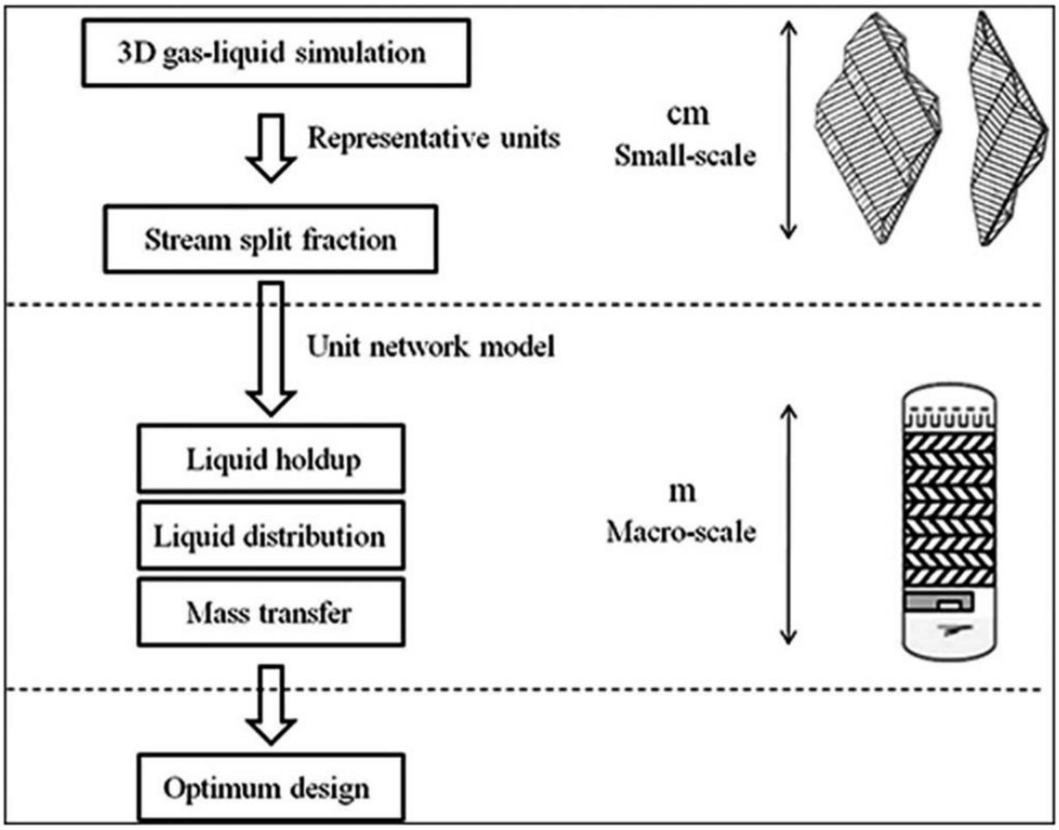

Figure 2-6 The strategy chart of the multiscale method [119].

2.4 Knowledge gaps

Based on the critical review of the state of the art methodologies for investigating the hydrodynamics and mass transfer of the RPBs, some knowledge gaps in the CFD modelling field have been summarized as follows:

(i) Lack of 2D VOF models with good computational grids to accurately resolve the liquid films and droplets in RPBs

The 2D VOF model can be used to effectively obtain some intuitionistic results. However, the existing 2D VOF model of the RPBs cannot capture the thin liquid films on the packing surface of the RPB, and this is mainly due to the computational grids not being fine enough. In addition, all the wires used in the wire mesh packing are assumed to have square cross-sections, which is mainly for reducing the difficulty of generating the computational grids. However, in reality, wire meshes having a round cross-section are the most common packing materials. For the wires that directly knock and split the liquid, the cross-section shape has a large influence on the liquid flow characteristics in the RPB. Therefore, it is difficult to obtain a detailed and accurate prediction of the liquid flow characteristics in an RPB by the existing 2D CFD models. In order to achieve a more reliable prediction of both the formation of the liquid droplet and the formation of the liquid film in the RPB, the quality of the grid should be improved and a real round cross-section of the wire mesh should be used.

(ii) Lack of mesoscale 3D VOF models to analyse the hydrodynamics of RPBs

At present, the existing 3D VOF model of the RPB was based on the simplified packing geometries, which was difficult to analyse the actual hydrodynamics of the RPB. In order to improve the understanding of the real gas/liquid flow in the pores of the packing, detailed and more accurate 3D simulations of the flow in the real geometrical structure of the packing are necessary. However, due to the multiscale issues that have plagued the modelling of the RPB, the multiscale modelling strategy has to be taken into account and the mesoscale 3D modelling of the flow over the packing structure/pores is possible to achieve this purpose.

(iii) Lack of reliable correlations for predicting the interfacial area and liquid holdup in the RPBs

At present, several correlations for the liquid holdup ε_L [47, 55-57] and the effective interfacial area A_e [63, 66, 69] in RPBs have been proposed. These correlations are mainly obtained using mathematical regression based on numerous sets of experimental data from certain RPBs and at certain operating conditions. However, the effect of the contact angle on the hydrodynamic parameters of the RPB has not been considered in the existing correlations. In addition, there are no correlations regressed from RPBs with the expanded stainless steel mesh packing and no correlations that focus on the concentration range of the MEA solutions that are aimed at CO_2 capture. Due to the lack of experimental data at these conditions, generating correlations from CFD simulation data could be an effective and economical alternative to meet the requirement of accurate prediction of the performance of the RPB for CO_2 capture.

(iv) Lack of a multiscale CFD modelling strategy to predict the CO_2 absorption by MEA solutions in RPBs

Inspired by the CFD modelling of the traditional packed beds, a multiscale CFD modelling strategy may be a good choice for RPB simulations. The CFD simulations of post-combustion CO_2 absorption in RPBs requires the combination of the flow, reactive mass transfer and heat transfer models, and the Eulerian method has apparent advantages for the CFD modelling of large or pilot-scale RPBs. For the Eulerian model, the gas-liquid interfacial area requires an extra model, and this can be derived from the CFD simulation of the liquid flow on real wire mesh packings through using a mesoscale VOF model. Therefore, a multiscale model that combines the Eulerian modelling method and the VOF modelling method should be proposed to achieve an accurate prediction of the CO_2 absorption in RPBs.

Chapter 3: Theories and methodologies

Summary

This chapter begins with a brief introduction on the numerical discretization methods for CFD simulations and the CFD modelling methods for simulating the gas-liquid flows. Then the governing equations and submodels in the VOF model and the Eulerian model for simulating the gas-liquid two-phase flows in RPBs are introduced. For investigating the detailed characteristics of the liquid flow in RPBs (Chapter 4 and Chapter 5), the VOF modelling methods are employed. The settings of the inlet boundary conditions and the acquisition of the detailed parameters in the calculation domains are achieved through writing UDFs. For investigating the CO_2 *absorption by MEA solutions (Chapter 6), the Eulerian modelling method is adopted, and the specified submodels for RPBs, such as the porous media model, the gas-liquid drag model, the mass transfer model, the interfacial area model, etc. are implemented in ANSYS® Fluent through writing UDFs.*

3.1 Numerical methods for CFD simulations

CFD applies computing algorithms to solve the governing equations of fluid mechanics, which can be used to obtain the vector and scalar fields such as velocity, pressure, concentration fields, etc. in the calculation domain. Further, these parameters facilitates the analysis of the phenomena that occurs and that are difficult to investigate experimentally. In the last several decades, several numerical methods have been developed for the discretization of the governing equations, such as the finite difference method

(FDM), the finite element method (FEM), the finite analytic method (FAM) and the finite volume method (FVM), etc. Among them, the FVM is the most widely employed method for solving flow, heat transfer and mass transfer problems [128]. Thus in this thesis, the FVM is used for the discretisation of the conservation equations and the commercial CFD software ANSYS® Fluent is used to solve these equations.

3.2 Gas-liquid flow CFD simulation methods

Currently, the Euler-Lagrange and the Euler-Euler approaches are the two most frequent approaches to tackle gas-liquid two-phase flow modelling issues. In the Euler-Lagrange approach, the Navier-Stokes equations are solved for the continuous phase while the dispersed phase is tracked as a number of droplets or bubbles. The mass, momentum and energy can be exchanged between the continuous phase and the dispersed phase [129]. Due to the liquid phase in the RPB being not only discrete droplets, the Euler-Lagrange approach has very strong limitations when it is applied for simulating the gas-liquid flows in an RPB. In the Euler-Euler approach, all the phases are treated as a continua phase. The concept of volume fraction is introduced to represent the components everywhere in the calculation domain. The sum of the volume fractions of all the phases is equal to unity. There are mainly three Euler-Euler models in CFD: the VOF model, the mixture model, and the Eulerian model [129].

At present, the VOF method and the Eulerian method have been used to simulate the gas-liquid flow dynamics in RPBs. The VOF model [130] is a surface-tracking technique, where a single set of momentum equations is shared by the fluids, and the volume fraction of each of the fluids in each computational cell is tracked throughout the domain. This method is used when the tracking of the interface is of interest. The Eulerian model solves a set of mass and momentum conservation equations for each phase and the different phases are coupled through the interface exchange coefficients and the pressure. Applications of the Eulerian multiphase model include bubble columns, risers, particle suspensions, and fluidized beds [129]. Both of the two methods have their own strengths and weaknesses. Some of the main differences in the two methods are as follows:

(i) The clear gas-liquid interface can be tracked by the VOF model and the interfacial area can be obtained based on the tracked interface, whereas the Eulerian model gives a liquid fraction in each unit volume and it requires an interfacial area model to estimate the interfacial area between the gas and liquid. Therefore, the VOF model is usually used to simulate the locally detailed liquid flow on the surface of the packings. However, due to the VOF model requiring a very dense computational grid and a very small time step to capture the transient movement of the droplets and films, it usually cannot simulate the pilot-scale or large-scale RPBs due to the limitations in the computational resources. When using the Eulerian method, the flow in PBs/RPBs can be regarded as being in a pseudo steady state and the steady-state simulation can be performed, therefore much more computational time can be saved compared to transient simulations.

(ii) A single set of momentum equation is solved for both the gas phase and the liquid phase in the VOF method and only the surface tension is considered for the interaction between the gas and liquid. In contrast, the Eulerian model treats the gas and liquid as individual phases, and it requires a porous media model to describe the flow resistance between the gas or liquid and the packing, and a gas-liquid drag force model to describe the gas-liquid drag force.

(iii) For the VOF model, the challenge is the difficulty in meshing the complicated geometry of the packing and the very high demand of the computational resource. For the Eulerian model, the challenge is the accurate description of the complicated gas and liquid flow behaviour in the diverse packing structures. For example, the packing material could be random packings, such as random sphere packings and the random arranged wire mesh packings, or structured packings, such as corrugated packings or structured wire mesh packings. The accurate description of the gas and liquid flow through different packings requires corresponding drag models and interfacial area models, which still require further studies.

(iv) Compared with the VOF method, the Eulerian method is more effective in resources and time when simulating an RPB. Therefore, it is preferable to be used for simulating the CO_2 absorption by liquid amines in pilot-scale or large-scale RPBs.

3.3 VOF method for investigating the hydrodynamics of RPBs

The VOF method, proposed by Hirt and Nichols [130], and the level-set method, proposed by Osher and Sethian [131] are two popular surface-tracking techniques that are used when the tracking of the interface is of much interest. However, the level-set method has a deficiency in the volume or mass non-conservation in the under-resolved regions during the calculation while the VOF method is naturally volume-conserved [129]. In addition, the coupled level-set and VOF approach has been provided in ANSYS® Fluent, however, when adopting this method, the convergence of the continuity equation becomes more difficult than when adopting the VOF method. Therefore, in this thesis, the VOF method is adopted when tracking the gas-liquid interface.

3.3.1 Governing equations

In this thesis, the VOF simulations are performed based on the following assumptions: (i) the two fluids are assumed to be Newtonian and incompressible with no phase change; (ii) the system is under isothermal condition; (iii) the surface tension is constant and uniform at the interface between the two fluids. Based on these assumptions, the governing equations used in the VOF models are illustrated in this section. In the VOF model, a single set of momentum equations are shared by the two fluids, and the volume fraction of each of the fluids in each computational cell is tracked throughout the domain. When solving for the flow within the RPB, it is advantageous to employ a moving reference frame that is fixed on the RPB rotor where the packing remains stationary when viewed from the reference frame, and this makes it easier to analyse the time-sequenced microcosmic liquid transformation process in the RPB. The governing equations of fluid flows in the rotational moving reference frame can be written as follows:

(i) The continuity equation:

$$\frac{\partial}{\partial t}(\alpha_L\rho_L) + \nabla \cdot \left(\alpha_L\rho_L\vec{v}_{rel,L}\right) = 0 \tag{3-1}$$

where L represents the liquid phase, t is the time, α_L is the volume fraction for liquid phase, and $\vec{v}_{rel,L}$ is the relative velocity for liquid phase.

The volume fraction of the gas phase is calculated based on the following constraint:

$$\alpha_G = 1 - \alpha_L \tag{3-2}$$

When the value α_l of a computational cell is equal to zero, it indicates that the cell is full of gas phase, when α_L=1, it means the cell is full of liquid, when 0<α_L<1, the cell contains the gas-liquid interface. The interface is reconstructed by the Geometric-Reconstruction scheme [132], which uses a piecewise-linear approach to represent the interface between the fluids.

(ii) The momentum conservation equation:

$$\frac{\partial}{\partial t}(\rho\vec{v}_{rel}) + \nabla\cdot(\rho\vec{v}_{rel}\vec{v}_{rel}) + \rho(2\vec{\omega}\times\vec{v}_{rel} + \vec{\omega}\times\vec{\omega}\times\vec{r}) \\ = -\nabla p + \nabla\cdot\left[\mu\left(\nabla\vec{v}_{rel} + \nabla\vec{v}_{rel}{}^{T}\right)\right] + \vec{F}_{vol} \tag{3-3}$$

where $(2\vec{\omega}\times\vec{v}_{rel})$ and $(\vec{\omega}\times\vec{\omega}\times\vec{r})$ are the Coriolis acceleration and the centripetal acceleration, respectively.

The fluid properties, such as density ρ and dynamic viscosity μ, take volume-averaged values as follows:

$$\rho = \alpha_L\rho_L + (1-\alpha_L)\rho_G \tag{3-4}$$

$$\mu = \alpha_L\mu_L + (1-\alpha_L)\mu_G \tag{3-5}$$

3.3.2 Surface tension and wall adhesion

The surface tension has a significant impact on the liquid dispersion. In this thesis, the CSF (Continuum Surface Force) model proposed by Brackbill et al. [133] is employed to account for the effect of the surface tension, i.e. the surface tension force is transformed to a volume force source term F_{vol} in the momentum equations. The localised volume force F_{vol} can be estimated using the following relationship:

$$F_{vol} = \sigma\frac{\rho k\nabla\alpha_L}{0.5(\rho_L+\rho_G)} \tag{3-6}$$

where σ is the surface tension coefficient, k is the gas-liquid interface curvature and it is defined in terms of the divergence of the unit normal ñ and it is given as

$$k = \nabla \cdot \tilde{n} \tag{3-7}$$

where ñ= $n/|n|$ and $n = \nabla \alpha_L$.

The effect of the contact angle between the fluid and the wall is established within the framework of the CSF model [133] by changing the unit surface normal at the grid next to the wall, which is calculated by the following equation:

$$\tilde{n} = \tilde{n}_w \cos\theta_w + \tilde{m}_w \sin\theta_w \tag{3-8}$$

where $\tilde{n}_w$ and $\tilde{m}_w$ are the unit vectors normal and tangential to the wall, respectively, and θ_w is the contact angle.

3.3.3 Turbulence model

The employment of an appropriate turbulence model is essential for achieving an accurate simulation and different turbulence models have respective adaptability. The two-phase flow in an RPB can be turbulent depending on the packings and the rate of the fluid flow. However, the presence of the packings can have a significant damping effect on the turbulence. The liquid film flow within the boundary layers of the packing surfaces develop from being laminar flow to being fully developed turbulence flow depending the location and thickness of the film and thus can be partially turbulent [134], and the Reynolds number based on the size of the pore/wire is usually low. However, in the vicinity of the liquid entrance region and in the cavity region, the Reynolds number is higher. Shi et al. [91] selected the most elaborate type of turbulence model: the Reynolds stress model (RSM) for the closure of the Reynolds-averaged Navier-Stokes equations. However, in this model, five and seven additional equations should be solved in a 2D and 3D calculation domain, respectively. This substantially increases the calculation time and requires more computational memory. Therefore, several two-equation eddy-viscosity turbulence models, including the standard, shear-stress transport (SST) k-ω models and the standard, RNG, realizable k-ε models with enhanced wall functions, have been tested for seeking the potential to simulate the liquid flow in the RPB. According to the simulation results, when adopting the standard or SST k-ω model, the liquid holdup is within only 5% from that obtained using the RSM model. When adopting the standard k-ε model and its variations, the liquid holdup is always less than when adopting the RSM or k-ω models with an error of about 10%. The SST k-ω model in ANSYS® Fluent incorporates modifications for low-Reynolds number effects. Therefore, in this thesis, the SST k-ω model [135] is adopted in the VOF simulations. It is worth mentioning that the turbulence modelling in packed materials is currently still a topic of much ongoing research.

3.3.4 Solvents properties adopted in the VOF simulations

Aqueous monoethanolamine (MEA) solution is one of the typical absorbents for CO_2 capture, and 30 wt% aqueous MEA solution is normally used in the packed columns for CO_2 capture. Previous investigations showed that increasing the concentration of the MEA solution can greatly increase the CO_2 absorption capacity [30] and reduce the absorbent's regeneration energy [136]. The RPB has the advantage of being able to deal with a highly concentrated MEA solution than packed columns because of the strong centrifugal field that can break the liquid and significantly increase the specific surface area of the solvent [84]. Therefore, simulations are performed with a variety of aqueous MEA solutions with the concentration from 30 wt% to 90 wt%. In addition, for the model validation, water and glycerol are also adopted. The properties of the solvents used for the CFD simulations are shown in Table 3-1. The MEA is assumed to operate at a constant temperature of 40 ^{o}C, which is close to the real operation conditions of a CO_2 absorber employed for PCC.

Table 3-1 Physical properties of the solvents used for the CFD simulations. [a]

Solvent	Density (kg/m^3)	Dynamic Viscosity (Pa.s)	Kinetic viscosity (mm^2/s)	Surface tension (N/m)
Water	998.2	0.001003	1.00	0.0728
30 wt% MEA [137]	1003.4	0.00167	1.66	0.05352
50 wt% MEA [137]	1011.7	0.00339	3.35	0.05069
70 wt% MEA [137]	1015.5	0.00696	6.85	0.04888
90 wt% MEA [137]	1008.4	0.0102	10.12	0.04725
60 wt% glycerol [47]	1140.0	0.00938	8.23	0.0669
70 wt% glycerol [47]	1172.95	0.0185	15.77	0.0665
80 wt% glycerol [47]	1213.60	0.0558	45.98	0.0657

[a] The properties of the aqueous MEA solutions are at 40 °C.

3.4 Eulerian method for analysing CO_2 absorption in RPBs

The Eulerian model is adopted when simulating the CO_2 absorption by MEA solutions in pilot or large-scale RPBs. In the Eulerian model, mass, momentum and energy conservation equations are solved. In addition, due to there being several components in both the gas and liquid phases, the species transport equations are solved to predict the concentration distribution of the components. Porous media models and gas-liquid drag force models are employed to express the drag force between the gas, liquid and packing. Mass transfer, heat transfer and reaction models are also solved to predict the complicated chemical and physical phenomena in the RPBs during the CO_2 absorption by MEA solutions.

3.4.1 Governing equations

In RPBs, the liquid almost achieving uniform distribution in a very short liquid entrance region, which is within about 10 mm from the inner edge of the packing [45, 48]. Therefore, the liquid flow in the RPBs can be assumed to be axisymmetric, and the 2D axisymmetric swirl Eulerian model is used to simulate the gas-liquid flow in the packing region of the RPB for remarkable savings in the computational resources. However, it is worth mentioning that for a more detailed analysis, 3D Eulerian simulations should be performed. In addition, the centrifugal environment in the packing region of the RPB is simulated through using the rotating reference frame. For the 2D axisymmetric swirl multiphase Eulerian model, the governing equations are as follows:

(i) The continuity equations:

$$\frac{\partial}{\partial x}\left(\rho_i\alpha_i v_{x,i}\right)+\frac{\partial}{\partial r}\left(\rho_i\alpha_i v_{r,i}\right)+\frac{\rho_i\alpha_i v_{r,i}}{r}=S_{m,i}+\dot{m}_i \quad (3\text{-}9)$$

$$\alpha_L+\alpha_G=1 \quad (3\text{-}10)$$

(ii) The momentum conservation equations in the axial, radial and tangential directions:

- Axial direction (x):

$$\begin{aligned}&\frac{1}{r}\frac{\partial}{\partial x}\left(r\rho_i\alpha_i v_{x,i}v_{x,i}\right)+\frac{1}{r}\frac{\partial}{\partial r}\left(r\rho_i\alpha_i v_{r,i}v_{x,i}\right)\\&=-\frac{\partial P}{\partial x}+\frac{1}{r}\frac{\partial}{\partial x}\left[r\mu_i\left(2\frac{\partial v_{x,i}}{\partial x}\right)\right]+\frac{1}{r}\frac{\partial}{\partial r}\left[r\mu_i\left(\frac{\partial v_{x,i}}{\partial r}+\frac{\partial v_{r,i}}{\partial x}\right)\right]+F_{drag,x}+S_{x,i}\end{aligned} \quad (3\text{-}11)$$

- Radial direction (r):

$$\begin{aligned}&\frac{1}{r}\frac{\partial}{\partial x}\left(r\rho_i\alpha_i v_{x,i}v_{r,i}\right)+\frac{1}{r}\frac{\partial}{\partial r}\left(r\rho_i\alpha_i v_{r,i}v_{r,i}\right)\\&=-\frac{\partial P}{\partial r}+\frac{1}{r}\frac{\partial}{\partial x}\left[r\mu_i\left(\frac{\partial v_{r,i}}{\partial x}+\frac{\partial v_{x,i}}{\partial r}\right)\right]+\frac{1}{r}\frac{\partial}{\partial r}\left[r\mu_i\left(2\frac{\partial v_{r,i}}{\partial r}\right)\right]-2\mu_i\frac{v_{r,i}}{r^2}\\&+\rho_i\alpha_i\frac{{v_{z,i}}^2}{r}+\rho_i\alpha_i\omega^2 r+F_{drag,r}+S_{r,i}\end{aligned} \quad (3\text{-}12)$$

- Tangential direction (z):

$$\frac{1}{r}\frac{\partial}{\partial x}\left(r\rho_i\alpha_i v_{r,i}v_{z,i}\right)+\frac{1}{r}\frac{\partial}{\partial r}\left(r\rho_i\alpha_i v_{x,i}v_{z,i}\right)$$

$$=\frac{1}{r}\frac{\partial}{\partial x}\left[r\mu_i\frac{\partial v_{z,i}}{\partial x}\right]+\frac{1}{r^2}\frac{\partial}{\partial r}\left[r^3\mu_i\frac{\partial}{\partial r}\left(\frac{v_{z,i}}{r}\right)\right]-\rho_i\alpha_i\frac{v_{x,i}v_{z,i}}{r}+2\rho_i\alpha_i\omega v_{r,i} \tag{3-13}$$

$$+F_{drag,z}+S_{z,i}$$

where x, r, z are the axial, radial and tangential coordinates, respectively; i is the gas phase (G) or liquid phase (L); α_i is the mass fraction of the i phase; $S_{m,i}$ is the mass source of the i phase; $\dot{m}_i$ is the mass change of the i phase due to interfacial mass transfer; ω is the angular velocity of the packing region of the RPB; F_{drag} is the drag force; S is the momentum source.

(iii) In order to model the interface species mass transfer, the phase species transport equations are solved, and the transport equation for $Y_{i,k}$, the local mass fraction of species k in the i phase, is as follows:

$$\nabla\cdot\left(\alpha_i\rho_i\vec{v}_{i,j}Y_{i,k}\right)=-\nabla\cdot\alpha_i\vec{J}_{i,k,j}+R_{i,k}+S_{m,i,k}+\dot{m}_{i,k} \tag{3-14}$$

where i is the phase index, j is the axial (x), radial (r) or tangential (z) coordinate direction, k is the species index; $Y_{i,k}$ is the mass fraction of the species k in the i phase, such as CO_2 species in the gas phase; $\vec{J}$ is the mass diffusion flux; R is the production of the species by reaction; $S_{m,i,k}$ is the mass source of species k in phase i; $\dot{m}_{i,k}$ is the mass source of species k in phase i due to the interphase mass transfer.

(iv) The energy conservation equation for phase i is as follows:

$$\nabla\cdot\left(\alpha_i\rho_i\vec{v}_i\left(\sum\nolimits_k Y_{i,k}h_{i,k}+\frac{v_i^2}{2}\right)\right)$$

$$=\nabla\cdot\left(k_{eff,i}\nabla T_i-\sum\nolimits_k h_{i,k}\vec{J}_{i,k}+\bar{\bar{\tau}}_{i,j}\cdot\vec{v}_{i,j}\right)+S_{h,i} \tag{3-15}$$

where $\frac{v_i^2}{2}$ is the kinetic energy term; $h_{i,k}$ is the specific enthalpy of species *k* in phase *i*, and it is calculated from $h_{i,k} = \int_{T_{ref,i}}^{T} c_{p,i,k} dT + h_{i,k}^0(T_{ref,i})$, where $c_{p,i,k}$ is the specific heat at constant pressure; $h_{i,k}^0(T_{ref,i})$ is the formation enthalpy of species *k* at the reference temperature $T_{ref,i}$; $T_{ref,i}$ is specified as 298.15 K; $k_{eff,i}$ is the effective heat conductivity for phase *i*; $\vec{J}_{i,k}$ is the diffusion flux of species *k* in the *i* phase; $\bar{\bar{\tau}}_{i,j}$ is the viscous stress tensor; $S_{h,i}$ is the source of enthalpy due to the heat exchange between phases.

3.4.2 Liquid inlet and outlet setting methods

When the gas and liquid counter-currently flow in the packing region of the RPB, the liquid inlet and gas outlet, and the liquid outlet and gas inlet of the packing region are overlapped, respectively. In order to overcome the difficulties of boundary condition settings, two regions for the liquid generation and elimination were designed, and the source/sink equations for the two regions in this thesis are written as follows:

(i) For the liquid generation region,

- The mass source of the liquid phase is

$$S_{m,L} = \frac{Q_L \rho_L}{\pi({r_2}^2 - {r_1}^2)h} \tag{3-16}$$

where Q_L is the volume flow rate of the liquid; r_1 and r_2 are the radial positions of the inner and outer boundaries of the liquid source region, respectively; *h* is the axial thickness of the rotating packed bed.

- The momentum sources of the liquid phase in the axial, radial and tangential directions are

$$S_{x,L} = \frac{1}{r}\frac{r\rho_L\alpha_L v_{x,L} v_{x,L}}{\Delta x} + \frac{1}{r}\frac{r\rho_L\alpha_L v_{r,L} v_{x,L}}{\Delta r} \tag{3-17}$$

$$S_{r,L} = \frac{1}{r}\frac{r\rho_L\alpha_L v_{x,L} v_{r,L}}{\Delta x} + \frac{1}{r}\frac{r\rho_L\alpha_L v_{r,L} v_{r,L}}{\Delta r} \tag{3-18}$$

$$S_{z,L} = \frac{1}{r}\frac{r\rho_L\alpha_L v_{r,L} v_{z,L}}{\Delta x} + \frac{1}{r}\frac{r\rho_L\alpha_L v_{x,L} v_{z,L}}{\Delta r} \tag{3-19}$$

where $v_{x,L} = 0$, $v_{r,L} = \frac{Q_L}{2\pi rh}$, $v_{z,L} = \omega r$; Δx is the axial size of the cell in the liquid generation region; Δr is the radial size of the cell in the liquid generation zone.

The mass fractions of the species in the liquid phase and the temperature of the injected liquid are specified as fixed values in each simulation case.

(ii) For the liquid elimination region,

- The mass sink for the liquid phase is

$$S_{m,L} = -\left(\frac{\rho_L\alpha_L v_{x,L}}{\Delta x} + \frac{\rho_L\alpha_L v_{r,L}}{\Delta r} + \frac{\rho_L\alpha_L v_{r,L}}{r}\right) \tag{3-20}$$

- The momentum sinks for the liquid phase in the axial, radial and tangential directions are

$$S_{x,L} = -\left(\frac{1}{r}\frac{r\rho_L\alpha_L v_{x,L} v_{x,L}}{\Delta x} + \frac{1}{r}\frac{r\rho_L\alpha_L v_{r,L} v_{x,L}}{\Delta r}\right) \tag{3-21}$$

$$S_{r,L} = -\left(\frac{1}{r}\frac{r\rho_L\alpha_L v_{x,L} v_{r,L}}{\Delta x} + \frac{1}{r}\frac{r\rho_L\alpha_L v_{r,L} v_{r,L}}{\Delta r}\right) \tag{3-22}$$

$$S_{z,L} = -\left(\frac{1}{r}\frac{r\rho_L\alpha_L v_{r,L} v_{z,L}}{\Delta x} + \frac{1}{r}\frac{r\rho_L\alpha_L v_{x,L} v_{z,L}}{\Delta r}\right) \tag{3-23}$$

where $v_{x,L}, v_{r,L}$ and $v_{z,L}$ are the local axial, radial and tangential velocity of the liquid, respectively.

- The mass sink for species k in the liquid phase is

$$S_{m,L,k} = -\left(\frac{\rho_L\alpha_L v_{x,L} Y_{L,k}}{\Delta x} + \frac{\rho_L\alpha_L v_{r,L} Y_{L,k}}{\Delta r} + \frac{\rho_L\alpha_L v_{r,L} Y_{L,k}}{r}\right) \tag{3-24}$$

- The energy sink is

$$S_{h,L} = -\left(\frac{\rho_L \alpha_L v_{x,L} H_L}{\Delta x} + \frac{\rho_L \alpha_L v_{r,L} H_L}{\Delta r} + \frac{\rho_L \alpha_L v_{r,L} H_L}{r}\right) \tag{3-25}$$

where H_L is the total enthalpy of the liquid phase.

3.4.3 Porous media model

The porous media model for the RPBs with wire mesh packings, which was recently proposed by Lu et al. [101], is employed in this thesis. In RPBs, only part of the packing surface is wetted by the injected liquid, therefore, in this model, as shown in Figure 3-1, the packing surface is divided into a wet area, where the liquid contacts with the packing, and a dry area, where the gas contacts with the packing.

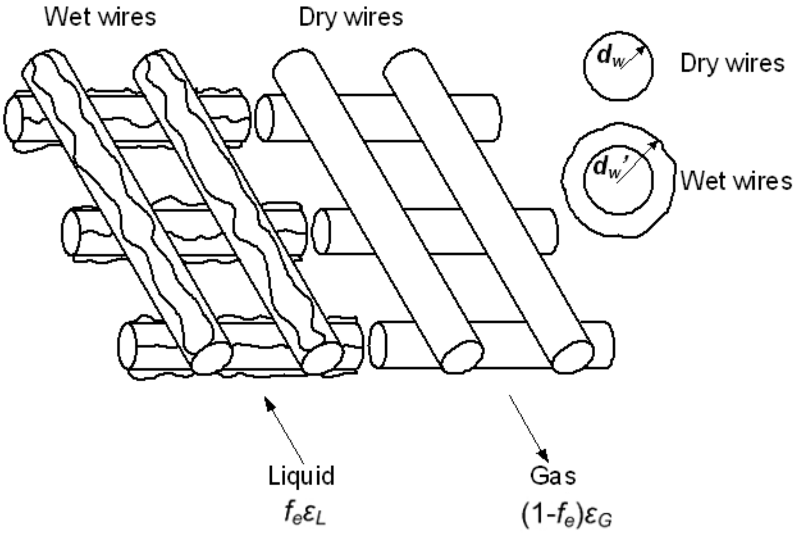

Figure 3-1 Schematic diagram of the porous media model for wire mesh packings [101].

The flow resistances for the liquid and gas phases were derived from the one-phase flow resistance of wire gauzes [138], and the equations are as follows:

$$S_{LS} = f_e \varepsilon_L \left[4\left(f_{app} + f_t\right) \frac{\rho_L {v_L}^2}{2 d_w} \frac{\varepsilon_S}{{\varepsilon_L}^3} \frac{\tau^3}{\cos^3\theta}\right] \tag{3-26}$$

$$S_{GS} = (1 - f_e)\varepsilon_G \left[4\left(f_{app} + f_t\right)\frac{\rho_G {v_G}^2}{2d_w}\frac{(1-\varepsilon_G)}{{\varepsilon_G}^3}\frac{\tau^3}{\cos^3\theta}\right] \tag{3-27}$$

where S_{LS} and S_{GS} are the resistances of the wire mesh packing for the liquid and gas phase, respectively, f_e is the fraction of the wetted area of the wire mesh packing, ε_L and ε_G are the volume fraction of the liquid and gas phase, respectively, d_w is the size of the wire, τ is the tortuosity factor of the packing; f_{app} and f_t are the Fanning friction factor and the turbulent friction factor, respectively, and they are specified as follows:

$$f_{app} = \frac{1}{Re_K}\left(\frac{3.44}{\sqrt{\chi^+}} + \frac{\frac{1.25}{4\chi^+}+16-\frac{3.44}{\sqrt{\chi^+}}}{1+\frac{0.00021}{{\chi^+}^2}}\right) \tag{3-28}$$

$$f_t = \frac{0.079}{{Re_K}^{0.25}} \tag{3-29}$$

$$\chi^+ = \frac{d_w}{D_h Re_K} \tag{3-30}$$

$$Re_K = \frac{\rho v_e D_h}{\mu} \tag{3-31}$$

where χ^+ is the dimensionless channel length, Re_K is the effective Reynold number, D_h is the hydraulic diameter, v_e is the effective velocity, μ is the viscosity of the fluid.

For the liquid-solid interaction:

$$\tau = 1 + \frac{\varepsilon_S}{2},\ d_w = \frac{4\varepsilon_S}{a_S},\ v_e = \frac{v_L}{\varepsilon_L}\frac{\tau}{\cos(\theta)},\ D_h = \frac{4\varepsilon_L}{a_S} \tag{3-32}$$

For the gas-solid interaction:

$$\tau = 1 + \frac{\varepsilon_S}{2},\ d_w = \frac{4\varepsilon_S}{a_S},\ v_e = \frac{v_G}{\varepsilon_G}\frac{\tau}{\cos(\theta)},\ D_h = \frac{4\varepsilon_G}{a_S} \tag{3-33}$$

where a_S is the specific area of the dry packing, and θ is the angle of slope of the employed packings [101].

It is worth mentioning that the employed porous media model was designed for the liquid film flow. In fact, there is also a small percentage of droplets existing in the porous media zone but they are restricted by the wire mesh and interact with the film. Therefore, this porous media model has shown applicability to predict the gas-liquid flow in RPBs with wire mesh packings [101].

3.4.4 Gas-liquid drag model

The gas liquid drag force model, which was deduced by Lu et al. [101], is employed in this thesis, and the drag force between the gas and liquid is expressed as

$$F_{GL} = f_e \varepsilon_G \left[4\left(f_{app} + f_t\right) \frac{\rho_G (v_G - v_L)^2}{2d'_w} \frac{(1-\varepsilon_G)}{{\varepsilon_G}^3} \tau^3 \right] \tag{3-34}$$

where f_{app} and f_t are expressed in Equation (3-28) and Equation (3-29), respectively, and the involved parameters are calculated as follows:

$$\tau = 1 + \frac{\varepsilon_S + \varepsilon_L}{2},\ d'_w = \frac{4\varepsilon_S}{a'_S},\ v_e = \frac{(v_G - v_L)\tau}{\varepsilon_G},\ D_h = \frac{4\varepsilon_G}{a'_S} \tag{3-35}$$

$$a'_S = \left(\frac{\varepsilon_L + \varepsilon_S}{\varepsilon_S}\right)^{\frac{1}{2}} a_S \tag{3-36}$$

where a'_S is the specific area of the wet wires; d'_w is the diameter of the wire and liquid film, as illustrated in Figure 3-1.

3.4.5 Interfacial area model

Due to the interfacial area in different RPBs and packings being case sensitive, therefore, there are no universal interfacial area models for RPBs at present. In this thesis, the interfacial area model used in the Eulerian model is the effective interfacial area correlation Eq. (5-12), which is regressed based on the data from the mesoscale 3D CFD simulations. The detailed formation process of the correlation is described in

Chapter 5, and the schematic of the implementation of the interfacial area correlation from the mesoscale 3D CFD simulations to the Eulerian CFD model can be seen from Figure 6-1.

3.4.6 Interface species mass transfer

3.4.6.1 Mass transfer equation

During the CO_2 absorption by the aqueous amine solutions, the CO_2 species is transferred from the gas phase to the liquid phase, and the transferred mass of the CO_2 is calculated using the following mass transfer equation [129]:

$$m_{GL,CO_2} = K_L A_{GL}\left(\rho_{L,CO_2}{}^{*} - \rho_{L,CO_2}\right) \tag{3-37}$$

where K_L is the overall mass transfer coefficient of the CO_2 species, $\rho_{L,CO_2}{}^{*}$ is the equilibrium mass concentration of CO_2 at the gas-liquid interface, and ρ_{L,CO_2} is the local CO_2 concentration in the liquid phase.

The equilibrium mass concentration of CO_2 at the gas-liquid interface is determined by the Henry's law, and it is expressed as follows:

$$\rho_{L,CO_2}{}^{*} = M_{w,CO_2}\frac{P_{CO_2}}{H_{CO_2-MEA}} \tag{3-38}$$

where M_{w,CO_2} is the molar mass of CO_2, P_{CO_2} is the partial pressure of CO_2 in the gas phase, H_{CO_2-MEA} is the Henry constant of CO_2 in the aqueous MEA solution, and it is estimated by the N_2O analogy method [139] as follows:

$$H_{CO_2-MEA} = H_{N_2O-MEA}\left(\frac{H_{CO_2}}{H_{N_2O}}\right)_{w} \tag{3-39}$$

where H_{N_2O-MEA} is the Henry constant of N_2O in the aqueous MEA solution, H_{CO_2} is the Henry constant of CO_2 in water, H_{N_2O} is the Henry constant of N_2O in water.

The two-resistance model [129] is used to estimate the overall mass transfer coefficient K_L. The relationship between K_L and the individual mass transfer coefficients is as follows:

$$\frac{1}{K_L} = \frac{1}{H' k_G} + \frac{1}{k_L} \tag{3-40}$$

$$H' = \frac{H_{CO_2-MEA}}{RT} \tag{3-41}$$

where k_G is the mass transfer coefficient at the gas side, k_L is the mass transfer coefficient at the liquid side. H' is the equilibrium ratio for the mass concentration of CO_2, R is the gas constant, T is the temperature.

3.4.6.2 Gas phase mass transfer coefficient

For the mass transfer coefficient at the gas side, the Hughmark model [140] is employed, and it is written as follows:

$$k_G = \frac{Sh_G D_G}{d_p} \tag{3-42}$$

$$Sh_G = 2 + 0.6 {Re_G}^{\frac{1}{2}} {Sc_G}^{\frac{1}{3}} \qquad 0 \le Re_G < 776.06,\ 0 \le Sc_G < 250 \tag{3-43}$$

$$Sh_G = 2 + 0.6 {Re_G}^{0.62} {Sc_G}^{\frac{1}{3}} \qquad Re_G \ge 776.06,\ 0 \le Sc_G < 250 \tag{3-44}$$

where Sh_G is the Sherwood number of the gas phase, D_G is the diffusivity of the gas phase, d_p is the equivalent diameter of the packing, $d_p = 6\varepsilon_S / a_S$, and Sc_G is the Schmidt number of the gas phase.

3.4.6.3 Liquid phase mass transfer coefficient

For the mass transfer coefficient at the liquid side, the film theory and the second-order irreversible enhancement model [108] are used, namely

$$k_L = E_x {k_L}^* \qquad (3\text{-}45)$$

where, E_x is the enhancement factor promoted by the chemical reaction in the liquid phase, ${k_L}^*$ is the physical mass transfer coefficient, and it is given by the film theory as follows:

$$ {k_L}^* = \frac{D_{L,CO_2}}{\ell} \qquad (3\text{-}46)$$

where D_{L,CO_2} is the diffusivity of CO_2 in the liquid phase, ℓ is the diffusion layer thickness for mass transfer in the liquid phase, which is related to the diffusivity, viscosity and flow condition of the liquid. From literature [141-143], it is found that the thickness of the diffusion layer in the liquid phase is in the ranges of $1{\sim}8 \times 10^{-5}$ m. Therefore, the sensitivity of the value of ℓ on the CO_2 absorption is investigated, and it was found that for values in the range of 1×10^{-5} m to 8×10^{-5} cm, there are no significant different results for the CO_2 absorption. Therefore, $\ell = 5 \times 10^{-5}$ m is employed for all the cases investigated in this thesis.

In addition, the enhancement factor E_x, which is developed by Wellek et al. [144], is employed in this thesis, and it is expressed as follows:

$$E_x = 1 + \left((E_i - 1)^{-1.35} + (E_1 - 1)^{-1.35}\right)^{-\frac{1}{1.35}} \qquad (3\text{-}47)$$

$$E_i = 1 + \frac{D_{L,MEA} C_{L,MEA}}{2 D_{L,CO2} C_{L,CO2}} \qquad (3\text{-}48)$$

$$E_1 = \frac{Ha}{tanh(Ha)} \qquad (3\text{-}49)$$

$$Ha = \sqrt{\frac{k_2 D_{L,CO2} C_{L,MEA}}{({k_L}^*)^2}} \qquad (3\text{-}50)$$

where $C_{L,MEA}$ and $C_{L,CO2}$ are the mole concentrations of the MEA and CO_2 species in the liquid phase, respectively; *Ha* is the Hatta number; and k_2 is the reaction rate constant.

The diffusivity of the MEA species in liquid phase is investigated by Snijder et al. [145], and the obtained correlation is expressed as follows:

$$D_{L,MEA} = exp\left(-13.275 - \frac{2198.3}{T} - 0.078142C_{L,MEA}\right) \tag{3-51}$$

Due to the chemical reaction between the CO_2 and MEA, it is impossible to obtain the physical diffusivity of CO_2 in the MEA solutions directly, therefore the diffusivity of CO_2 in the MEA solution is estimated by the N_2O analogy method [146] as follows:

$$D_{L,CO_2} = D_{L,N_2O}\left(\frac{D_{CO_2}}{D_{N_2O}}\right)_w \tag{3-52}$$

3.4.6.4 Chemical reactions in the liquid phase

For describing the chemical reaction between CO_2 and MEA in the liquid phase, the zwitterion mechanism has been generally accepted [147], where the reaction is happened in two steps. In the first step, one mole of CO_2 and one mole of MEA react and generate one mole of zwitterion. Then, in the second step, the zwitterion reacts with MEA to deprotonate. Therefore, the two-step reactions can be expressed as follows:

$$\mathrm{CO_2(aq) + HOC_2H_4NH_2(aq)} \underset{k_{-1}}{\overset{k_2}{\leftrightarrows}} \mathrm{HOC_2H_4NH_2{}^+COO^-(aq)} \tag{3-53}$$

$$\mathrm{HOC_2H_4NH_2{}^+COO^-(aq) + HOC_2H_4NH_2(aq)} \overset{k_b}{\rightarrow} \mathrm{HOC_2H_4NH_3{}^+(aq) + HOC_2H_4NHCOO^-(aq)} \tag{3-54}$$

After combining the two-step reactions, the overall reaction can be expressed as follows:

$$\mathrm{CO_2(aq) + 2HOC_2H_4NH_2(aq) \overset{k_2}{\rightarrow} HOC_2H_4NH_3{}^{+}(aq) +}$$
$$\mathrm{HOC_2H_4NHCOO^{-}(aq)} \tag{3-55}$$

According to the zwitterion mechanism with two-step reactions, the reaction rate between the CO_2 and MEA is calculated by:

$$r_{CO_2-MEA} = \frac{k_2[MEA][CO_2]}{1+\frac{k_{-1}}{k_b[MEA]}} \tag{3-56}$$

where r is the reaction rate, k_2, k_{-1} and k_b are the reaction rate constants, $[MEA]$ and $[CO_2]$ are the molar concentration. Due to $\frac{k_{-1}}{k_b[MEA]} \ll 1$, the CO_2 reaction with the MEA can be treated as a second-order irreversible reaction and the reaction rate between CO_2 and MEA can be expressed as follows:

$$r_{CO_2-MEA} = -k_2[MEA][CO_2] \tag{3-57}$$

The above simplified reaction has been extensively employed in the simulation of CO_2 absorption by the liquid amines [108, 112].

In addition, Versteeg et al. [148] proposed the correlation of the reaction rate constant k_2, and it has been employed and validated by Hosseini et al. [108], therefore it is employed in this thesis and expressed as:

$$k_2 = 4.4 \times 10^{11} exp\left(-\frac{5400}{T}\right) \tag{3-58}$$

In this thesis, the formation enthalpies of $HOC_2H_4NH_3^+$ and $HOC_2H_4NHCOO^-$ are obtained from Mishra [149].

3.4.7 Interface heat transfer

The transferred heat between the gas phase and the liquid phase $Q_{h,GL}$ is calculated by the heat transfer equation, as follows:

$$Q_{h,GL} = h_{GL} A_{GL} (T_G - T_L) \tag{3-59}$$

where h_{GL} is the heat transfer coefficient; A_{GL} is the gas-liquid interfacial area; T_L and T_G are the temperatures of the gas and liquid, respectively.

Due to investigations on the heat transfer in RPBs being very limited, in this thesis, the modified Hughmark model [140] is employed to predict the gas-liquid heat transfer coefficient h_{GL}, which is analogous to the gas phase mass transfer coefficient. In addition, due to lack of detailed measurements of the heat flux at the wall of RPBs, the wall of the RPB is assumed to be adiabatic.

Chapter 4: Characteristics of liquid flow in an RPB: A 2D CFD analysis

Summary

This chapter presents a 2D CFD model for analysing the characteristics of liquid flow within an RPB. The VOF multiphase flow model is implemented to calculate the flow field and capture the interface between the gas and liquid phases in the RPB. The simulation results show good agreement with the experimental data. The distinct liquid flow patterns in different regions of an RPB are clearly observed. The simulation results indicate that increasing the rotational speed dramatically decreases the liquid holdup and increases the degree of the liquid dispersion. The increasing liquid jet velocity decreases the liquid residence time but slightly increases the liquid holdup. In addition, the liquid holdup increases and the degree of the liquid dispersion decreases with increasing MEA concentration, but the effects are weaker at a higher rotational speed. With the increasing of the contact angle, both the liquid holdup and the degree of the liquid dispersion are reduced. This proposed model leads to a much better understanding of the liquid flow characteristics within RPBs.

4.1 Introduction

The fluid mechanics of RPBs is not fully understood, thus accurate predicting the characteristics of the liquid solvent flow and subsequently the mass transfer within the RPB is difficult. In order to achieve a more reliable prediction of the liquid flow characteristics in an RPB, a new 2D computational framework of an RPB is proposed based on the VOF method. This model adopts the real round cross-section of the wire mesh as the packing characteristics and a non-uniform grid generation strategy has been employed to make the model available to capture the liquid films on the packing surface so that both the formation of the liquid droplet and the formation of the liquid film can be simulated. In addition, the fluid flow is calculated in a rotational coordinate system that is fixed on the RPB rotor. The SST k-ω model is applied to close the Navier-Stokes equations. Both low and high concentrations of aqueous monoethanolamine (MEA) solutions are investigated for the possible flow patterns in the RPB. The effects of the rotational speed, liquid jet velocity, liquid viscosity and contact angle have been simulated to provide an improve understanding on the detailed flow patterns, liquid holdup, liquid residence time, and the degree of liquid dispersion, which are important parameters for RPB designs.

4.2 CFD modelling

4.2.1 Geometry of the investigated RPB

The wire mesh packing is investigated in this chapter, which has a good performance to deal with the high viscosity fluid [47] and it has a good mass transfer performance among several different types of packings [150]. In addition, it is suitable to deal with large amounts of flue gas in the PCC process due to the high porosity. The RPB simulated is based on the experiments of Yang et al. [47], and the X-ray CT scan image of the wire mesh packing that was employed in the RPB and a photo of one layer of the wire mesh packing are shown in Figure 4-1 (a) and (b), respectively.

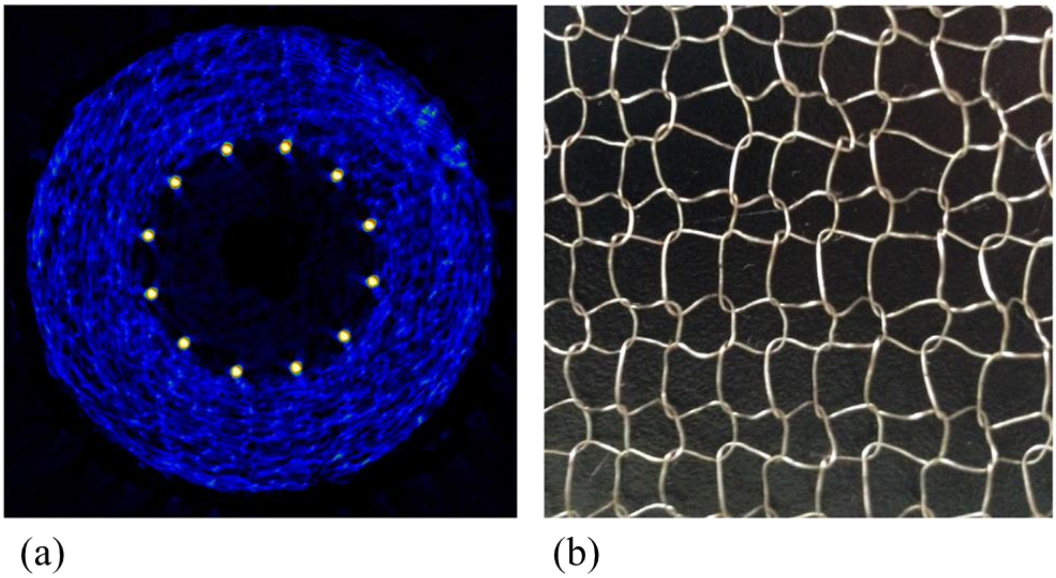

Figure 4-1 (a) An X-ray CT scan image of the wire mesh packing; and (b) a photo of one layer of the wire mesh packing [47].

As shown in Figure 4-1, because of the irregular structure and limited information on the packing employed in the experiments [47], it is almost impossible to make an identical packing arrangement in the CFD model. The annular packing region of the RPB consists of a woven wire mesh in rolls, which can be reasonably simplified into a concentric multi-layer wire mesh, and each layer is composed of concentric and coaxial wires. Figure 4-2 (a) shows the simplified diagram of the employed packing with the main dimensions. It has a 20 mm height, 42 mm inner diameter and 82 mm outer diameter, and the specific area is 497 m^2/m^3 and the void fraction is 0.95. The liquid is radially injected into the packing from the centre of the RPB through a liquid distributor, which is designed as a rectangular crack with the size of 1 mm × 15 mm. The rotational speed of the bed varied from 500 rpm to 2500 rpm, the liquid flow rate ranges from 1094 ml/s to 2580 ml/s, and this means that the liquid jet velocity ranges from 1.22 m/s to 2.87 m/s. The data on the liquid holdup under these operating conditionals are available from the experiment [47].

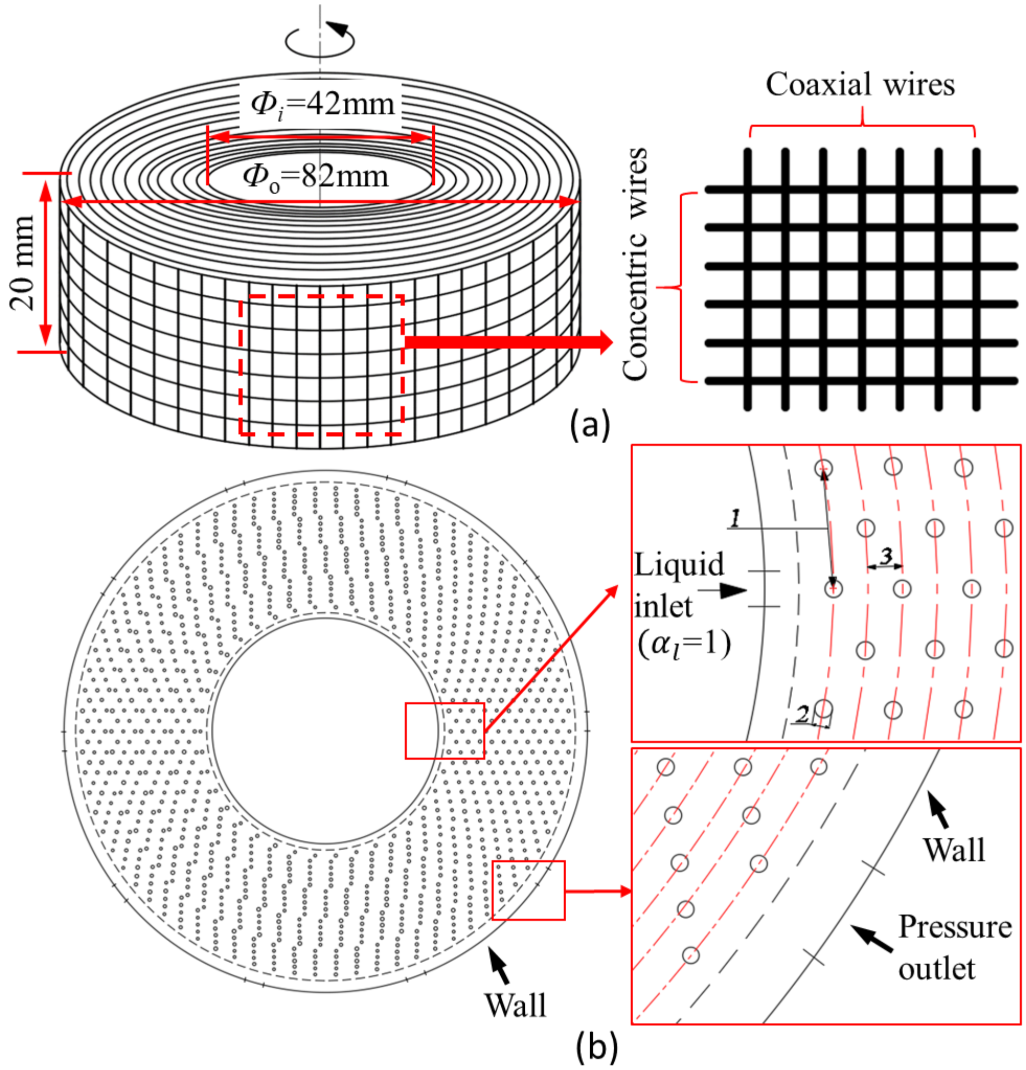

Figure 4-2 (a) Schematic diagram of the wire mesh packing; and (b) 2D calculation domain of an RPB and the partial schematic illustration of the packing arrangement and boundary conditions (1. Centre distance between two adjacent wires in the circumferential direction; 2. Diameter of the wire; 3. Centre distance between two adjacent mesh layers).

A cross-section, where there are only coaxial wires, is chosen to build up the 2D calculation domain (see Figure 4-2 (b)). The influence of the concentric wires on the liquid flow has been ignored, mainly because in a 2D model the concentric wires would form closed circles that the liquid cannot flow across. Since the direction of the liquid flow in most of the packing region is almost radial relative to the packing, it is expected that the liquid flow characteristics would be similar to that when it hits a coaxial wire.

In order to make the 2D model have similar characteristics, such as void fraction and specific area, compared to the real physical models, several important parameters have been controlled to generate the 2D packing geometry. The diameter of the wires is 0.5 mm and the distance between the centres of two adjacent packing wires in the circumferential direction is 3.5 mm. There are 21 concentric packing layers in total and the distance between the centres of two adjacent mesh layers in the radial direction is 1 mm. Under this arrangement, the void fraction of the packing is 0.94, and the specific area is 469 m^{-1}. These parameters are similar to the RPB employed by Yang et al. [47]. Therefore, the simulation results of the liquid holdup can be compared with the experimental results for model validation.

4.2.2 Computational grid

The computational grid generation is a critical step that influences the convergence, stability, and accuracy of the simulations. From the previous study [44, 45, 134], the liquid film flow is an essential flow pattern in the RPB. Moreover, the morphology of small ligaments and droplets is very sensitive to the boundary layers on the packing surfaces. Accurately resolving the boundary layer in the neighbourhood of the packing surfaces is the basis for accurately predicting the liquid flow field by using the VOF-based CFD methods. Therefore, considering the computational accuracy of the liquid flow field, especially in the vicinity of the packing surfaces, as well as the overall computing efficiency, the flow domain is discretized with a non-uniform mesh as shown in Figure 4-3. A higher mesh density is implemented near the packing surface in order to resolve the flow boundary layer accurately and then the size of the grids grows gradually. In the region far away from the packing surface, the grid is quadrilateral dominate. The final grid size is a result of a grid sensitivity study, which is discussed in more detail in Section 4.2.5. In this chapter, the geometry and grid of the computational domain is generated with ICEM CFD 16.1.

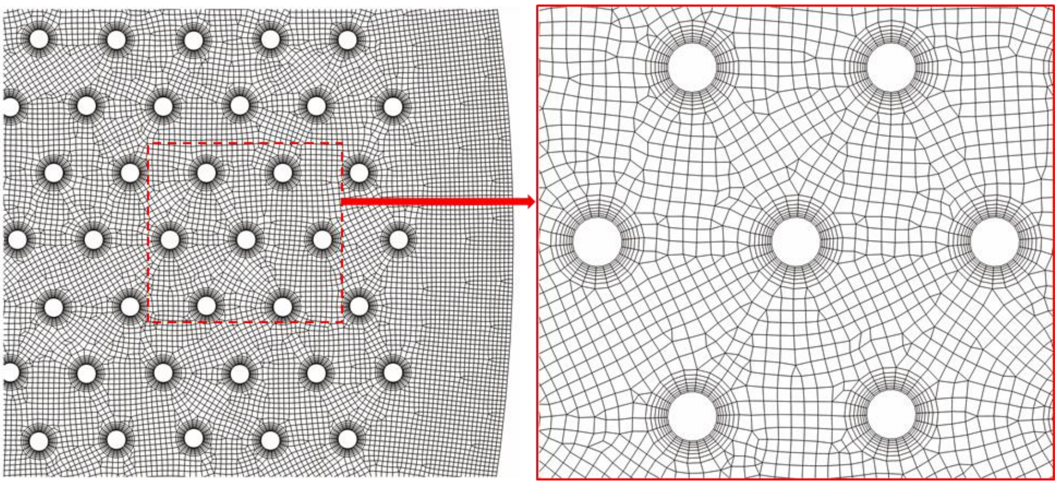

Figure 4-3 Computational grid arrangement in the RPB.

4.2.3 Boundary conditions

The computational domain and the locations to which the flow boundary conditions are applied are shown in Figure 4-2 (b). The liquid inlet is specified by a fixed jet velocity with the volume fraction of the liquid phase being set to unity. The jet velocity ranges from 1.22 m/s to 2.87 m/s, which corresponds to the experimental settings [47]. The turbulent intensity is specified as 1%, and the hydraulic diameter is specified as the nozzle width, 1 mm. Many investigations indicate that the gas has little effect on the main liquid flow pattern [45] and liquid holdup [57, 58]. Therefore, the effect of the gas flow on the liquid flow characteristics is not accurately investigated in this chapter. Thus, the volume fraction of the liquid phase and the fluid velocity are set to zero on the rest of the inner boundary. In addition, the computational domain is fixed on a rotational coordinate system; therefore, the liquid nozzle rotates in the opposite direction relative to the rotational coordinate system and the movement of the nozzle is realized by a user-defined function (UDF). In the UDF, the position of the liquid nozzle is defined as a function of time and it is updated at each time step during the transient calculation. This nozzle setup method has been verified by comparing the predicted flow patterns and liquid holdup with the sliding mesh method as adopted in the previous research [91]. The comparison results indicate that the two nozzle setup methods have the same effects while moving the nozzle using the UDF method reduces the complexity of the modelling and presents more flexibility when changing the width of the liquid nozzle without rebuilding the geometry and regenerating the grid.

In the outer periphery of the computational domain, the wall condition is set to simulate the casing wall of the RPB and ten evenly distributed pressure outlets with a width of 3 mm are set to drain the liquid. The contact angle between the liquid and the wall is set at 150° so as to represent a hydrophobic material, thus the collected liquid can freely move along the wall and quickly drain from the nearest liquid outlet. In addition, there is a gap between the casing wall and the packing region. Therefore, the wall has almost no influence on the flow pattern and the liquid holdup in the packing region, where we pay most of our attention. For the surface of the packing, the no-slip boundary condition and wall adhesion is specified. However, a given packing surface may have different contact angles depending on the liquid properties, and for a given liquid, the contact angle also varies with different packing surfaces [103]. In addition, the contact angle of the packing surface corresponding to different solvents is not available in the literature. Therefore, in this chapter, a value of 30° is specified as the contact angle of the packing surface in the initial simulations. Further, considering the importance of the contact angle on the flow pattern and liquid holdup, the effect of varying the contact angle is investigated. The computational domain with a rotational speed of the reference frame in the range of 500–1500 rpm is used to investigate the effect of the rotational speed of the PRB on the flow.

4.2.4 Solution procedure

Transient simulations are performed using the ANSYS® Fluent 16.1 software in a double precision mode, and it incorporates the in-house developed UDF for setting the inlet boundary conditions. The pressure-velocity coupling is resolved by the PISO algorithm, and the PRESTO scheme is employed for the pressure discretization. The Geo-Reconstruct method is applied for the spatial discretization of the volume fraction equation, the second-order upwind scheme is employed for solving the momentum equations and turbulence equations. In addition, for the convergence criteria, the residuals of the mass balance equations are taken to be less than 1×10^{-4} and the residuals of all the other equations are less than 1×10^{-5}. Different time step sizes have been tested to check the effect of the time step size on the results. As a result, the time step size is set as 1×10^{-5} s when the rotational speed is between 500 to 750 rpm (include 750 rpm) and 5×10^{-6} s when the rotational speed is between 750-1500 rpm. In addition, the maximum number of iterations of 30 are performed per time step in order to achieve the calculation convergence. The instantaneous liquid holdup is monitored for each simulation to make sure it achieves the pseudo steady state and the average liquid holdup in each simulation is calculated based on the instantaneous liquid holdup after the simulation achieving the pseudo steady state.

4.2.5 Grid independence

A grid independence study is conducted to determine a reasonable computational grid. Four different grids consisting of 0.13, 0.43, 0.64 and 0.87 million quadrilateral-dominated cells have been employed to investigate the effect of the mesh on the CFD solutions. The grid is refined in the vicinity of the packing surface. When increasing the grid numbers in the packing surface, the regions, which are away from the packing surface, can correspondingly be refined according to the meshing strategy employed. As shown in Figure 4-4, solutions for the liquid holdup and the liquid dispersion index (explained in Section 4.3.4.1) at a demanding condition (N=1500 rpm) are almost the same as when using a grid with no less than 0.43M cells, which may be regarded as a reasonable fine grid to predict the overall liquid flow characteristics. Therefore, for the simulations of the liquid holdup and the liquid dispersion index, the grid with 0.43M cells is used as a trade-off between computing time and simulation precision. However, a refined grid can achieve a clearer observation of the detailed liquid flow pattern. Therefore, for investigating the liquid flow pattern, the 0.87M grid is chosen.

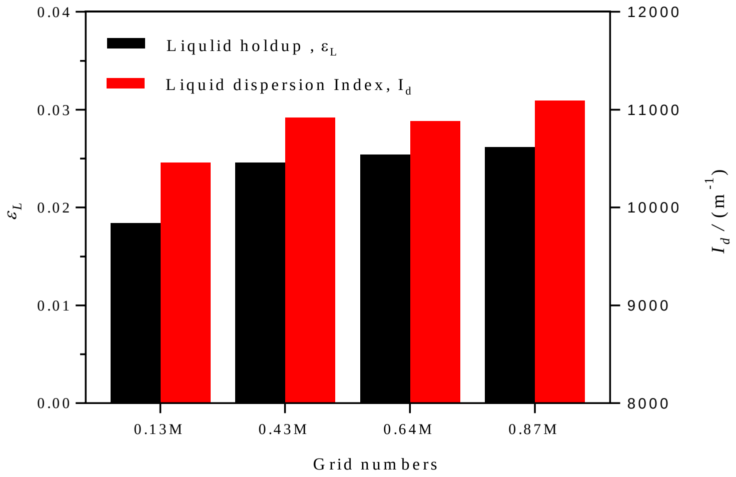

Figure 4-4 Predicted liquid holdup and liquid dispersion index using four different grids. (N=1500 rpm, u_0 = 1.53 m/s, water).

4.3 Results and discussion

4.3.1 Model validation

The CFD predicted liquid holdup has been compared with the experimental results measured by Yang et al. [47] and with the correlation proposed by Burns [56] as follows:

$$\varepsilon_L = 0.039\left(\frac{g}{g_0}\right)^{-0.5}\left(\frac{U}{U_0}\right)^{0.6}\left(\frac{\nu}{\nu_0}\right)^{0.22} \qquad (4\text{-}1)$$

where $g_0 = 100\ m/s^2$, $U_0 = 0.01\, m/s$ and $\nu_0 = 10^{-6}\, m^2/s$ are characteristic values.

This correlation has been adopted by many researchers for validation [93] and process modelling [41, 89, 90, 151] of RPBs. The simulation results in this chapter show that the effect of the rotational speed (Figure 4-5 (a)), the liquid jet velocity (Figure 4-5 (b)) and the liquid viscosity (Figure 4-5 (c)) on the liquid holdup is similar to those obtained by Yang et al. [47] experimentally and the Burns correlation. It is noted that the liquid holdup from the simulation is closer to the experimental data than the widely accepted Burns correlation. This may be because the conductivity measurement method adopted in the experiments [56] cannot take into consideration of the free droplets, which may take up an important percentage of liquid in the packing region of typical RPBs. However, the liquid holdup from the simulation is still lower than the liquid holdup obtained by the X-ray technique in general. On the one hand, this is because the liquid may accumulate at the intersections of the two crossed wires but this cannot be considerate in this 2D model. On the other hand, because the concentric wires are ignored in the 2D model, the specific area (469 m^{-1}) of the packing in the model is slightly less than that of the real packing (497 m^{-1}) although the void fraction of the packing (0.94) in the

2D model is similar to that in the experiments (0.95). Therefore, there is less packing surface to be wetted by the liquid. In general, this model can reflect the effects of the above-mentioned influencing factors on the liquid holdup, compared to the experimental data obtained by Yang et al. [47]. Although the simulation is performed in a 2D domain rather than a real 3D domain and there are some limitations due to the simplification of the real geometry, we take the view that the 2D CFD model can still effectively predict the liquid flow characteristics in the RPB.

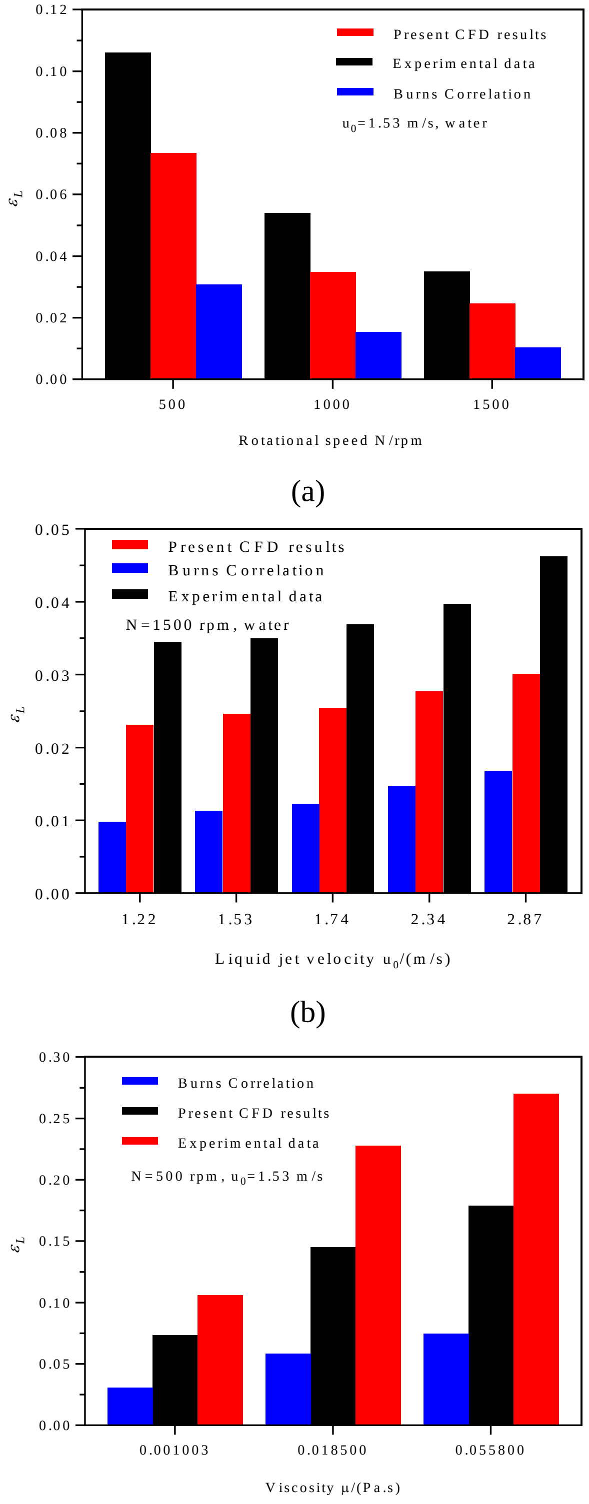

(a)

(b)

(c)

Figure 4-5 Comparison of simulation results of liquid holdup with the experimental data [47] and Burns correlation [56]: (a) Effect of the rotational speed, (b) effect of the liquid jet velocity, and (c) effect of the liquid viscosity.

4.3.2 Liquid flow pattern in the RPB

Solvents with 30 wt% MEA are typically recommended to be used in conventional packed bed absorbers. However, the RPB can cope with much higher MEA concentrations. In this chapter, the 50 wt% aqueous MEA solution is used to demonstrate the liquid flow patterns in the RPB. The CFD model predicted four typical liquid flow patterns in two different packing regions and under two rotational speeds of the RPB are shown in Figure 4-6. As can be seen in Figure 4-6, or Figure 4-2 (b), the packing space is unevenly distributed in the whole packing region. The arrangement of the wires in the CFD model is similar to the inherent nature of the random wire mesh packing, since the wire mesh is compactly arranged in rolls, which forms regular but an uneven distribution around the bed. The distribution of the wires in different circumferential regions of the packing has more or less effect on the liquid flow pattern, however distinct flow patterns still can be observed in different packing regions around the bed, which are mainly determined by the radial positions and the operation conditions. The packing region close to the liquid inlet is usually defined as the entrance region, which is the region of about 10 mm in radius in the inner side of the dashed lines as indicated in Figure 4-6. The rest of the packing region is usually defined as the bulk region. Also, different flow patterns between the two regions have been confirmed by Guo et al. [45], Yan et al. [48] and Guo et al. [49] through different experimental methods, which indicate the feasibility of the CFD model to investigate the liquid flow pattern in the RPB.

4.3.2.1 Flow pattern in the entrance region

As shown in Figure 4-6, when the liquid is injected into the packing region from the liquid inlet, the rotational packing splits the liquid continuously. Most of the liquid is sheared into the liquid ligaments but still moves almost along the radial direction, which is mainly due to the existence of the initial momentum in the radial direction. A small percentage of the liquid becomes liquid films and it adheres to the packing wires and rotates with the packing. As for the liquid ligaments in the entrance region, the radial velocity of the liquid decreases from the initial jet velocity to a lower velocity. This is mainly due to the loss of the liquid initial momentum when the liquid strikes the packing. However, the tangential velocity of the liquid gradually increases from zero to approach the packing's tangential velocity under the action of the drag force from the packing. As a result, the ratio of the tangential velocity to the radial velocity of the liquid ligaments gradually increases, and the liquid ligaments are all captured by the packing at the end of the entrance region.

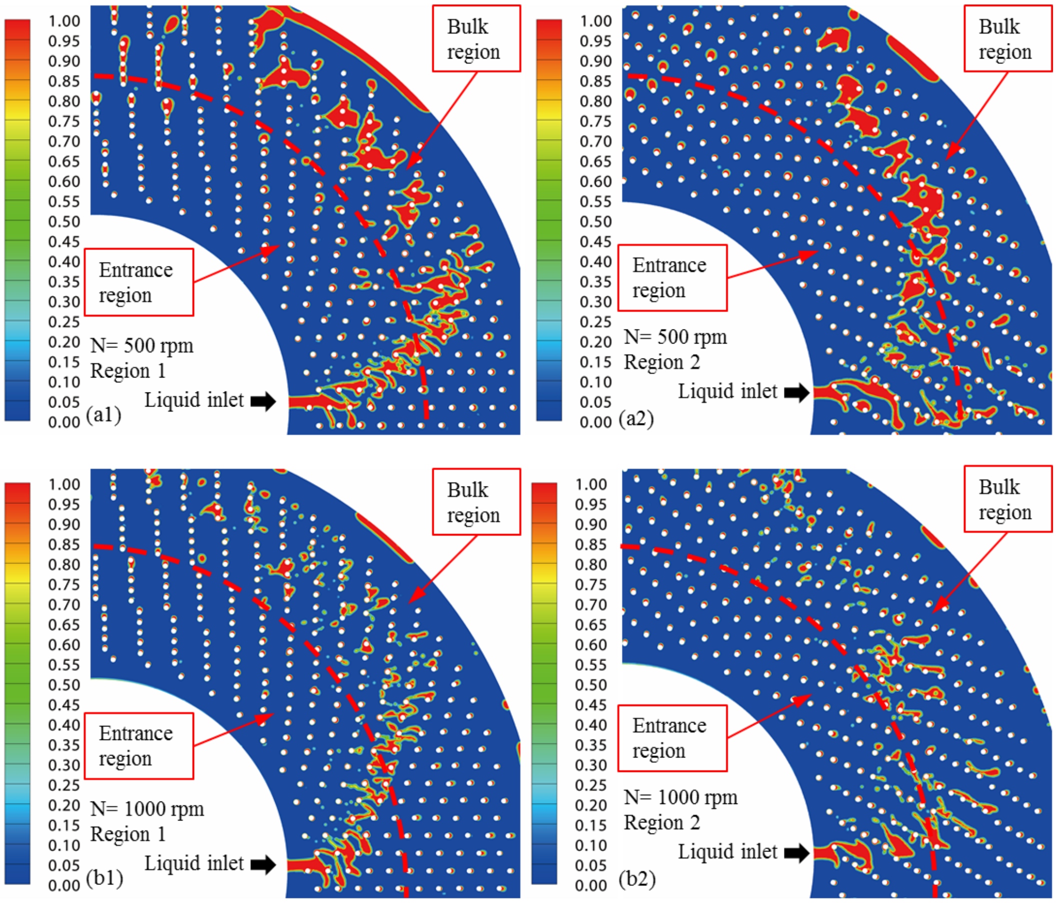

Figure 4-6 Typical liquid flow patterns in different regions (50 wt% MEA, $u_0 = 2.87$ m/s, contours represent the volume fraction of liquid).

4.3.2.2 Flow pattern in the bulk region

Within the bulk region, at a relatively low rotational speed, such as 500 rpm, where the average centrifugal acceleration in the bed is about 80 m/s^2, the liquid flow pattern is a pore-dominated flow, as shown in Figure 4-6 (a1) and (a2). This is because the surface tension makes the liquid prefer to coalesce and the relative velocity between the liquid and the packing is not large enough to make it separate. As a result, the liquid exists in the form of liquid groups and travels in the pores of the packing. While at a higher rotational speed, such as 1000 rpm, where the average centrifugal acceleration in the bed is about 320 m/s^2, the liquid flow pattern becomes a droplet-dominated flow, as shown in Figure 4-6 (b1) and (b2).

The typical transportation process of a droplet in the bulk region of the packing is shown in Figure 4-7. It shows that the liquid moves relative to the rotating packing at 1000 rpm within seven milliseconds. Initially, the observation is focused on the droplet within the dashed circles in Figure 4-7 (a) at time t_0. Then the droplet moves, disperses and mixes with other liquid as time goes on. The liquid elements, which originated from the same droplet within the red dashed circle in Figure 4-7 (a), are marked by the dashed circles in the rest of the figures. As can be observed, when the liquid droplet hits the packing surface and one part of the liquid attaches to the packing surface and becomes a liquid film, and the other part of the liquid moves into the next layer of the packing space. The percentage of the free moving liquid relative to the captured liquid by the packing surface depends on the voidage of the packing, that is, a higher voidage leads to a higher percentage of free moving liquid to the next layer. As for the captured liquid by the packing surface, when the liquid leaves the surface of the wires, the stretched liquid droplets always breakup and generate some satellite droplets (see Figure 4-7 (d) and (h)). This is because the surface tension of the liquid makes it have the trend to form liquid droplets rather than liquid ligaments. At the same time, the droplet–droplet collisions occur in the packing space, see Figure 4-7 (e) to (f), and the small droplets collide and merge into big droplets. These steps repeat until the liquid moves out of the packing region and the droplets become smaller and smaller and the liquid surfaces continuously update.

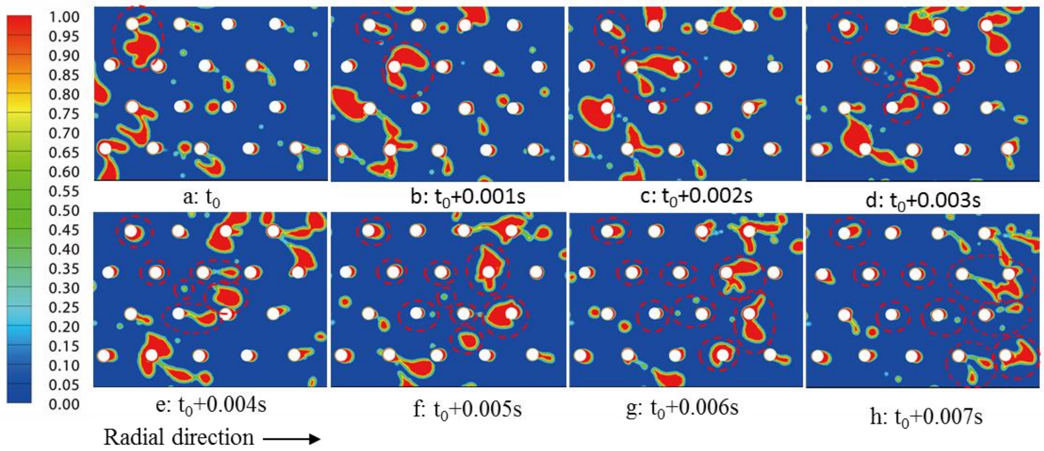

Figure 4-7 Transient development of the liquid phase (50 wt% MEA, N = 1000 rpm, u_0 = 1.53 m/s, contours represent the volume fraction of liquid).

4.3.3 Liquid holdup and liquid residence time in the RPB

The liquid holdup (ε_L), defined as the liquid volume per unit packing volume, and the mean residence time ($\bar{t}$) of the liquid are two essential parameters for an RPB [45, 47, 56] and the two parameters are closely related. The mean residence time of liquid can be determined based on the liquid holdup using Equation (2-1), where U is the superficial liquid flow velocity and it can be calculated by

$$U = \frac{u_0 d}{2\pi r} \tag{4-2}$$

where u_0 is the liquid jet velocity, d is the width of the nozzle and $r = (r_i + r_o)/2$.

4.3.3.1 Effect of rotational speed on liquid holdup

Figure 4-8 shows the effect of the rotational speed (*N*) on the liquid holdup at two different liquid jet velocities where the 50 wt% aqueous MEA solution is used. The figure illustrates that the liquid holdup decreases with the increasing rotational speed from 500 to 1500 rpm for both liquid jet velocities of 1.53 and 2.87 m/s. The liquid gains the tangential velocity from the packing continuously, and it almost synchronously rotates with the packing in the bulk region. Therefore when increasing the rotational speed, the liquid can obtain a higher tangential velocity, thus resulting in a higher centrifugal acceleration as well as a higher radial velocity relative to the packing. Therefore, the residence time of the liquid decreases as well as the liquid holdup decreases.

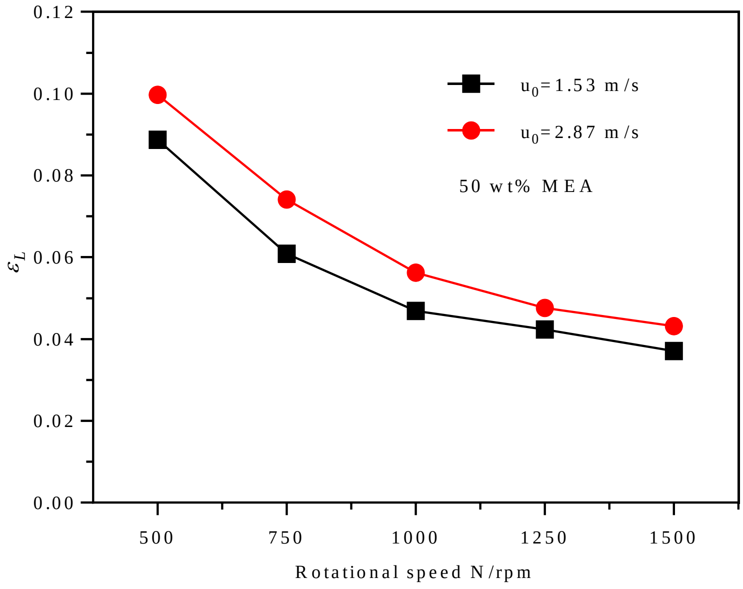

Figure 4-8 Effect of the rotational speed on the liquid holdup.

In addition, on increasing the rotational speed, the liquid can gain more kinetic energy from the packing, and the liquid can be split into smaller liquid droplets and fragments (compare Figure 4-6 (a1) and (b1) or compare Figure 4-6 (a2) and (b2)). Therefore, the percentage of liquid that flies into the void of the packing increases. When the liquid flies in the void of the packing, it is free from the drag force from the packing and this contributes to the increasing average radial velocity. As shown in Figure 4-8, on increasing the rotational speed from 500 to 1000 rpm, where the liquid flow is dominated by the pore flow, the liquid holdup decreases by about 50%. While, when increasing the rotational speed from 1000 rpm to 1500 rpm, the liquid holdup decreases by only about 20% and this may be because the droplets are difficult to be captured by the packing when the rotational speed is higher than 1000 rpm, where the liquid flow is dominated by the droplet flow and the droplets become smaller and smaller.

From Figure 4-7 (e) to (h), it can be observed that some of the liquid is retained in the packing surface and does not move with time, and this is due to the adhesion force between the liquid and the packing surface. In this state, the centrifugal force and the adhesion force are in balance. When the rotational speed increases, then the retained liquid obtains a higher centrifugal force, and when the adhesion force cannot meet the centrifugal force, then the retained liquid moves away from the packing surface. Therefore, the percentage of the retained liquid decreases with increasing rotational speed, which also leads to the decrease in the liquid holdup.

4.3.3.2 Effect of liquid jet velocity on liquid holdup and residence time

The effect of the liquid jet velocity on the liquid holdup is shown in Figure 4-9. It is clear that the liquid holdup increases with the increasing liquid jet velocity, while, the increase rate of the liquid holdup is very small. This is because the average liquid radial velocity increases with increasing the liquid jet velocity. Specifically, a higher liquid jet velocity directly increases the liquid radial velocity in the entrance region. In addition, with an increase in the liquid flow rate, the frequency of the liquid-liquid collisions and liquid-packing collisions increases, therefore small droplets and thin films are easier to coalescence and form big droplets, which increases the escape frequency of the liquid from the packing surface. Due to the same reason, the liquid residence time decreases with the increasing liquid jet velocity, as shown in Figure 4-9. As for the flow pattern, on comparing Figure 4-10 (a) and (b), with an increase in the liquid jet velocity, the radial distance of the entrance region increases and the circumferential liquid maldistribution is more severe.

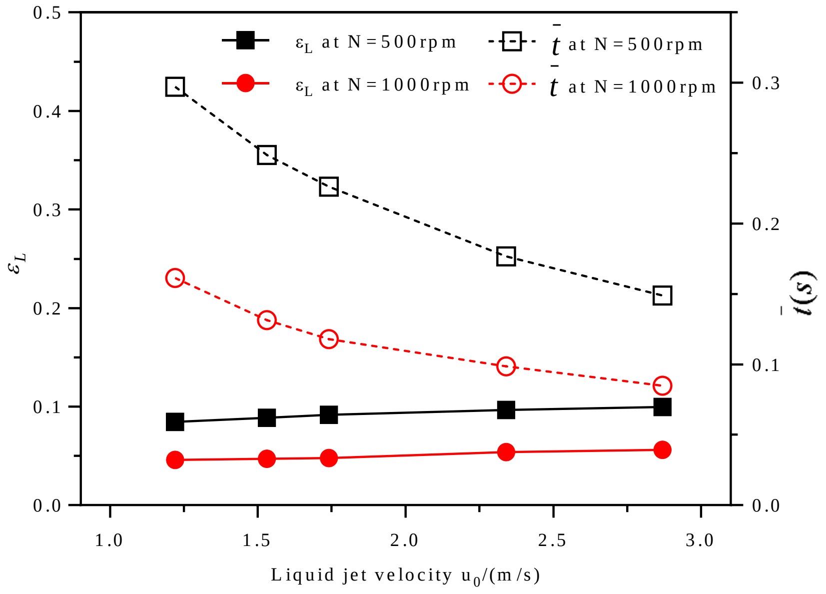

Figure 4-9 Effect of the liquid jet velocity on the liquid holdup and the residence time.

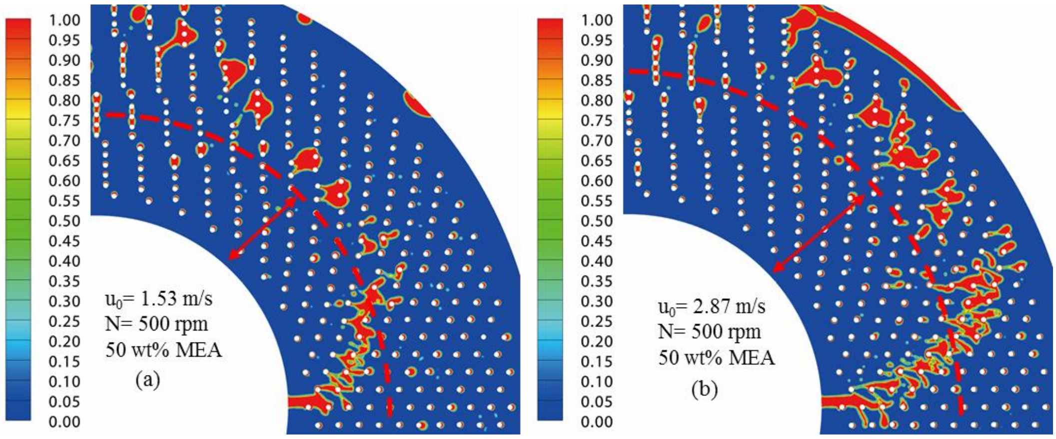

Figure 4-10 Effect of the liquid jet velocity on the liquid flow pattern (contours represent the volume fraction of liquid).

4.3.3.3 Effect of MEA concentration on liquid holdup and liquid residence time

The effect of the MEA concentration on the liquid holdup is shown in Figure 4-11, which shows that the liquid holdup increases with the increasing MEA concentration from 30 wt% to 90 wt%. This is mainly because the liquid viscosity noticeably increases with the increasing concentration of the MEA. As shown in Figure 4-12, most of the liquid is partially in contact with the packing surface where the viscous force plays a major role. With the increasing of the liquid viscosity, the liquid deformation rate reduces and this causes the residence time of the liquid that is partially attached onto the packing surface to increase. In addition, the thickness of the boundary layer increases with the increasing liquid viscosity and this leads to the liquid volume that is attached to the packing surface to increase. Thus, the liquid holdup increases with an increasing liquid viscosity. From another perspective, the drag force is the driving force for the liquid movement in the tangential direction, but it is resistant to the liquid movement in the radial direction. As a result, with increasing the liquid viscosity, the liquid is easier to attach onto the packing surface and follow the rotation of the packing, which leads to a better circumferential liquid distribution (compare Figure 4-12 (a) and (b) or compare Figure 4-12 (c) and (d)). Also, this contributes to the increasing of the liquid holdup.

However, as shown in Figure 4-11, the effect of the MEA concentration on the liquid holdup is weaker at a higher rotational speed. This is because at a higher rotational speed, the free moving liquid droplets increases and the amount of the liquid films attached to the packing surface reduces and thus the influence of the viscous resistance force on the liquid becomes weaker. Such as, at 500 rpm, the flow pattern is pore-dominated flow, and much liquid is in contact with the packing surface, thus the liquid viscosity has a stronger influence on the liquid holdup than that at 1000 rpm or 1500 rpm, where the liquid is in the droplet-dominated flow pattern.

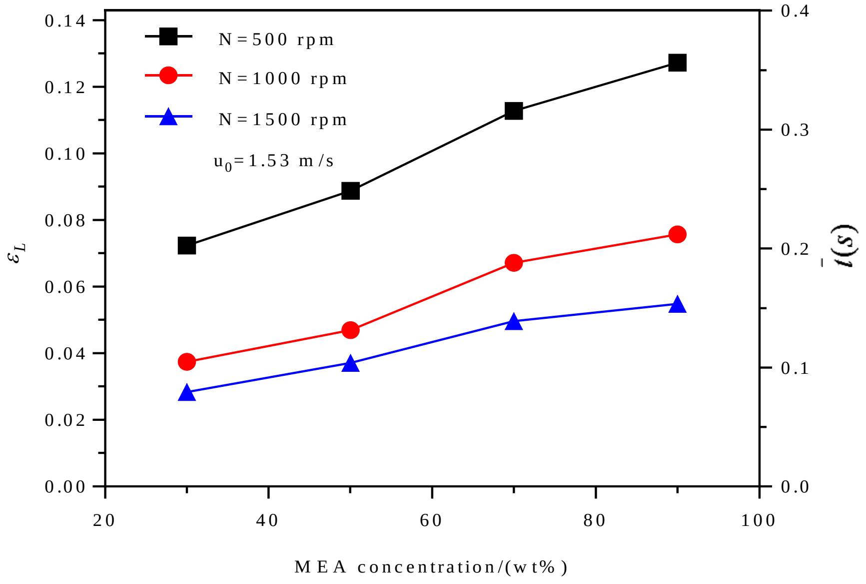

Figure 4-11 Effect of the MEA concentration on the liquid holdup and the liquid mean residence time at two different rotational speeds.

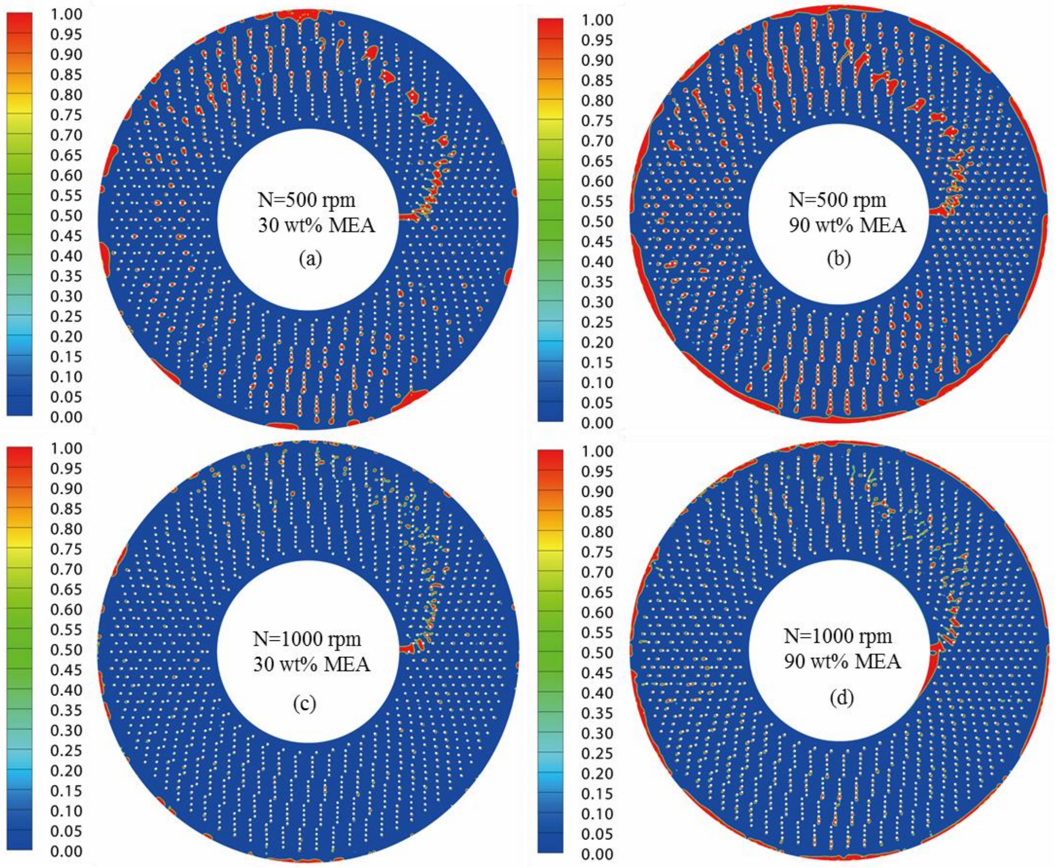

Figure 4-12 Effect of MEA concentration on the liquid flow pattern at different rotational speeds (u_0=1.53m/s, contours represent the volume fraction of liquid).

When keeping the liquid jet velocity as constant, the mean residence time of the liquid ($\bar{t}$) is proportional to the liquid holdup based on Equation (2-1). Therefore, the effect of the MEA concentration on $\bar{t}$ is the same as the effect of the MEA concentration on the liquid holdup and the value of $\bar{t}$ can be obtained from the right Y-axis of Figure 4-11.

4.3.3.4 Effect of contact angle on liquid holdup and liquid residence time

The contact angle is an important parameter for gas-liquid-solid systems and different packing materials and/or different surface treatments lead to different contact angles. Stainless steel is hydrophilic but some materials used in the RPB packing are hydrophobic [152]. In order to cover a wide range of materials, the effect of the contact angles from 0 degree, where complete wetting occurs [153], to 150 degrees on the liquid holdup and flow pattern is investigated. The increasing of the contact angle means the wettability of the packing by the liquid is not as good. Figure 4-13 shows that the liquid holdup is reduced with the increasing of the contact angle.

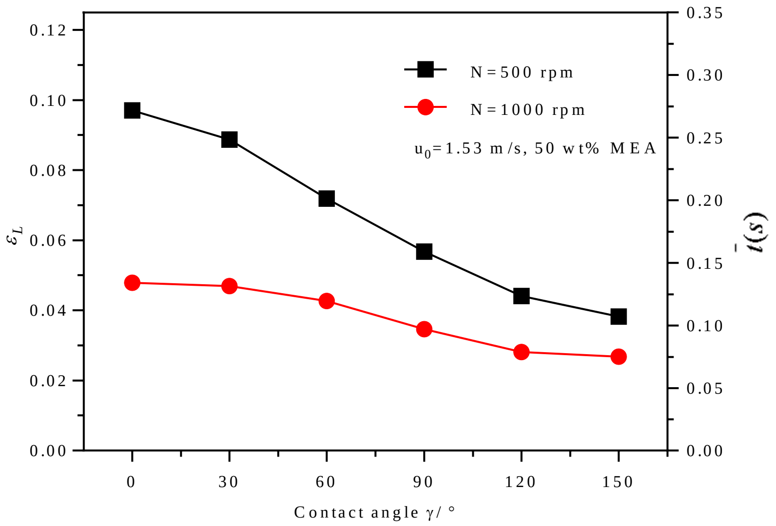

Figure 4-13 Effect of the contact angle on the liquid holdup and the liquid mean residence time at two different rotational speeds.

When the contact angle is less than 90 degrees, the material is hydrophilic (see Figure 4-14 (a)). At a certain rotational speed, with an increase in the contact angle, the percentage of the liquid that is attached to the packing surface decreases. Moreover, on increasing the contact angle, the flow pattern transformation, i.e. from the pore-dominated flow to the droplet-dominated flow, occurs at a lower rotational speed. When the contact angle is larger than 90 degrees, the material is hydrophobic (see Figure 4-14 (b)). Therefore, when the liquid-packing collision occurs, the liquid is almost impossible to be attached on to the packing surface. Further, with the increasing of the contact angle, more small droplets are generated. This phenomenon also has been observed in the experimental work of Zheng et al. [152]. Because the packing has no viscous resistance on the flying liquid droplets, a large percentage of liquid droplets means a higher average radial velocity and this decreases the liquid holdup. The value of $\bar{t}$ is marked on the right Y-axis of Figure 4-13.

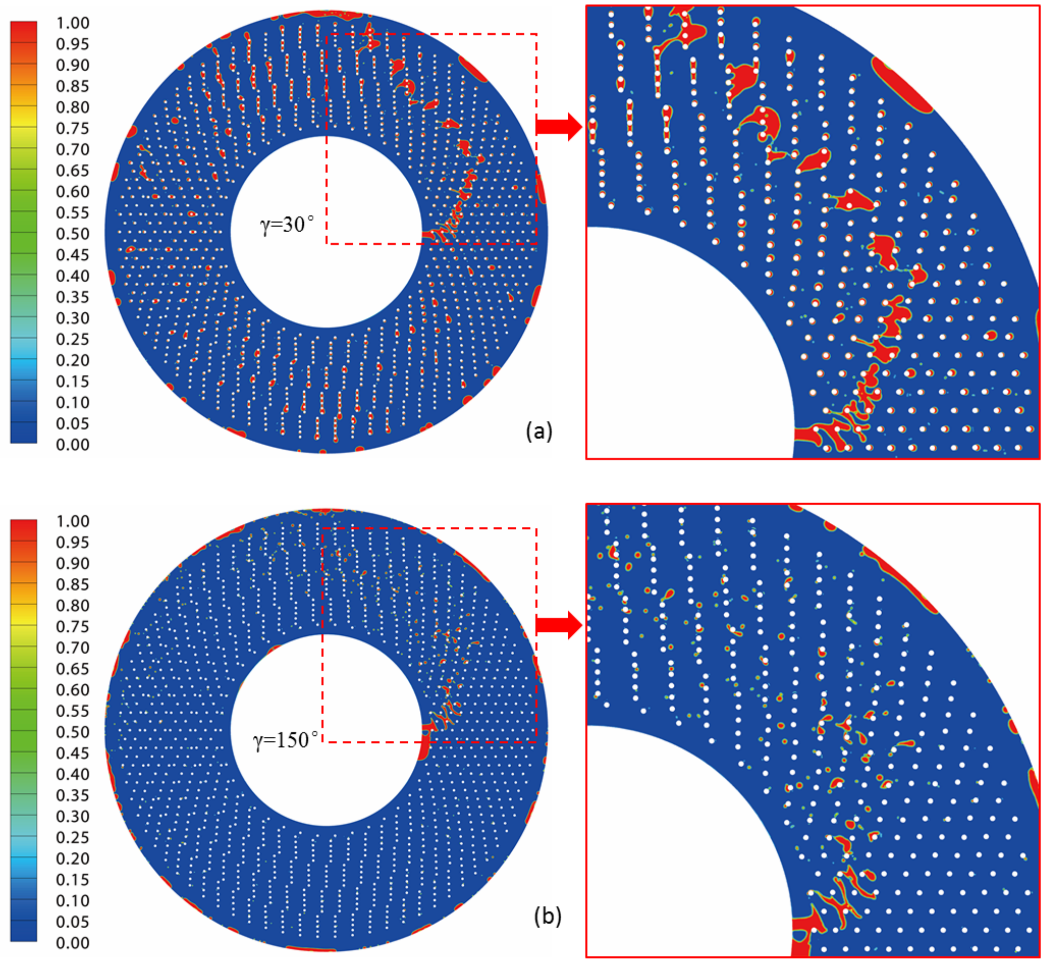

Figure 4-14 Effect of the contact angle on the liquid flow pattern (50% MEA, N=500 rpm, u_0=1.53m/s, contours represent the volume fraction of liquid).

4.3.4 Liquid dispersion

4.3.4.1 Definition of the liquid dispersion index (I_d)

The reaction between CO_2 and MEA is fast and the absorption of CO_2 is usually mass transfer limited [30], and therefore the enhancement of the CO_2 absorption in an RPB mainly depends on the liquid dispersion to increase the interfacial area. Highly dispersed liquid can generate a large gas-liquid interface and increase the surface renewal rate of the liquid due to the higher turbulence. The degree of liquid dispersion is usually assessed based on the droplet size and film thickness. However, due to the complex packing structure and the high frequent interactions between the liquid and the packing surface, different liquid shapes, such as liquid droplets, liquid films, liquid ligaments and liquid groups, co-exist in the packing region. Therefore, it is extremely difficult to assess the overall degree of liquid dispersion based on the common parameters such as droplet size and/or film thickness. In this chapter, a liquid dispersion index (I_d) is defined as follows in order to assess the degree of liquid dispersion:

$$I_d = \frac{A_{int}}{V_L} \tag{13}$$

where A_{int} is the gas-liquid interfacial area in the packing region, and V_L is the liquid volume in the packing region. In the VOF model, the liquid volume fraction (α_L) of 0.5 is used to define the gas-liquid interface [154]. The liquid dispersion index (I_d) is similar to the specific surface area of the liquid in the packing region of the RPB but it only considers the gas-liquid interfacial area, which is effective for the gas-liquid mass transfer. The liquid-solid interfacial area is not considered in this parameter.

4.3.4.2 Effect of MEA concentration and rotational speed on I_d

As shown in Figure 4-15, the liquid dispersion index (I_d) decreases with the increasing of the MEA concentration from 30 wt% to 90 wt%. This is because, with the increasing of the liquid viscosity, the film thickness increases and the size of other discrete liquid, such as the liquid droplets and the liquid ligaments, may also increase because the discrete liquid particles are mainly derived from the separation of liquid films from the packing surface. Meanwhile, at a constant rotational speed, the relative velocity between the liquid and the packing is smaller at a higher MEA concentration due to the effect of viscous damping. Therefore, the liquid breakup is more difficult to occur. In addition, it demonstrates that with the increasing of the rotational speed, I_d is substantially increased, especially from 500 rpm to 1000 rpm, where the flow pattern transforms from being a pore-dominated flow to a droplet-dominated flow (Comparing Figure 4-12 (a) and (c) or Figure 4-12 (b) and (d)).

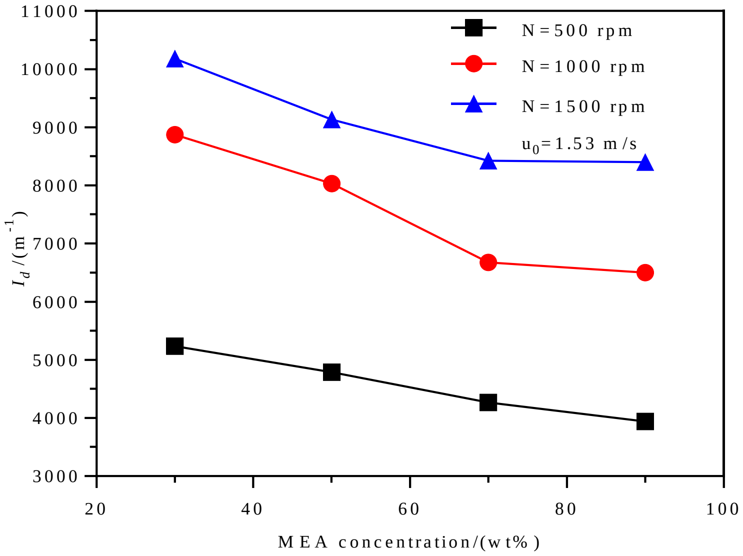

Figure 4-15 Effect of the MEA concentration on the liquid dispersion index at three different rotational speeds.

4.3.4.3 Effect of contact angle on I_d

The effect of the contact angle on the liquid dispersion index (I_d) at 500 rpm and 1000 rpm is shown in Figure 4-16, where it can be seen that when the contact angle is less than 90 degree, that is when the packing material is hydrophilic, I_d markedly decreases with the increasing of the contact angle. This is because the liquid is less likely to cover the packing surface and stretches into thin films at a higher contact angle. When the contact angle is larger than 90 degree, that is, as for the hydrophobicity packing material, the contact angle has less effect on the I_d compared to the hydrophilic materials and this may be due to the liquid mainly existing in the droplet form and almost no liquid film covers the packing surface. However, with the increasing of the contact angle, a larger percentage of small droplets are generated and this phenomenon is more dominated at lower rotational speeds. Therefore, the increased surface area due to the increasing percentage of small droplets compensates the decreased surface area due to less liquid film being formed. Therefore, the decreasing rate of I_d with increasing contact angle under a lower rotational speed is lower than under a higher rotational speed.

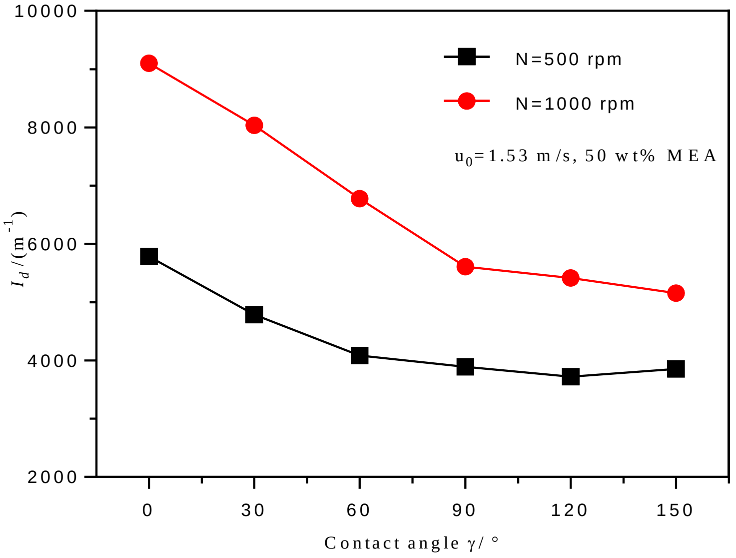

Figure 4-16 Effect of the contact angle on the liquid dispersion index at two different rotational speeds.

4.4 Conclusions

A 2D CFD model has been built to investigate the liquid behaviour in an RPB. The model has been verified through comparing the results obtained with the available experimental data [47] and the Burns correlation [56]. The results show that the 2D CFD model is effective in analysing the liquid flow characteristics in the RPB. Both the overall and local liquid flow patterns in the RPB have been analysed and distinct flow patterns have been observed in different packing regions. In the entrance region, the liquid flow is ligament-dominated flow; in the bulk region, the flow pattern is pore-dominated flow at low rotational speeds (500-1000 rpm) and droplet-dominated flow at high rotational speeds (1000-1500 rpm). The results show that the size of the entrance region increases with increasing the liquid jet velocity. With the increasing rotational speed, whilst the degree of liquid dispersion increases, the liquid holdup and residence time decrease. This is because more liquid is in droplet form and there is a thinner film flow. However, under the simulation conditions, the liquid holdup slightly increases with the increasing liquid jet velocity. When a high concentration MEA is employed, the liquid dispersion decreases but the liquid holdup and residence time increases and the effect is weak at a relatively high rotational speed. The liquid holdup and flow pattern are sensitive to the contact angle. Larger contact angles can generate more liquid droplets while smaller contact angles can generate more liquid films. The simulation results indicate that this 2D CFD modelling method has the capability of analysing the detailed liquid flow patterns, the liquid holdup, the liquid residence time as well as the degree of liquid dispersion in an RPB. Because of the acceptable computational accuracy and much smaller amount of computations compared to a 3D model, this method has the potential to be used to analyse the hydrodynamics of an industrial scale RPB.

Chapter 5: Characteristics of liquid flow in an RPB: A mesoscale 3D CFD analysis

Summary

This chapter presents a mesoscale 3D CFD modelling approach, which can be used to investigate the liquid flow in both laboratory- and large-scale RPBs in detail and accurately. A 3D representative elementary unit (REU) of the RPB has been built and validated with experimental observations, and then it is employed to investigate the gas–liquid flows at different locations, across a typical RPB, so that the overall characteristics of the liquid flow in the RPB can be reassembled. The proposed approach enables the detailed prediction of the liquid holdup, droplets formation, effective interfacial area, wetted packing area and specific surface area of the liquid within real 3D packing structures throughout the bed. New correlations to predict the liquid holdup, effective interfacial area, and specific surface area of the liquid are proposed, and the sensitivities of these quantities to the rotational speed, liquid flow rate, viscosity and contact angle have been investigated. The results have been compared with experimental data, previous correlations and theoretical values and it shows that the new correlations have a good accuracy in predicting these critical quantities. This proposed model leads to a much better understanding of the liquid flow behaviours and can assist in the RPB optimisation design and scaling up.

5.1 Introduction

At present, CFD models have been used to investigate the liquid behaviour within RPBs. Compared to the 2D VOF model as described in Chapter 4, the 3D VOF model is more accurate in simulating the liquid flow in the RPB. However, due to the extremely complex structure and small scales of the pores in the RPB, it requires an extremely large number of computational grids to resolve the pore structure. For example, if performing a 3D simulation of the RPB investigated in Chapter 4 (20 mm height, 42 mm inner diameter and 82 mm outer diameter) with the similar computational grid size as has been employed in the 2D model, then more than 100M grids are required to resolve the porous packings. Therefore, although the VOF method theoretically allows the resolution of the detailed geometry of the RPB, it is very difficult to meet the requirement of performing transient calculations for the full 3D simulation of even a laboratory-scale RPB with the appropriate accuracy.

In order to improve the understanding of the real gas/liquid flow in the pores of the packing, the detailed and more accurate 3D simulations of the flow in the real geometrical structure of the packing are necessary. However, due to the multiscale issues that have plagued the modelling of the RPB, the multiscale modelling strategy has to be taken into account and the mesoscale 3D modelling of the flow over the packing structure/pores is the most important aspect of the analysis. Therefore, in this chapter, a mesoscale CFD model is proposed to investigate the liquid flow in the RPB. The mesoscale model is based on a small 3D representative elementary unit (REU), being implemented at different locations in an RPB. Through this model, the influence of the operating conditions and the properties of the packings and liquids on the local hydrodynamic characteristics are investigated. In addition, new correlations for predicting the distribution of the liquid characteristic parameters in the whole RPB are developed based on the local data.

5.2 CFD modelling

5.2.1 Representative elementary unit (REU) of the RPB

Figure 5-1 (a) shows a cross section of the packing area of a pilot-scale RPB, with a bed of 0.1 m inner radius, 0.5 m outer radius and 0.2 m thickness, which is investigated in this chapter. The RPB is operated at 100-300 rpm and the liquid flow rate ranges from 3.6-21.6 m^3/h. In the RPB, the liquid is radially injected into the packing from the centre of the RPB through a liquid distributor. Due to the structure of the packing being repeated in the circumferential and axial directions of the RPB and the flow is dominated by the packing, the idea of a representative elementary unit (REU) is proposed in order to reduce the computational cost, which has been used in both the single-phase system [155] and the multiphase system [120, 123]. As demonstrated in Figure 5-1 (a), a small REU can be identified (Figure 5-1 (b) and (c)) at locations of interest in the RPB. Then the local liquid flow at these positions can be simulated with appropriate boundary conditions, such as the liquid flow rate and centrifugal acceleration, to the REU. The VOF model is used to capture the gas-liquid interface in the REU, and the centrifugal force field in the REU is simulated using a rotating reference frame.

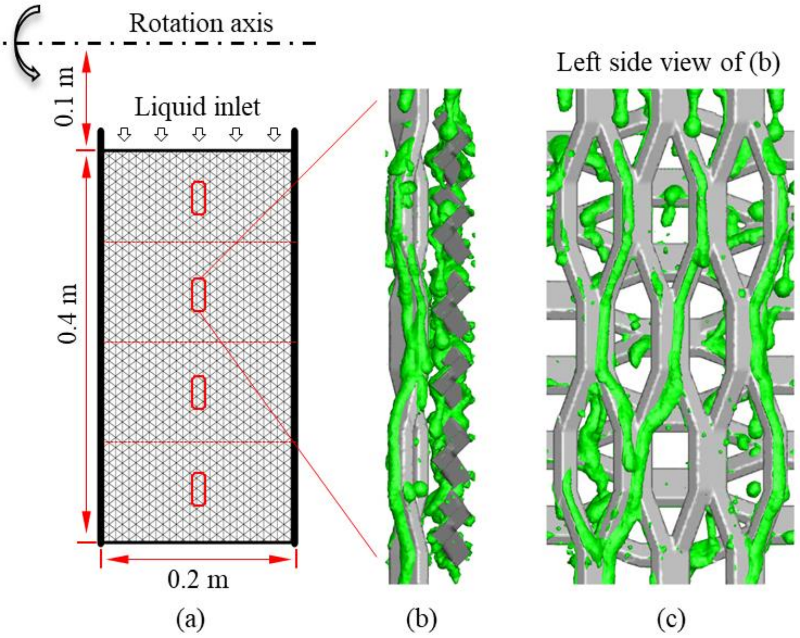

Figure 5-1 (a) Schematic diagram of the bed of the simulated RPB, (b) schematic diagram of the REU and (c) left side view of (b).

From the existing studies [45, 48, 156], there are two regions, i.e. the entrance region and the bulk region, in the packed bed of the RPB. In the entrance region, the liquid interacts with the rotating packing, and obtains the tangential velocity of the packing. As has been observed in Chapter 4, and according to the existing experimental study [45], almost all the liquid can be captured by the packing within approximately 10 mm from the entrance and the liquid closely follows the rotation of the bed. In a pilot-scale or industrial-scale RPB with a large diameter, the size of the entrance region in terms of the percentage of the bed size becomes very small. For example, if the depth of the entrance region is assumed to be 10 mm in the RPB, as investigated in this chapter, it only takes 2.5% of the total depth of the bed. Therefore, the focus of this investigation is the bulk region, and the liquid can be assumed to be evenly distributed in the circumferential direction, especially with a good liquid distributor and for liquids with high viscosity [156].

5.2.2 Structure of the packing

Special attention should be paid to the packing due to its strong effect on the gas-liquid hydrodynamics and mass transfer performance. Stainless steel meshes are widely employed as the packings of RPBs due to their high mass transfer performance [150] and their resistance to corrosion. At present, most of the stainless steel meshes used in the small scale RPBs are knitted or woven stainless steel wire mesh. However, these meshes have poor repeatability in construction as well as low mechanical strength [69], which may cause dynamic balance issues, such as an unacceptable vibration, when they are employed in a large scale RPB. Therefore, the expanded stainless steel mesh packing, which has been used for investigating CO_2 absorption by monoethanolamine (MEA) solutions [157], is employed in this chapter, as shown in Figure 5-2 (a). The mesh is manufactured through expanding the stainless steel sheet, and this enhances the material strength during the expansion, hence it has sound reliability for the industrial RPBs for long-time operation. In addition, there is almost no waste material from the manufacturing process and this is because the base metal is cut and stretched to the final form [158]. Typically, the expanded stainless steel mesh sheets are cut into annular shapes and they are stacked along the axial direction of the rotor layer by layer to form a firm packed bed. In order to increase the porosity of the packing, and make the liquid evenly distributed, the mesh is configured to be 90° between the two adjacent sheets. Therefore, every two packing layers form a repeating structure in the axial direction of the bed and the fluid flows between the two sheets from the top to the bottom (see Figure 5-1 (b) and (c)). In addition, along the radial direction from the inner periphery to the outer periphery, the packing also can be regarded as being made up of many duplicate structures. The structure of the minimum unit of the expanded metal mesh is shown in Figure 5-2 (b) and the structural dimensions of the packing are listed in Table 5-1. Based on this configuration, the specific surface area of the packing is 546.5 m^2/m^3 and the void fraction is 0.84.

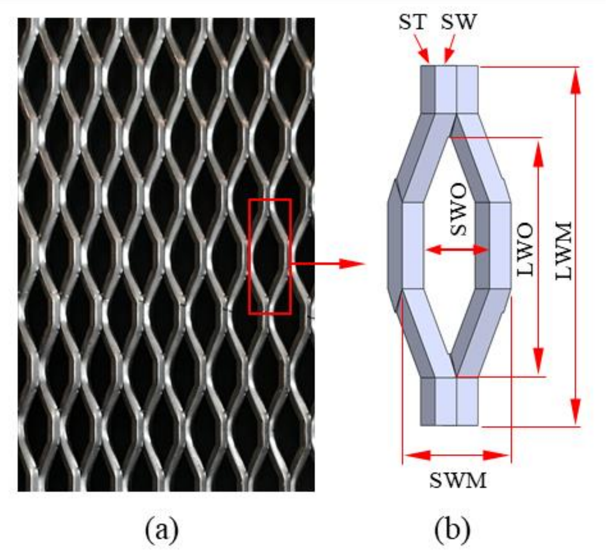

Figure 5-2 (a) Photograph of the expanded stainless steel mesh and (b) a schematic of the minimum unit.

The size of the REU is determined through considering both the periodicity of the packing and the mesh numbers. The dimensions of the REU in the circumferential and axial directions are the minimum periodic distance of the packing, which are 15.81 mm and 5.7 mm, respectively. While, due to a certain distance being required for the development of the liquid along the radial direction, the distance of the two minimum periodic units (31.62 mm) are taken as the dimension of the REU in the radial direction after investigating the effect of the liquid inlet configuration on the liquid distribution (this is discussed in Section 5.3.3).

Table 5-1. Structural dimensions of the expanded stainless steel mesh packing.

Name	Dimensions (mm)
Long way of the mesh (LWM)	15.81
Short way of the mesh (SWM)	4.78
Long way of the opening (LWO)	10.57
Short way of the opening (SWO)	2.90
Strand width (SW)	1.33
Strand thickness (ST)	0.90

5.2.3 Computational grid and boundary conditions of the REU

In order to prevent numerical difficulties associated with the quality of the grid generated, some special treatments have been adopted in the model. For example, chamfering has been performed to avoid the sharp corners at the splits. In addition, there is a 0.2 mm gap in the nearest location between the packing sheets rather than them touching each other through contact points, and this value is chosen based on trial and error. These treatments have been employed in the literature [159, 160]. Then the calculation domain is discretized with an unstructured mesh as shown in Figure 5-3. Prism grids with a higher grid density are implemented near the packing surface in order to capture the thin liquid film accurately, and in other regions, the grid is tetrahedral mesh dominate. The final grid size is a result of a grid sensitivity study, which is discussed in more detail in Section 5.3.1. In this chapter, the geometry is generated using SOLIDWORKS 2015, and the computational girds are generated using ICEM CFD 17.2.

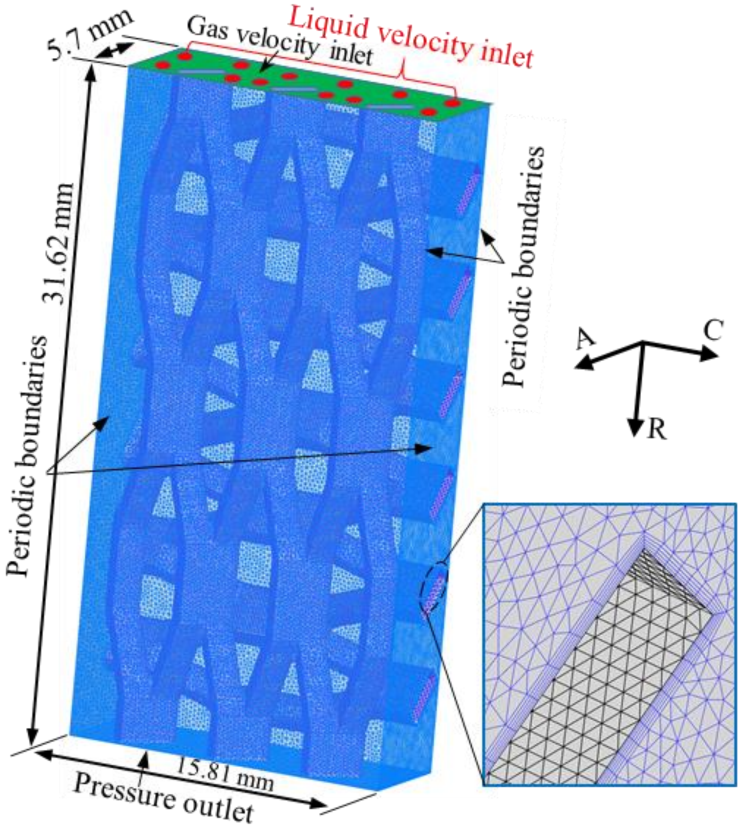

Figure 5-3 Computational domain, boundary conditions and grids for the REU (A stands for the axial direction, C stands for the circumferential direction and R stands for the radial direction in the RPB).

The liquid superficial velocity (U), namely the liquid flow rate per unit annular cross-section area of the RPB, is calculated according to the following equation:

$$U = \frac{Q_L}{2\pi r h} \tag{5-1}$$

where Q_L is the volume flow rate of the liquid, r is the radial position of the REU in an RPB, and h is the thickness of the packed bed in the axial direction of an RPB.

Therefore, for a given operating condition, the volume flow rate of the liquid feeding the REU is calculated as follows:

$$q_L = U \cdot A \tag{5-2}$$

where A is the entrance area of the REU, see Figure 5-3. Due to the short distance of the calculation domain in the radial direction compared to the radius of a pilot-scale RPB, the cross section area along the radial direction in the REU is assumed constant and equal to A.

According to the visualization study [44], and the simulations described in Chapter 4, the flow pattern in the RPB could be a combination of droplet, film and pore flows at different conditions. Therefore, it is very difficult to pre-set the liquid inlet boundary conditions to be the same as the actual flow patterns. Fortunately, investigations [161, 162] indicate that the liquid after flowing around an object will develop into different flow patterns within a short distance that mainly depends on the liquid flow rate, the surface properties of the object, etc. rather than the liquid inlet condition. Therefore, in this chapter, the liquid is set such that is fed from several evenly distributed nozzles. After the liquid flows out of the nozzles, it interacts with the packings and then quickly develops into different flow patterns at different conditions. In addition, a distance is required to make the liquid flow develop into a pseudo steady state, and the effect of the liquid inlet configuration on the liquid distribution along the radial direction in the REU is discussed in Section 5.3.3.

Many investigations indicate that the gas has little effect on the liquid flow below the flooding point [45, 57, 58], and this is mainly because the density of the gas is much lower than that of the liquid. In addition, due to the VOF model using a set of momentum equations for the gas-liquid two-phase flow, and it is not recommended to simulate the conditions for which the gas and liquid have a very large velocity difference. Therefore, the gas and liquid is set at a co-current configuration in the simulation, and the effects of the gas flow on the liquid flow characteristics are not precisely investigated in this chapter. The setting of the inlet boundary conditions of the REU is implemented through the user-defined functions (UDFs), where the liquid volume fraction is specified as unity in the liquid nozzle region, and zero in the rest of the inlet region, which is the gas inlet region (see Figure 5-3). At the inlet, the gas and liquid are assumed to have the same circumferential velocity as the packing. The radial liquid inlet velocity is calculated based on the following equation:

$$u_0 = \frac{q_L}{A_N} \tag{5-3}$$

where A_N is the total area of the liquid nozzles in the REU. The radial velocity of the gas is set as 20% of the radial liquid velocity in the gas inlet area to reduce the backflow from the outlet and accelerate convergence.

For the surface of the packing, the no-slip boundary condition and the wall adhesion are specified. However, a given packing material may have different contact angles, depending on the surface treatment technologies and the liquid properties, and for a given liquid, the contact angle also varies with different packing surfaces [103, 123, 163, 164]. In addition, the contact angle of the expanded stainless steel packing surface corresponding to different solvents is not available in the literature. Therefore, a value of 75° is specified as the contact angle of the packing surface in the initial simulations since this is within the reasonable range for stainless steel [163] and it is suitable for the packings used in RPBs [164]. Further, in order to investigate the effect of the contact angle on the flow pattern, liquid holdup and interfacial area, the contact angle ranging from 30° to 150° is studied in this chapter. Due to the thickness of the REU being much smaller than the thickness of the bed in the axial direction, most of the liquid flow in the RPB is not effected by the sidewalls of the RPB, and the liquid flow is mainly dominated by the periodic packing structure. Therefore, the periodic boundaries are used for axial simplification. In addition, due to the REU being assumed to be repeatable in the circumferential directions of the RPB, the left and right surfaces of the REU, as shown in Figure 5-3, are set to be periodic boundaries as well. The outlet boundary is set as the pressure outlet and the pressure is equal to one standard atmospheric pressure.

5.2.4 Numerical scheme

Simulations are performed using the ANSYS® Fluent 17.2 software that incorporates the in-house developed UDFs for setting the inlet boundaries. The pressure-velocity coupling is resolved by the Pressure Implicit with Splitting of the Operators (PISO) algorithm and the Body Force Weighted scheme is employed for the pressure discretization. The gradient of the variables is calculated through using the least-squares cell based method, and the warped-face gradient correction is enabled to improve the gradient accuracy for the complex unstructured grids [129]. The Geo-Reconstruct scheme is applied for the spatial discretization of the volume fraction equation, the second-order upwind scheme is employed for solving the momentum equations and turbulence equations. Due to the presence of large body forces (including centrifugal forces and surface tension forces) in the calculation domain, the “implicit body force” is enabled for improving the solution convergence by accounting for the partial equilibrium of the pressure gradient and body forces in the momentum equations. In addition, the residuals in all the equations less than 1×10^{-4} are considered as the convergence criterion for each calculation step. Different time step sizes have been tested to check the effect of the time step size on the results. As a result, the time step size is set as 5×10^{-7} s when the centrifugal acceleration is no more than 100 m/s^2 and it is less than 3×10^{-7} s when the centrifugal acceleration is between 100 m/s^2 to 300 m/s^2. In addition, the maximum number of iterations of 20 are performed per time step in order to achieve the calculation convergence. The instantaneous liquid holdup, wetted wall area and gas-liquid interfacial area are monitored for each simulation to ensure it achieves the pseudo steady state, and the average value of the parameters in each simulation are calculated based on the instantaneous value after the simulation achieves the pseudo steady state.

5.3 Model verification and validation

5.3.1 Grid convergence analysis

A verification study is undertaken to determine a reasonable computational grid size and to assess the error estimate (δ) and grid uncertainty (U_G). Three different grids consisting of 0.92, 1.40 and 2.48 million cells have been employed to investigate the effect of the grid size on the effective interfacial area A_e (defined in Section 5.4.2.1). The test liquid is 50 wt% MEA and the superficial velocity employed in the test is 0.0106 m/s. The verification is performed at two centrifugal conditions, with the centrifugal acceleration of 74.0 m/s^2 and 205.6 m/s^2, which are equivalent to the centrifugal accelerations at r=0.3 m with the bed rotational speed of N=150 rpm and 250 rpm, respectively. As shown in Figure 5-4, A_e decreases with the increasing mesh numbers at the same centrifugal field, and this is mainly due to the false diffusion errors near the gas-liquid interface decrease with the grid refinement. The U_G analysis is performed through using the Richardson extrapolation method with the recommended factors of safety (FS_0=2.45, FS_1=1.6, FS_2=6.9) proposed by Xing and Stern [165, 166]. In the factor of safety (*FS*) method, the error estimate is $\delta=P*\delta_{RE}$, where P is the distance metric to the asymptotic range and δ_{RE} is the error estimate from the Richardson extrapolation method. The detailed calculation procedure can be found in the references [165, 166] and the results of the grid convergence study are listed in Table 5-2. The convergence ratio R_K is between 0 and 1 both at g_ω=74.0 m/s^2 and g_ω=205.6 m/s^2, which means that monotonic convergence is achieved at the two typical test conditions. In addition, at the condition of 74.0 m/s^2, δ=0.96 and the relative U_G=3.42%. At the condition of 205.6 m/s^2, δ=7.92 and the relative U_G=26.07%. This indicates that at a higher centrifugal field, the dispersed liquid in the calculation domain becomes smaller, therefore, a fine grid is required in order to accurately capture the gas-liquid interface. However, a finer grid requires more computing memory and computing time. Both considering the computing efficiency and the simulation precision, the grid with 2.48M cells is used when the centrifugal acceleration is between 100 m/s^2 and 300 m/s^2, and the grid with 1.40M cells is used when the centrifugal acceleration is less than 100.0 m/s^2.

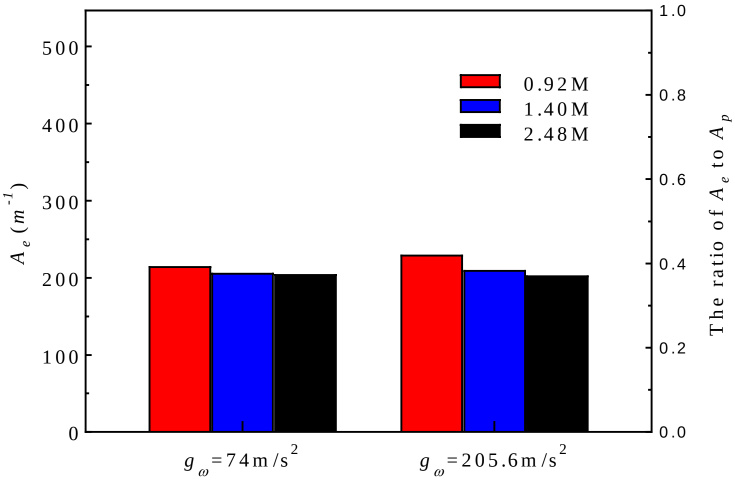

Figure 5-4 Predicted effective interfacial area using three different grids.

Table 5-2 Grid convergence study for A_e at g=74 m/s^2 and g=205.6 m/s^2.

	R_K	δ_{RE}	P	δ	U_G (%)
g_ω==74 m/s^2	0.16	0.16	5.82	0.96	3.42%
g_ω=205.6 m/s^2	0.34	2.08	3.81	7.92	26.07%

5.3.2 Comparing the CFD results with experimental data

In order to validate the CFD model then further experiments were carried out for observing the liquid flow in the expanded stainless-steel mesh packing under the force of gravity. Figure 5-5 depicts a schematic diagram of the experimental setup. Two pieces of tightly bound mesh sheets, supplied by The Expanded Metal Company in the UK are vertically fixed on a support, and the texture of the mesh is perpendicular to each other and this is the same as the arrangement of the mesh in the simulation. The liquid is supplied to the mesh from ten evenly distributed nozzles with 1 mm diameter, which are placed vertically above the mesh. The liquid flow rate is controlled by adjusting the liquid level in the tank over the mesh sheets. Several overflow drains are installed on the tank and the liquid level can be controlled at different heights by opening the different overflow drains. The liquid flow rate is measured by calculating the difference in the flow rates between the supply tank and the collecting tank. Water and 70 wt% glycerol solution are used in the experiments. In order to increase the visibility of the liquid when it flows through the mesh sheets, a small amount of blue ink (less than 2%) is added to the water. Due to the amount of blue ink being very small, its effect on the physical properties of the liquids is negligible. The experiments are carried out at ambient pressure (~1 atm) and room temperature (~20 °C). The properties of the liquids are listed in Table 3-1. A digital camera (Casio Exilim F1, Japan) with the maximum speed of 60 frames per second and the maximum resolution of 6 million pixels is used to capture the details of the liquid flow by focusing on a small region of the mesh sheets as illustrated in Figure 5-5.

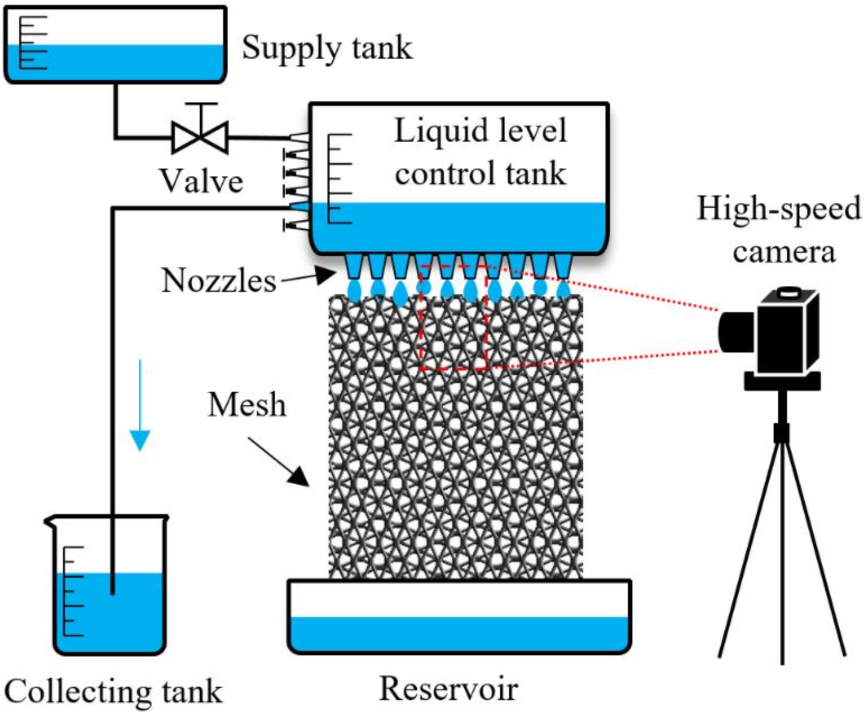

Figure 5-5 Schematic diagram of the experimental setup.

Numerical simulations of the flow through the REU have been compared with experimental observations under gravitational conditions and with the same liquid flow rates. Figure 5-6 (a1) and (a2) show the water flowing in the mesh packing obtained by the simulation and experimental methods, respectively. Figure 5-6 (b1) and (b2) show the 70 wt% glycerol aqueous solution, which has a higher viscosity than water, flowing in the mesh packing. In both cases, the liquids are released from two nozzles with 1 mm diameter above the packing region and the jet velocity is controlled at 0.5 m/s. It is clearly observed that both the water and the glycerol solution flows through the interspace of the packing, which can be classified as the pore flow. However, the high viscosity of the glycerol solution reduces the liquid velocity and increases the thickness of the liquid films on the packing surface, and thus there is more glycerol solution held on the packing.

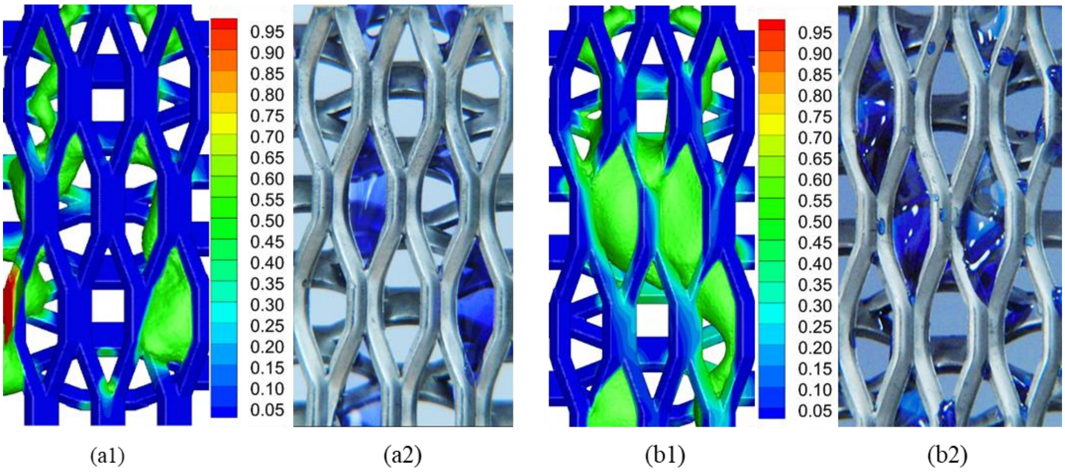

Figure 5-6 Liquid flow patterns in the expanded mesh packings: (a1) CFD simulation and (a2) experimental photograph with water flow, v=0.5m/s, and (b1) CFD simulation and (b2) experimental photograph with 70% glycerol, v=0.5m/s (VOF=0.5 is regarded as the gas/liquid interface).

Further, for performing a quantitative comparison between the CFD simulation and the experimental results, the characteristic liquid holdup, which is defined as the fraction of the liquid phase area to the total packing unit area from the photographic shooting direction, is compared. The characteristic liquid holdup is obtained through processing the experimental snapshots and the contours of the liquid from the CFD simulations. For the experimental snapshots, due to the liquid being dyed by blue ink, the liquid phase area is identified by recognising the pixels in the blue colour. From the statistical point of view, the characteristic liquid holdup can reflect the amount of actual liquid holdup. The average characteristic liquid holdup over a period of time are shown in Figure 5-7. The experimental uncertainties are based on the standard deviation of the observed results. It shows that the characteristic liquid holdup from the CFD simulations is approximately the same as those obtained from the experimental results. This demonstrates that the CFD model has a reasonable accuracy to simulate the liquid flow in the packings with complicated structures. It is worth mentioning that, in the future, further validations of the CFD model under centrifugal fields should be performed based on improved experimental measurement technologies.

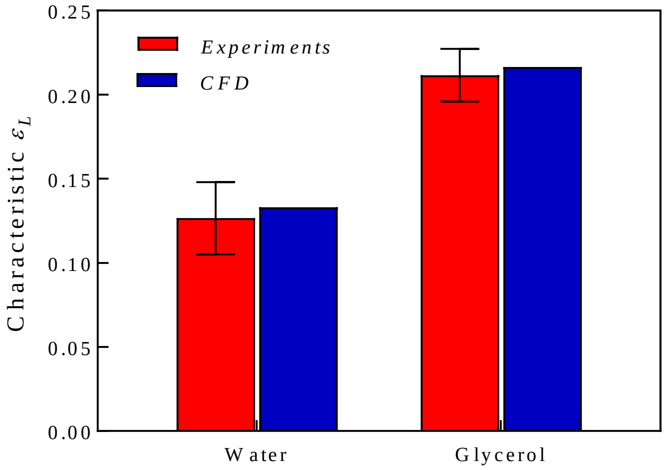

Figure 5-7 Comparison of the CFD simulation results of the average characteristic liquid holdup with the experimental data.

5.3.3 Effect of the liquid inlet configuration

In order to assess the configuration of the liquid inlet on the liquid distribution in the REU, different numbers of evenly distributed nozzles with the same total liquid flow rate and the same diameter are investigated. The diameter of the nozzle is set as 1 mm, which is close to the diameter of the droplets in the RPB as observed in the experiments [43] and the number of nozzles tested ranges from 5 to 14. The calculation domain is divided evenly into 6 regions along the radial direction from the liquid inlet boundary to the outlet boundary. The average liquid holdup (ε_L) and average specific surface area of the liquid (A_s) in each region are shown in Figure 5-8 (a) and (b), respectively.

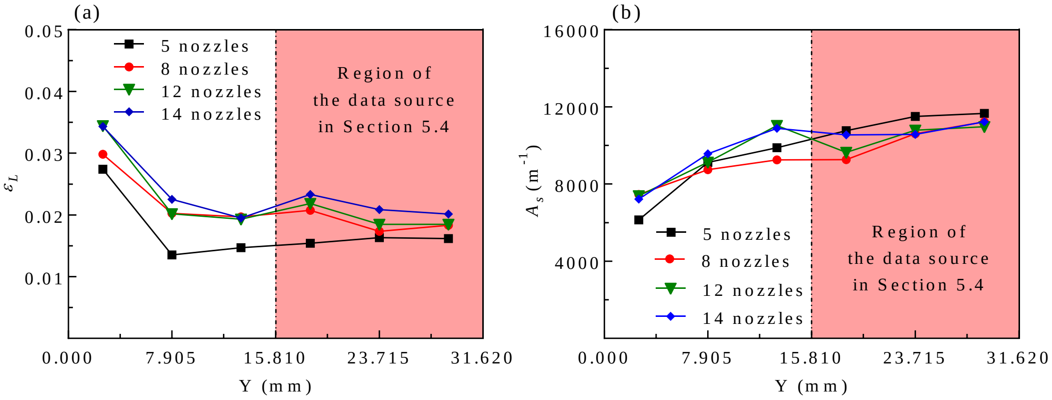

Figure 5-8 Effect of the liquid inlet configuration on the on the liquid distribution along the radial direction in the REU: (a) Liquid holdup (ε_L) and (b) specific surface area of the liquid (A_s) (g_ω=205.6 m/s^2, U=0.0106m/s, 50 wt% MEA, γ=75°).

Close to the liquid inlet nozzles, ε_L is the highest among all the regions and then it dramatically decreases in the second region. This is because the liquid impinges on the packing in the first region and accumulates here, and then it speeds up quickly under the centrifugal force. After a short distance, the centrifugal force is in balance with the drag force from the packing, and then the average speed of the liquid is almost constant. After impinging on the packing, the liquid is dispersed, and therefore A_s keeps increasing in the region that is close to the liquid entrance, as shown in Figure 5-8 (b). However, the liquid dispersion develops into a steady state within a short distance, therefore A_s remains almost constant in the region that is 15.81 mm away from the liquid entrance. Therefore, the flow patterns and data discussed in Section 5.4 are obtained from the region that is 15.81 mm away from the liquid entrance, which is half of the REU region away from the liquid inlet. In addition, with the increasing number of nozzles, the liquid holdup increases due to the decreasing liquid initial velocity, however, the increase in the liquid holdup becomes small when the number of nozzles is more than 12. Therefore, the nozzle number is set as 12 in the following investigations.

5.4 Results and discussion

5.4.1 Liquid flow patterns in the REUs

The simulated profiles (including the front, right and back views) of the liquid flows in the mesh packing with different centrifugal accelerations, liquid loads and viscosities are shown in Figure 5-9. Generally, the liquids that flow in the interspace of the packing are mainly in the form of films, ligaments and droplets, which are similar to the experimental observations [44, 45, 167]. In addition, more liquid is attached to the longitudinal wires than the latitude wires in general. Further, the dynamic behaviour of the liquid in the RPB can be observed in the simulations, where the liquid film that attaches on the packing surface flows radially under the action of the inertial centrifugal force. When the direction of the wire is not aligned with the inertial centrifugal force, the liquid film has a trend to move away from the packing surface, and if the inertia of the film is strong enough to overcome the adhesive force from the packing, the liquid will separate from the packing surface and form droplets. Then, the free droplet will hit the wires downstream of the current wire and form a liquid film. The above dynamic process is repeated in the packing region, which promotes the surface renewal of the liquid and this is advantageous for the gas-liquid mass transfer. In addition, due to the direction of the latitude wires being perpendicular to the inertial centrifugal force, more droplets are detached from the latitude wires than the longitudinal wires. Therefore, a larger percentage of the latitude wires leads to a larger percentage of droplets in the RPB, and a larger percentage of longitudinal wires generates more liquid films. However, it is worth mentioning that the influence of the packing structure and layout on the flow patterns still requires further investigations, and the use of the mesoscale CFD modelling method is a good way to perform the investigations.

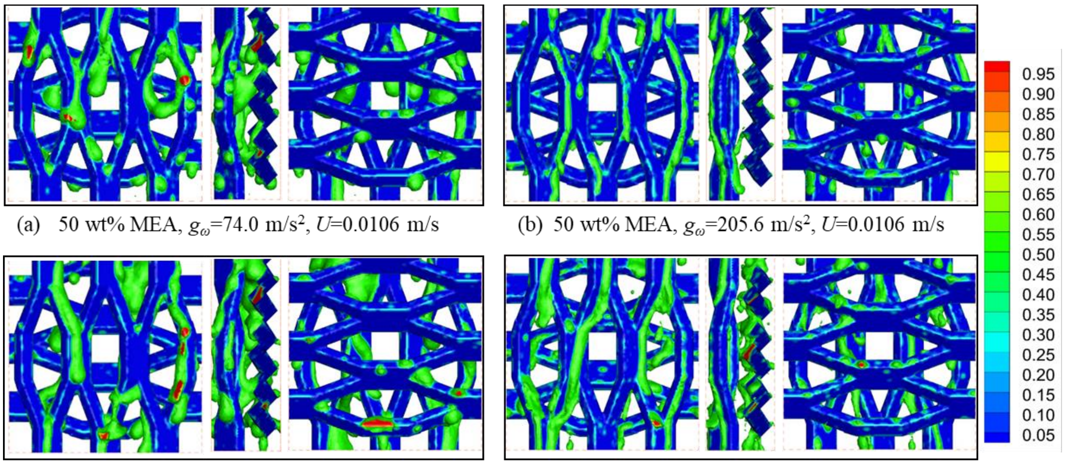

(a) 50 wt% MEA, g_{ω}=74.0 m/s^2, U=0.0106 m/s

(b) 50 wt% MEA, g_{ω}=205.6 m/s^2, U=0.0106 m/s

(c) 50 wt% MEA, g_{ω}=74.0 m/s^2, U=0.0159 m/s

(d) 90 wt% MEA, g_{ω}=205.6 m/s^2, U=0.0106 m/s

Figure 5-9 Liquid flow patterns in the REU at different conditions (γ=75°, contours represent the volume fraction of liquid, VOF=0.5 is regards as the gas-liquid interface).

In addition, the effect of centrifugal acceleration g_{ω} on the liquid flow pattern can be directly observed through comparing Figure 5-9 (a) and (b), where the values of the centrifugal acceleration are 74.0 and 205.6 m/s^2, respectively. As shown in Figure 5-9 (a), at a small centrifugal field (74.0 m/s^2), the liquid is mainly in the state of thick liquid films that attach onto the packing surface. Then, with the increasing of g_{ω}, as shown in Figure 5-9 (b), the liquid films become elongated and thinner and the droplets become smaller. The effect of liquid load on the liquid flow pattern can be observed from comparing Figure 5-9 (a) and (c), where the values of the liquid superficial velocity (U) are 0.0106 and 0.0159 m/s, respectively. As can be seen, the liquid flow patterns are similar, but the liquid volume increases with increasing U. On comparing Figure 5-9 (b) and (d), the effect of MEA concentration on the liquid flow pattern can be observed. The 90 wt% MEA, with a higher viscosity results in the thicker liquid films on the packing surface and the wetted wall area is larger than that of the 50 wt% MEA.

5.4.2 Characteristic parameters of the liquid flow in the REU

5.4.2.1 Definition of the characteristic parameters

Characteristic parameters are very helpful in characterising the liquid flow in the REU. Several important parameters, such as liquid holdup (ε_L), volume fraction of the droplets (F_d), effective interfacial area (A_e), wetted wall area (A_w), and specific surface area of the liquid (A_s), are defined in this section.

The liquid holdup (ε_L) is an essential parameter for gas-liquid reactors [55]. In the REU, it is defined as follows:

$$\varepsilon_L = \frac{V_L}{V_p} \tag{5-4}$$

where V_L is the liquid volume in the data source region of the REU (ref. Figure 5-8), and it is obtained through integrating the volume fraction of the liquid phase in each cell; V_p is the packing volume of the data source region in the REU, which includes the volume occupied by the porous packing material and the flow space.

The films that attach on the packing surface have very different flow dynamics and mass transfer mechanisms from the detached droplets. Therefore, distinguishing the droplets from the films in the REU is important for establishing an accurate mass transfer model, and the volume fraction of the detached droplets (F_d) is defined as follows:

$$F_d = \frac{V_d}{V_L} \tag{5-5}$$

where V_d is the volume of the detached droplets in the data source region of the REU.

The simulations are performed in two steps to calculate V_d. In the first step, the time-dependent computation is conducted until the flow achieves a pseudo-steady state. Then, the mass transfer simulation is performed by setting a tracer concentration boundary condition on the packing surface and solving a convective-diffusive equation to make the tracer diffuse in the liquid films that are attached to the packing surface until the simulation reaches the quasi-steady state. In this way, the liquid films that are in contact with the packing surface are marked by the tracer concentration, while the detached liquids that are mainly in the form of droplets are not marked by the tracer concentration. Further, V_d is calculated by integrating the volume of liquid that is not marked by the tracer concentration. It is worth noting that some droplets may also be in contact with the packing surface and the tracer may cause an unpredictable error.

The effective interfacial area (A_e), which is used for calculating the mass transfer and gas-liquid drag force, is defined as follows:

$$A_e = \frac{A_{GL}}{V_p} \tag{5-6}$$

where A_{GL} is the gas-liquid interfacial area in the data source region of the REU, and it is calculated through integrating the gas-liquid interfacial area in each cell (a_{GL}) of the data source region in the REU. From the viewpoint of CFD [129], a_{GL} is calculated by using the gradient of the volume fraction in each computational cell as follows:

$$a_{GL} = |\nabla \alpha_L| = |\nabla \alpha_G| \tag{5-7}$$

which has been used to calculate the gas-liquid interfacial area in the VOF models [104, 168].

In addition, the wetted wall area (A_w), which is an important parameter for predicting the drag force between the packing and the liquid, is defined as follows:

$$A_w = \frac{A_{LS}}{V_p} \tag{5-8}$$

where A_{LS} is the liquid-solid interfacial area in the data source region of the REU.

The specific surface area of the liquid (A_s) can be used to assess the degree of liquid dispersion, and it is defined as follows:

$$A_s = \frac{A_{GL}}{V_L} = \frac{A_e}{\varepsilon_L} \tag{5-9}$$

All the original data for calculating these parameters are accessed through UDFs.

5.4.2.2 Effect of the centrifugal acceleration

The centrifugal acceleration g_ω in an RPB changes with the rotational speed ω and the radial position r of the RPB. 50 wt% MEA, with a nominal viscosity of 3.39 mm^2/s, is used for simulating the typical liquid flow in an RPB for CO_2 capture. The effect of the centrifugal acceleration g_ω on the liquid holdup ε_L is examined for two liquid flow rates and the superficial velocities are 0.0053 m/s and 0.0106 m/s, respectively, which are within the typical operational conditions of the RPB. The variation of ε_L is shown in Figure 5-10 (a). On increasing g_ω from 32.9 to 296.1 m/s^2, ε_L keeps decreasing, but the downtrend gradually becomes weaker after 150 m/s^2. Variation of the droplet holdup and the volume fraction of the droplets F_d with the increasing of g_ω are shown in Figure 5-10 (b). On increasing g_ω, the inertia of the liquid increases and therefore more liquids are stripped from the packing surface and turn into the detached droplets. Figure 5-10 (c) shows the effect of g_ω on the variation of the effective interfacial area A_e and the wetted wall area A_w. It is observed that A_e slightly increases but A_w slightly decreases with the increasing of g_ω. The slight increasing of A_e is the composite effect of decreasing the liquid holdup but increasing the liquid dispersion (see Figure 5-10 (a) and (d)). While, the slight decreasing of A_w could be due to some liquid films changing into detached droplets. From the right Y-axial of Figure 5-10 (c), it is observed that A_e and A_w only take 30-40% and 10-20% of the specific surface area of the packing A_p, respectively. This demonstrates that A_e and A_w are not recommended to be regarded as A_p in the mass transfer calculations. Figure 5-10 (d) indicates that the specific surface area of the liquid A_s keeps increasing when g_ω changes from 32.9 to 296.1 m/s^2. Due to the change of A_e being very little with the increase in g_ω, the increasing of A_s is mainly due to the reduced ε_L.

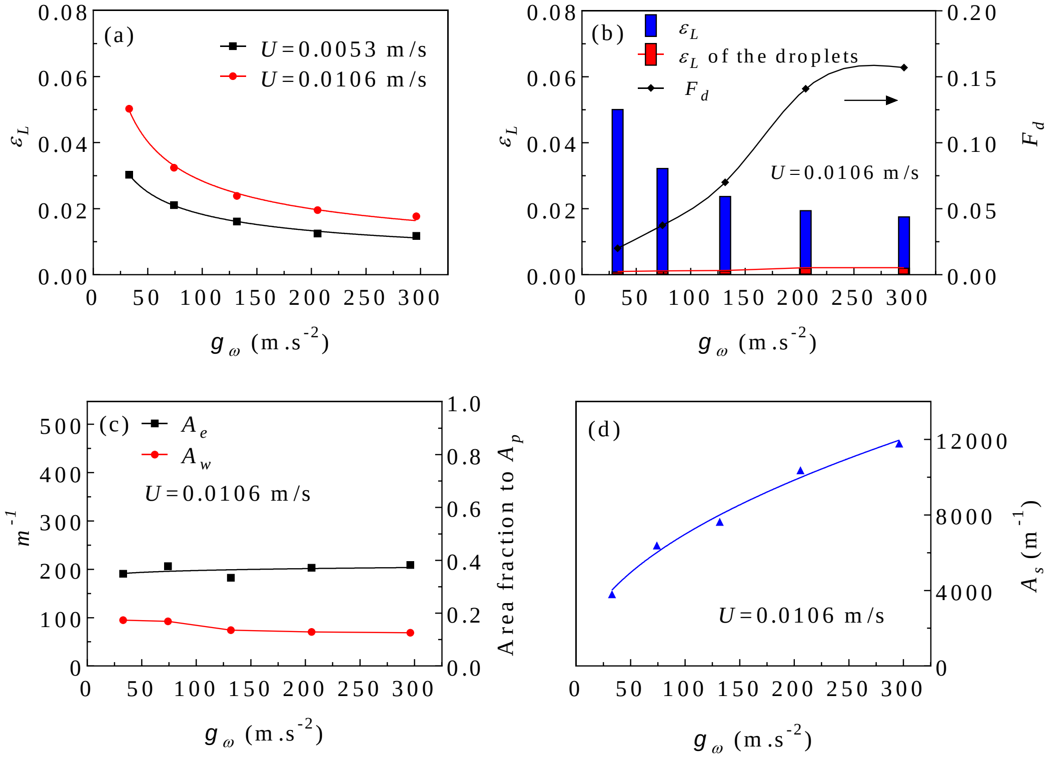

Figure 5-10 Effect of g_ω on the characteristic parameters of the liquid flow in the REU: (a) liquid holdup ε_L, (b) volume fraction of the droplets F_d, (c) effective interfacial area A_e and wetted wall area A_w, and (d) specific surface area of the liquid A_s. (50 wt% MEA, γ=75°)

5.4.2.3 Effect of the liquid load

According to Eq. (5-1) the liquid superficial velocity U in an RPB changes with the liquid flow rate Q and the radial position r of the RPB. The effect of U on the liquid flow characteristics is examined with g_ω at 74.0 m/s^2 and 205.6 m/s^2 respectively, and the liquid is set as the 50 wt% MEA. As shown in Figure 5-11 (a), ε_L increases with the increase in U from 0.0053 m/s to 0.0159 m/s, and the growth rate is higher at a lower g_ω. In addition, Figure 5-11 (b) shows that both A_e and A_w increase with increasing U. Due to the increasing rate of ε_L being larger than the increasing rate of A_e at the same g_ω, the specific surface area of the liquid A_s decreases with the increasing U, as shown in Figure 5-11 (c). This means that the degree of liquid dispersion decreases with increasing *U*.

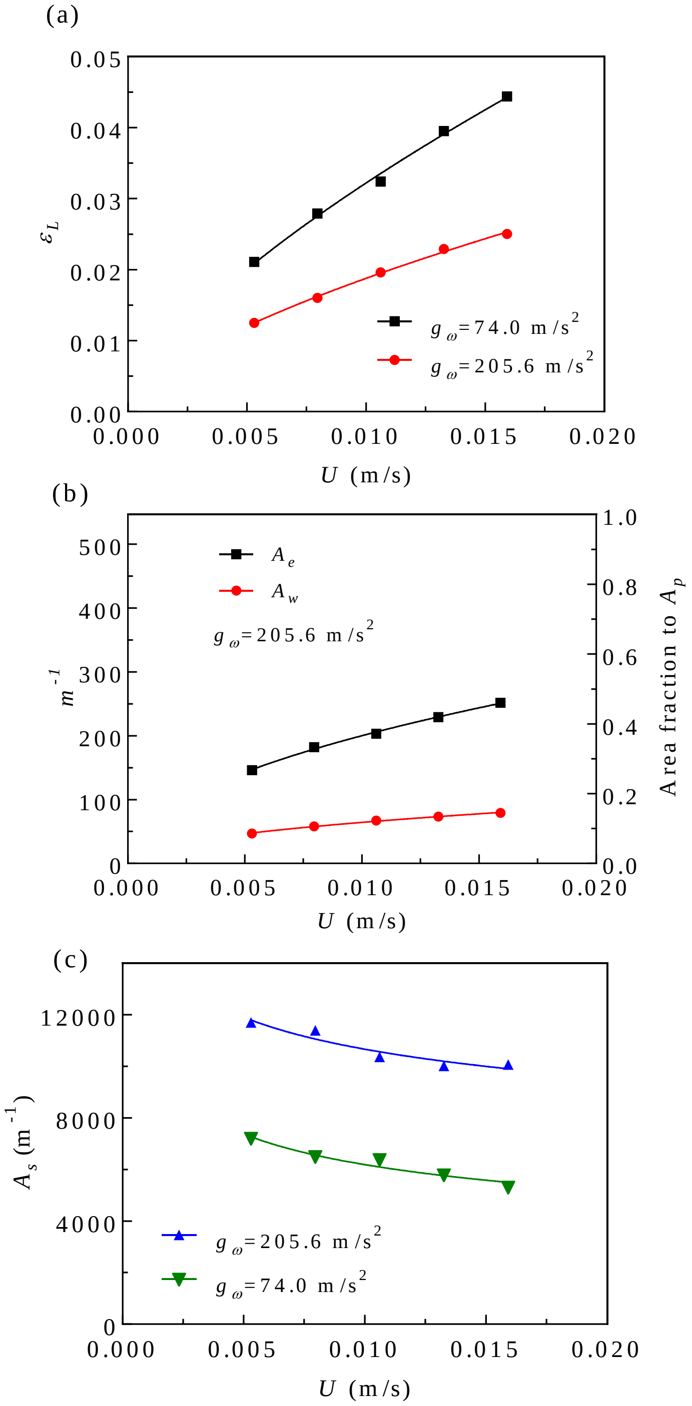

Figure 5-11 Effect of *U* on the characteristic parameters of the liquid flow in the REU: (a) liquid holdup ε_L, (b) effective interfacial area A_e and wetted wall area A_w, and (c) specific surface area of the liquid A_s. (50 wt% MEA, γ=75°)

5.4.2.4 Effect of the liquid viscosity

With the increasing of the MEA concentration, the viscosity correspondingly increases, and it has a large influence on the liquid flow in the RPB. The effect of the liquid viscosity (ranging from 1.66 mm^2/s to 10.12 mm^2/s) on ε_L and the volume fraction of the droplets F_d is shown in Figure 5-12 (a) and (b) respectively, which corresponds to the MEA concentration increasing from 30 wt% to 90 wt%. ε_L increases with the increasing viscosity, but F_d decreases. This is mainly due to the increase in the thickness of the liquid film and the decrease in the velocity of the liquid flow. In addition, if droplets strip from the liquid film, they have to overcome a greater viscous force. From Figure 5-12 (c) and (d), both A_e and A_w slightly increase with the increasing viscosity, while A_s decreases with the increasing viscosity at the same g_ω. This suggests that the increasing viscosity can weaken the liquid dispersion. Due to A_s being larger at a higher g_ω, as shown in Figure 5-12 (d), increasing g_ω could be a solution for increasing A_s when dealing with a high viscosity liquid.

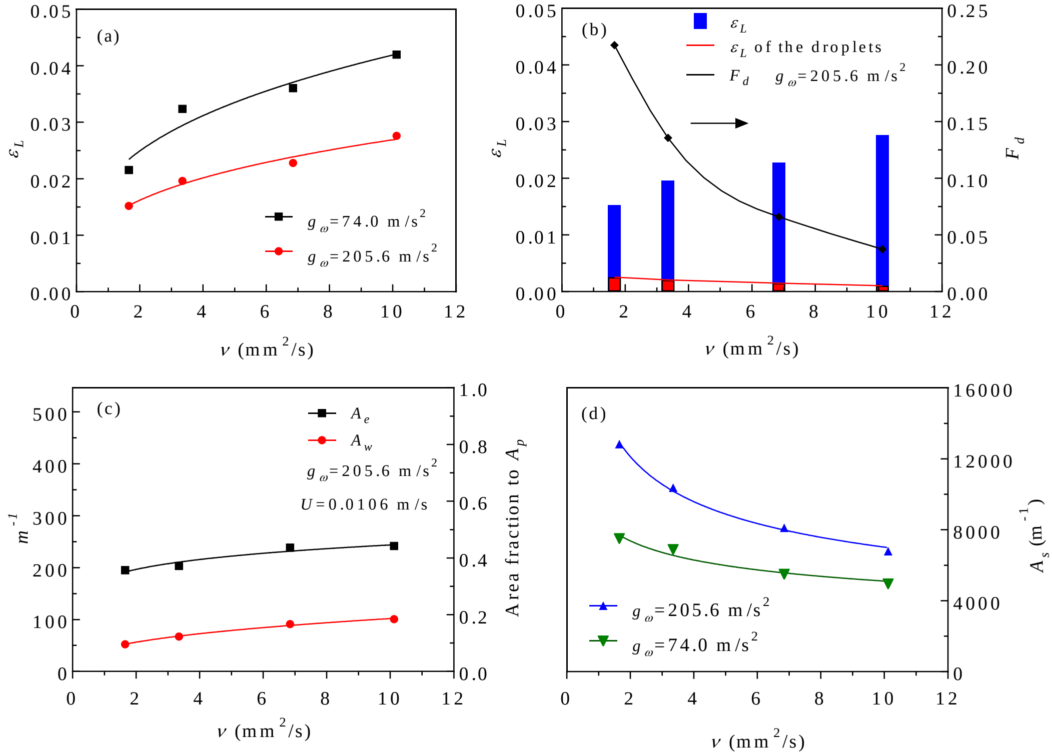

Figure 5-12 Effect of liquid viscosity on the characteristic parameters of the liquid flow in the REU: (a) liquid holdup ε_L, (b) volume fraction of the droplets F_d, (c) effective interfacial area A_e and wetted wall area A_w, and (d) specific surface area of the liquid A_s. (U=0.0106 m/s, γ=75°)

5.4.2.5 Effect of the contact angle

The contact angle γ of the packing surface is a sensitive parameter for influencing the liquid flow morphology and it further influences the mass transfer performance in a gas-liquid reactor [163]. Stainless steel is usually hydrophilic but γ is variable with different surface treatments [164]. In order to cover a wide range of properties of the packing materials, the effect of γ ranged from 30° to 150° on the liquid flow characteristics is investigated. Figure 5-13 shows the liquid flow pattern in the REU for different values of γ. It demonstrates that the liquid flow pattern gradually changes from the film-dominated flow to the droplet-dominated flow with increasing of γ. This trend also can be obtained from Figure 5-14 (b), where the volume fraction of the droplets increases with increasing γ. However, ε_L reduces with increasing γ, as shown in Figure 5-14 (a). This is because the packing has a weaker resistance to the droplets than films, and this makes the droplets have much higher velocities than the films. From Figure 5-14 (c), A_e and A_w decrease with the increasing γ. The decreasing of A_e is partly due to the decrease in liquid holdup. The decreasing of A_w is mainly due to the less wettability of the surface with increasing γ. In addition, as shown in Figure 5-14 (d), A_s increases with increasing γ, and this is mainly because the liquid is easier to break into small droplets with a hydrophobic surface, which also has been observed in the experiments of Zheng et al. [152] and Zhang et al. [164]. Moreover, a higher g_ω combined with a higher γ further promotes the breakup of the liquid.

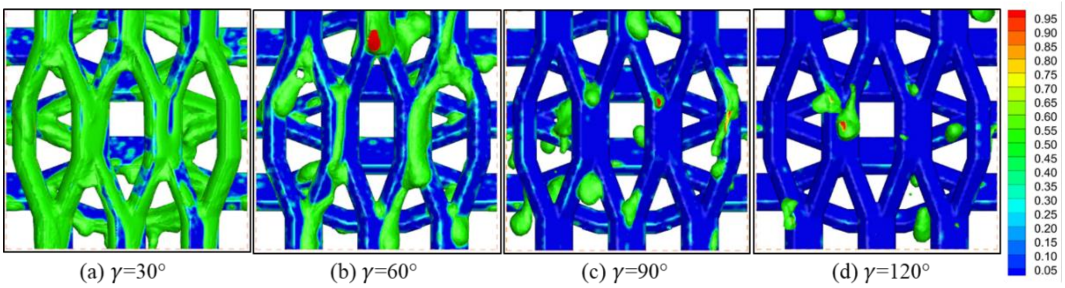

(a) γ=30° (b) γ=60° (c) γ=90° (d) γ=120°

Figure 5-13 Simulated profiles of the liquid flows in the mesh packing with different contact angles (50 wt% MEA, g_ω=74.0 m/s^2, U=0.0106 m/s, contours represent the volume fraction of liquid, VOF=0.5 is regards as the gas-liquid interface).

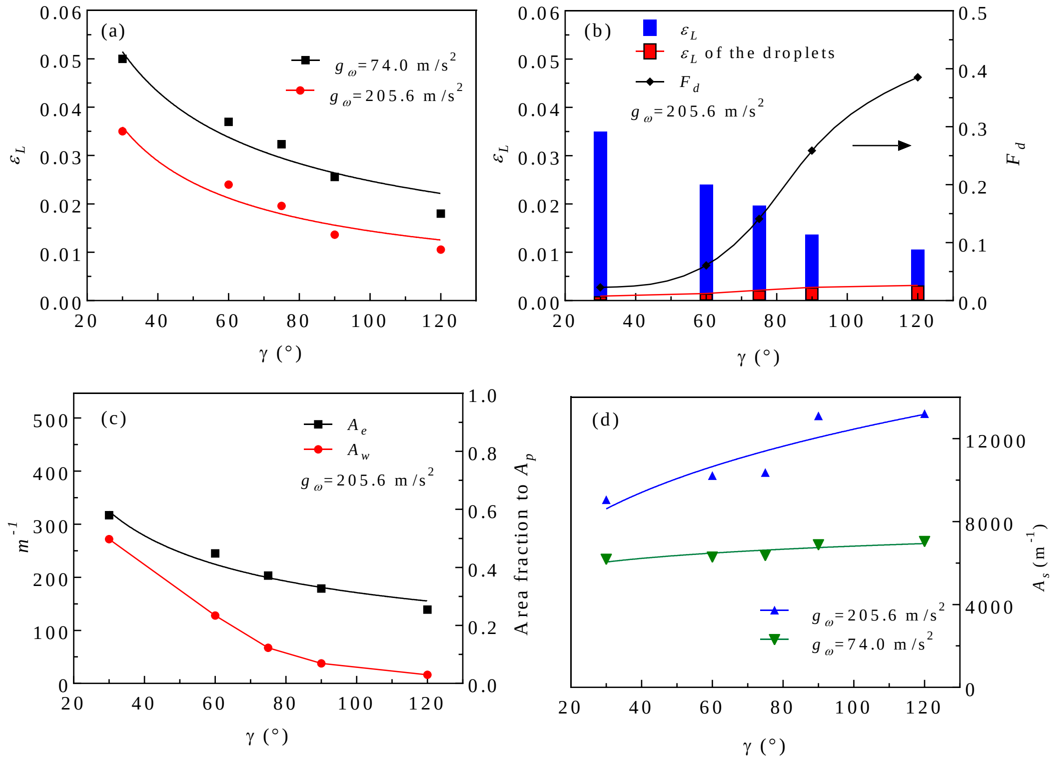

Figure 5-14 Effect of contact angle on the characteristic parameters of the liquid flow in the REU: (a) liquid holdup ε_L, (b) volume fraction of the droplets F_d, (c) effective interfacial area A_e and wetted wall area A_w, and (d) specific surface area of the liquid A_s. (50 wt% MEA, U=0.0106 m/s)

5.4.3 Correlations for ε_L, A_e and A_s

5.4.3.1 Correlations from the CFD simulation data and validations

As listed in Table 2-1 and Table 2-2, several correlations for the liquid holdup ε_L and the effective interfacial area A_e in RPBs have been proposed. These correlations are mainly obtained using mathematical regression based on numerous sets of experimental data from certain RPBs and at certain operating conditions. However, the effect of the contact angle on the hydrodynamic parameters of the RPB has not been considered in the existing correlations. In addition, there are no correlations regressed from RPBs with the expanded stainless steel mesh packing and no correlations that focus on the concentration range of the MEA solutions that aimed at CO_2 capture. Due to lack of experimental data at these conditions, generating correlations from CFD simulation data could be an effective and economical alternative to meet the requirement of accurate prediction of the performance of the RPB for CO_2 capture. Among the existing correlations, the Burns correlation [56] describes the relationship between liquid holdup (ε_L) and the centrifugal acceleration (g_ω), liquid superficial velocity (U) and viscosity (ν), which is concise and clear, and it has been adopted in many cases [39, 41, 89, 90, 169]. Therefore, a similar expression has been adopted to regress the correlations for ε_L, A_e and A_s in the RPB with an expanded mesh packing based on the CFD simulation results. Due to the contact angle having a large influence on these parameters, it has been taken into account in this model as follows:

$$y = a\left(\frac{g_\omega}{g_0}\right)^m \left(\frac{U}{U_0}\right)^q \left(\frac{\nu}{\nu_0}\right)^n \left(\frac{\gamma}{\Upsilon_0}\right)^p \tag{5-10}$$

where $\mathrm{g_0} = 205.6\ \mathrm{m/s^2}$, $\mathrm{U_0} = 0.0106\ \mathrm{m/s}$, $\nu_0 = 3.35 \times 10^{-6}\ \mathrm{m^2/s}$, $\Upsilon_0 = 75°$ are the characteristic values for g_ω, U, ν and γ in a typical operating condition. y is ε_L, A_e or A_s, and a, m, q, n, and p are the coefficients to be obtained from the regression analysis. First, this exponential function is transformed into a linear function through the logarithm operation; then the least squares regression (LSR) method is used for the regression analysis due to the weak collinearity among the independent variables [170].

The regression equations are given as follows, which are based on the 31 sets of data gathered from the CFD simulations, and the data are provided in Appendix Table A-1.

For the liquid holdup:

$$\varepsilon_L = 0.0188\left(\frac{g_\omega}{g_0}\right)^{-0.4764} \left(\frac{U}{U_0}\right)^{0.5716} \left(\frac{\nu}{\nu_0}\right)^{0.3197} \left(\frac{\gamma}{\Upsilon_0}\right)^{-0.7557} \tag{5-11}$$

For the effective interfacial area:

$$A_e = 202.3485\left(\frac{g_\omega}{g_0}\right)^{0.0435}\left(\frac{U}{U_0}\right)^{0.4275}\left(\frac{\nu}{\nu_0}\right)^{0.1200}\left(\frac{\gamma}{\Upsilon_0}\right)^{-0.5856} \quad (5\text{-}12)$$

For the specific surface area of the liquid:

$$A_s = 10517.1970\left(\frac{g_\omega}{g_0}\right)^{0.4946}\left(\frac{U}{U_0}\right)^{-0.1515}\left(\frac{\nu}{\nu_0}\right)^{-0.2921}\left(\frac{\gamma}{\Upsilon_0}\right)^{0.1658} \quad (5\text{-}13)$$

The availability of these correlations to predict ε_L, A_e and A_s at different radial positions of an RPB are examined. This is achieved through comparing the predicted results from the correlations with the new CFD simulation results, which are obtained by setting the REU at four radial positions (r=0.11, 0.3, 0.38, 0.49 m) with three rotational speeds (N=150, 250, 300 rpm). The examination is conducted at the liquid flow rate of 7.2 m^3/h, and 50% MEA are used as the liquid phase and the contact angle is set as 75°. The test data are provided in the Appendix Table A-2. From Figure 5-15 (a1), (b1) and (c1), it can be seen that the correlations have a good performance to predict ε_L, A_e and A_s with the radial position ranging from 0.1 to 0.5 m. Further, both the 31 sets of training data and the 11 sets of test data of ε_L, A_e and A_s are displayed in Figure 5-15 (a2), (b2) and (c2), and most of the data lie within ± 20% of the values predicated by Eq. (5-11), (5-12) and (5-13), respectively. This demonstrates that the correlations are valid to predict ε_L, A_e and A_s at different radial positions of an RPB.

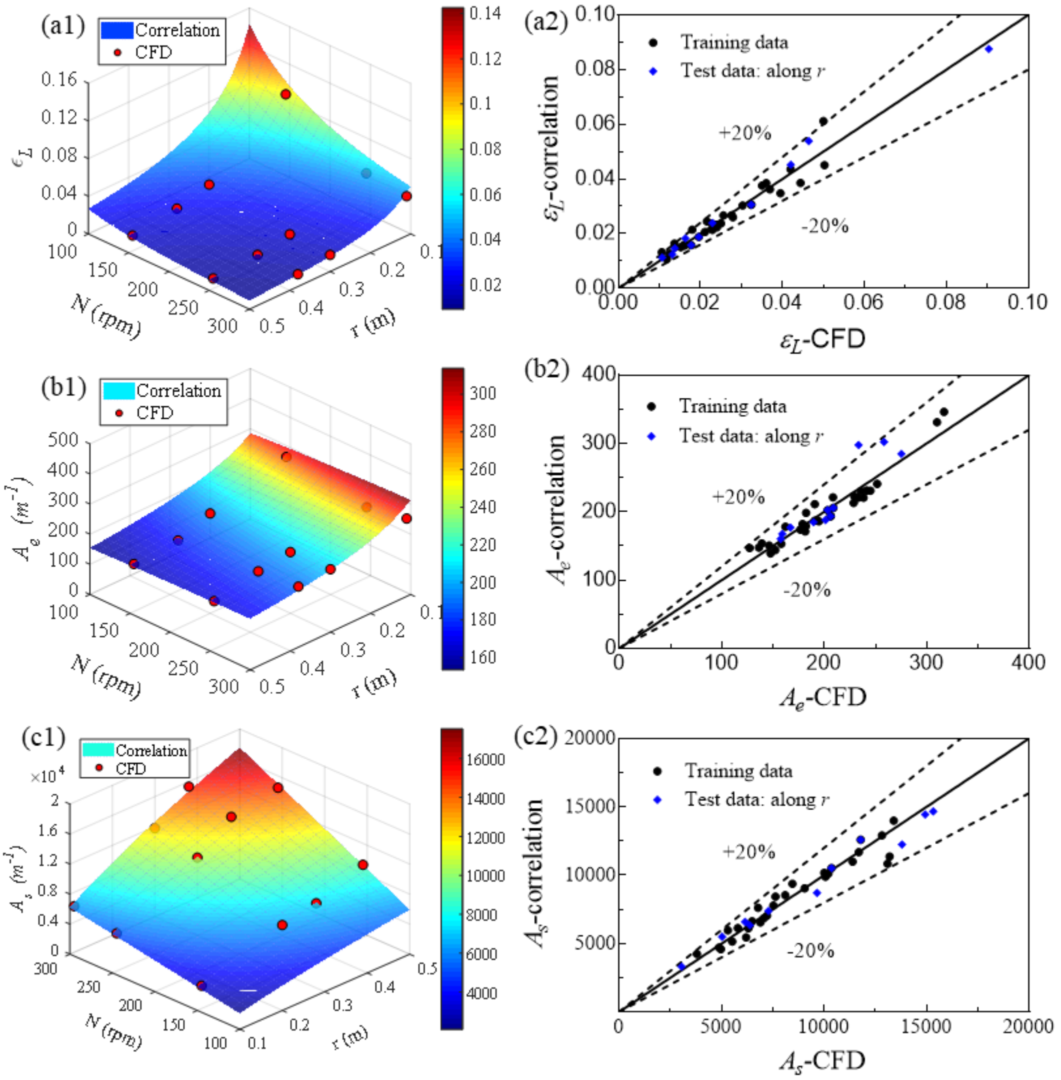

Figure 5-15 Comparison of the characteristic parameters between the predicted values from the correlations and CFD: (a) liquid holdup ε_L, (b) effective interfacial area A_e and (c) specific surface area of the liquid A_s.

In order to further validate the proposed correlation, the exponents m, q, n of the corresponding independent variables g_ω, U, ν in the ε_L correlation Eq. (5-11) are compared with previous investigations, including the exponents in the Basic and Dudukovic correlation [55], Burns correlation [56] and two theoretical models [56], as listed in Table 5-3. From the theoretical model that is summarised in Burns et al. [56], there are two extreme flow models: viscous flow and inertial flow. In the case of viscous flow, the liquid is assumed to flow as fully developed laminar films over the packing surface, then *m*= -0.33, *q*= 0.33 and *n*= 0.33. In the case of inertial flow, the kinetic energy of the flow is mainly lost by the frequent collisions with the packings, and it includes inertial film flow, pore flow and droplet flow, then *m*= -0.5, *q*= 1, *n*= 0. As can be seen in Table 5-3, the value of the exponents *m*, *q* and *n* that are derived from the CFD data are located between the limits of the two theoretical models. The absolute value of *m* is smaller but *n* is larger than the corresponding values in the Burns correlation, which suggests that there are more viscous film flows in the current investigation than in the investigation of Burns et al. [56]. This is probably caused by the different packing structures and different void fractions. The expanded stainless steel mesh packing is used in this chapter while the reticulated foam packing is used in the experiments of Burns, and the void fraction (ε) of the packing that is used in this chapter (0.84) is smaller than that in the experiments of Burns (0.953). In addition, the exponents from the current investigation are within the limits of the exponents from the experiments of Basic and Dudukovic [55], which used glass beads packings with lower void fractions (0.348 and 0.466). The comparisons between the different investigations indicates that the essential flow mode should be similar in the RPBs, although the sensitivity of the investigated parameters that influence ε_L is different for different packing structures and void fractions. The exponent of *p* for predicting the effect of the contact angle (γ) appears to be very important for influencing ε_L, but it has not been investigated in the previously mentioned investigations. Further, the new proposed correlation (Eq. (5-11)) has been used to predict the ε_L in the experiments of Burns et al. [56] and Yang et al. [47]. The experimental data of ε_L, the ε_L predicted by Lu model [101] and the new proposed correlation (Eq. (5-11)) are plotted in Figure 5-16 (a) and (b). It is observed that the predicted ε_L is close to the experimental data [47, 56] and the predictions of the Lu model [101].

Table 5-3 Comparison of the exponents m, q, n and p for ε_L.

Data Source	Packing type	m (of g_ω)	q (of U)	n (of ν)	p (of γ)
ε_L-CFD	Expanded stainless steel mesh packing (ε=0.84)	-0.4764	0.5716	0.3197	-0.7557
ε_L-Theoretical inertial model		-0.5	1.0	0	--
ε_L-Theoretical viscous model		-0.33	0.33	0.33	--
ε_L-Burns	Reticulated foam (ε=0.953)	-0.5	0.6	0.22	--
ε_L-Basic and Dudukovic	Glass beads (ε=0.348, 0.466)	-0.48~ -0.36	0.57~ 0.64	0.23~ 0.51	--

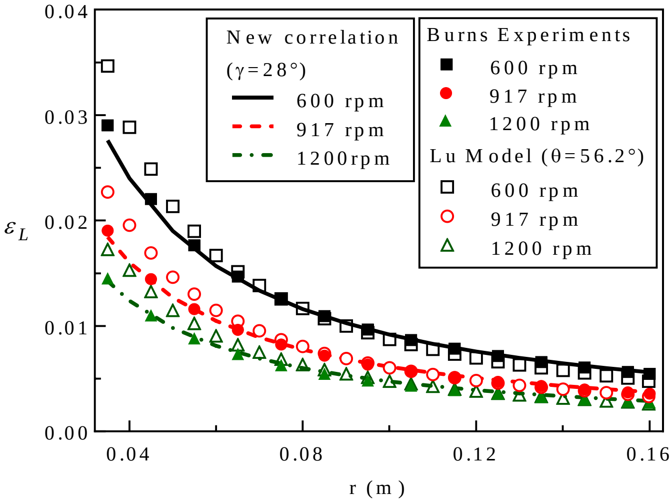

(a)

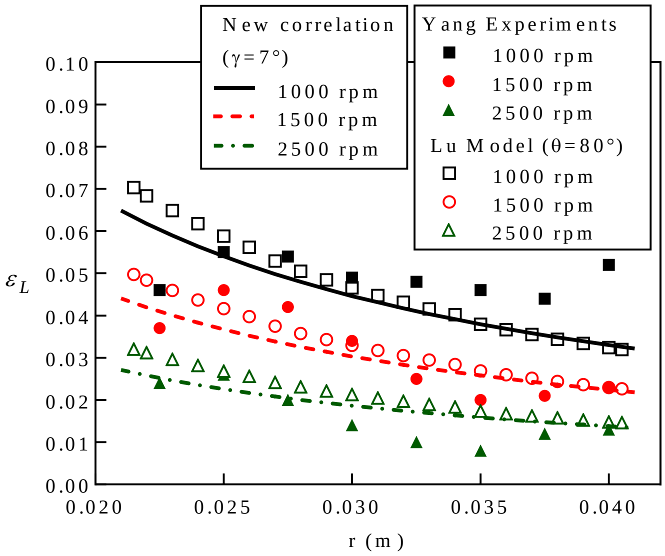

(b)

Figure 5-16 Comparison of the $\boldsymbol{\varepsilon}_L$ between the new correlations, experimental data and existing model [101]: (a) Burns case (Q_L=1.75*10^{-5} m^3/s) [56] and (b) Yang case (Q_L=2.29*10^{-5} m^3/s) [47].

5.4.3.2 Practical implications of the correlations

In order that the correlations explicitly connect to the practical operations, the centrifugal acceleration g is decomposed into the radial position r and the rotational speed ω based on the following equation:

$$g_{\omega} = r\omega^2 \tag{5-14}$$

Therefore, on substituting Eq. (5-1) and Eq. (5-14) into Eq. (5-10), then Eq. (5-10) becomes:

$$y = E\omega^{2m}{Q_L}^{q}r^{(m-q)}\nu^{n}\gamma^{p} \tag{5-15}$$

where E is an empirically derived constant.

The independent variables in Eq. (5-15) cover most of the important parameters in the operation and design of an RPB. For example, ω and Q_L are the main operating parameters and both of them are highly relevant to the operating cost in the CO_2 capture process. Further, r is the important structural parameter that is relevant to the volume and weight of the bed, ν is the physical property of the solvents that flows in the RPB, and γ is the property of the packing materials. Therefore, analysing the exponents of these parameters has very important practical implications.

Table 5-4 lists the exponents of ω, Q_L, r, ν and γ for predicting ε_L, A_e and A_s. A positive exponent means the dependent variable has a positive correlation with the independent variable, and vice versa. In addition, the absolute value of an exponent represents the sensitivity of the dependent variables to the change in the corresponding independent parameters.

Table 5-4 Comparison of the exponents ω, Q_L, r, ν and γ for predicting ε_L, A_e and A_s.

Parameters	$2m$ (of ω)	q (of Q_L)	m-q (of r)	n (of ν)	p (of γ)
ε_L	-0.9528	0.5716	-1.048	0.3197	-0.7557
A_e	0.0870	0.4275	-0.384	0.1200	-0.5856
A_s	0.9892	-0.1515	0.6461	-0.2921	0.1658

(i) For ε_L, the exponents of Q_L, ν are positive, and the exponents of ω, r and γ are negative, in addition, the sensitivity of the independent variables is ranked as follows: $r > \omega > \gamma > Q_L > \nu$. This means that the viscosity ν is the weakest parameter while the radial position r is the strongest parameter for influencing ε_L. Moreover, the exponent of r is approximately -1, which means ε_L almost reduces inversely proportional to the local packing radius in an RPB. Therefore, for the scale up design of an industrial scale RPB for CO_2 capture, the radial thickness of the rotating packed bed should not be too large in order to prevent the severe liquid maldistribution along the radial direction in the RPB. In addition, enlarging the RPB in the axial direction or the design of RPBs with multistage liquid nozzles along the radial directions could be the feasible solutions.

(ii) For A_e, the exponents of ω, Q_L and ν are positive, and the exponents of r and γ are negative. In addition, the sensitivity of the independent variables is ranked as follows: $\gamma > Q_L > r > \nu > \omega$. This indicates that within the investigation conditions in this chapter, in order to increase A_e, decreasing the contact angle γ could be the most effective option, while increasing the rotational speed ω is the most inefficient way. Therefore, a high rotational speed is not recommended in order to achieve a large A_e by both considering the performance of the RPB and the energy consumption for driving the RPB.

(iii) For A_s, the exponents of ω, r and γ are positive, and the exponents of Q_L and ν are negative. The sensitivity of the independent variables is ranked as follows: $\omega > r > \nu > \gamma > Q_L$. This indicates that increasing ω is the most effective way to increase A_s.

In addition optimizing a single characteristic parameter, multiple characteristic parameters should be considered for optimizing a particular application of the RPB. From the aspect of CO_2 absorption [171], increasing A_e is the first choice to facilitate the CO_2 absorption rate in the RPB. According to the correlation for A_e, both increasing Q_L and decreasing γ are two effective solutions to increase A_e. However, both of the two solutions have negative impacts on A_s, which reduces the utilization efficiency of the solvents. Due to A_s being very sensitive to ω, an appropriate increase in ω could reduce the side effects of increasing A_e which resulted from the increase in Q_L and the decrease in γ. In addition, using high-concentrated aqueous MEA solutions has good potential to reduce the volume ratio of the solvents to CO_2, which can reduce the energy consumption in MEA regeneration. However, the increasing viscosity ν decreases A_s, which could decrease the utilization efficiency of MEA. Therefore, increasing ω and/or increasing γ appropriately are possible solutions to deal with this issue through analysing the exponents.

5.5 Conclusions

This chapter proposes a new mesoscale 3D CFD model to investigate the liquid flow characteristics in the RPB for CO_2 capture. The model has been validated through comparing the results obtained with experimental data. Detailed liquid flow patterns, liquid holdup, volume fraction of the droplets, effective interfacial area, wetted wall area and specific surface area of the liquid in the RPB are obtained numerically. The results show that the mesoscale CFD model is effective in analysing the local detailed liquid flow characteristics as well as the overall parameters of an RPB. The main conclusions are as follows:

(i) Increasing the rotational speed dramatically reduces the liquid holdup and increases the specific surface area of the liquid but it has very weak positive effect on increasing the effective interfacial area in the RPB.

(ii) Increasing liquid flow rate and/or increasing liquid viscosity improve both the liquid holdup and the effective interfacial area in the RPB, but they have a negative effect on the specific surface area of the liquid. Higher liquid flow rate and/or higher viscous MEA require higher rotational speed to maintain both the effective interfacial area and the specific surface area.

(iii) The flow pattern, liquid holdup and interfacial area are sensitive to the contact angle. Larger contact angles can generate more liquid droplets with larger specific surface area but the liquid holdup, the effective interfacial area and the wetted wall area dramatically decrease. Surface modification of the packing is an important method to optimize the mass transfer efficiency in the RPB.

(iv) The correlations for predicting the liquid holdup ε_L, effective interfacial area A_e, and specific surface area A_s in the RPB are proposed. The sensitivities of the investigated effect parameters on ε_L, A_e and A_s, respectively, are as follows: For ε_L, $r > \omega > \gamma > Q_L > \nu$; For A_e, $\gamma > Q_L > r > \nu > \omega$; For A_s, $\omega > r > \nu > \gamma > Q_L$.

In general, a much better understanding of the liquid flow behaviours within the RPB has been achieved and the factors that influence the mass transfer has been analysed in depth. The proposed model provides a feasible way to predict the hydrodynamic performance of the RPB, which could assist to optimize the design and operation of the RPBs for CO_2 capture.

Chapter 6: CFD simulations of CO_2 absorption in an RPB

Summary

This chapter employs an Eulerian two-phase flow model to analyse the CO_2 *absorption by monoethanolamine (MEA) solutions in an RPB. Only the packing region of the RPB is modelled, and the investigation is performed using a 2D axisymmetric swirl model in order to save on the calculation resource and time. In this chapter, the interfacial area correlation, which is obtained from the 3D mesoscale VOF simulation in Chapter 5, is used to estimate the interfacial area in the packing region of the investigated RPB. In addition, the reactive mass transfer model and the heat transfer model are integrated in the Eulerian model, and the integrated model successfully simulates the* CO_2 *capture from the flue gas by MEA solutions in the RPB. The model is validated through comparing the predicted results with the experimental data and existing correlations. In addition, the effects of the rotational speed, the gas and liquid flow rate, the MEA concentration, and the liquid inlet temperature on the overall gas phase mass transfer coefficient (*K_Ga*), the* CO_2 *removal efficiency and/or the pressure drop in the RPB are investigated using this model.*

6.1 Introduction

Accurate prediction of the CO_2 absorption by amine solutions is very important for RPB design and operation optimization for large-scale CO_2 capture. Due to the very high demand of the computational resources, it is very difficult to perform the mass transfer simulation for pilot-scale or large-scale RPBs using the VOF-based method. On considering the computing efficiency, the Eulerian method is advantageous for the CFD simulations of pilot-scale and large-scale RPBs. However, the Eulerian method cannot resolve the gas-liquid interface where the mass transfer occurs, therefore it requires a submodel to predict the gas-liquid interfacial area in the RPB. As a solution, the interfacial area correlation that is obtained from the VOF simulation, as described in Chapter 5, is employed in the Eulerian model. Therefore, a comprehensive multiscale modelling strategy is presented in this chapter, as illustrated in Figure 6-1, which can be used to simulate CO_2 absorption by MEA solutions in RPBs. Finally, effects of the operating parameters, such as rotational speed, gas and liquid flow rate, MEA concentration and temperature, on the CO_2 absorption and pressure drop are investigated through using the proposed modelling method.

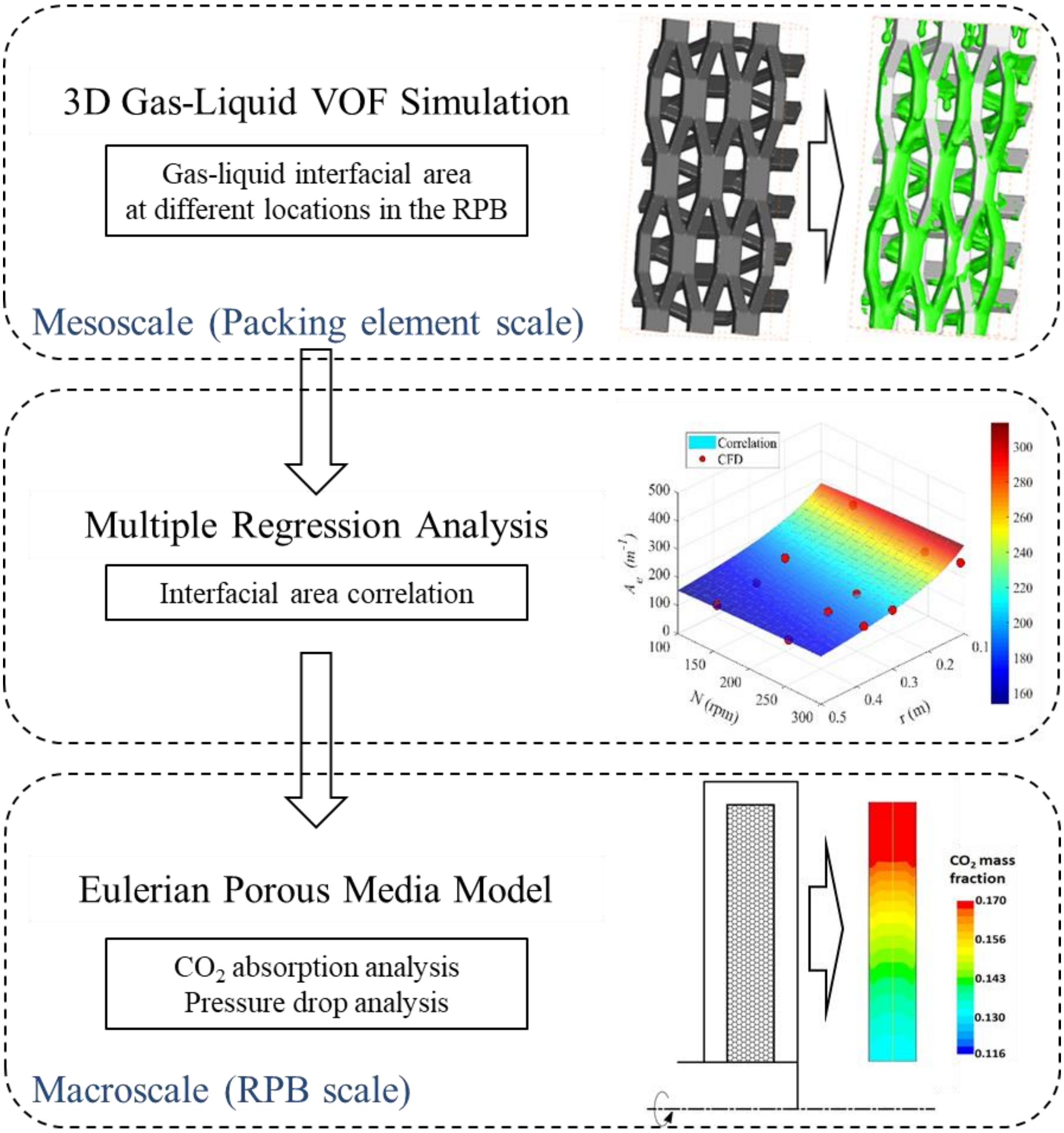

Figure 6-1 An overview of the multiscale approach for modelling the CO_2 absorption in an RPB.

6.2 CFD modelling

6.2.1 Introduction of the investigated RPB test rig

The RPB simulation is based on the experiments of Lee et al. [31], and a photograph of the RPB test rig is shown in Figure 6-2. The important dimensions of the RPB and the specifications of the used packing are listed in Table 6-1.

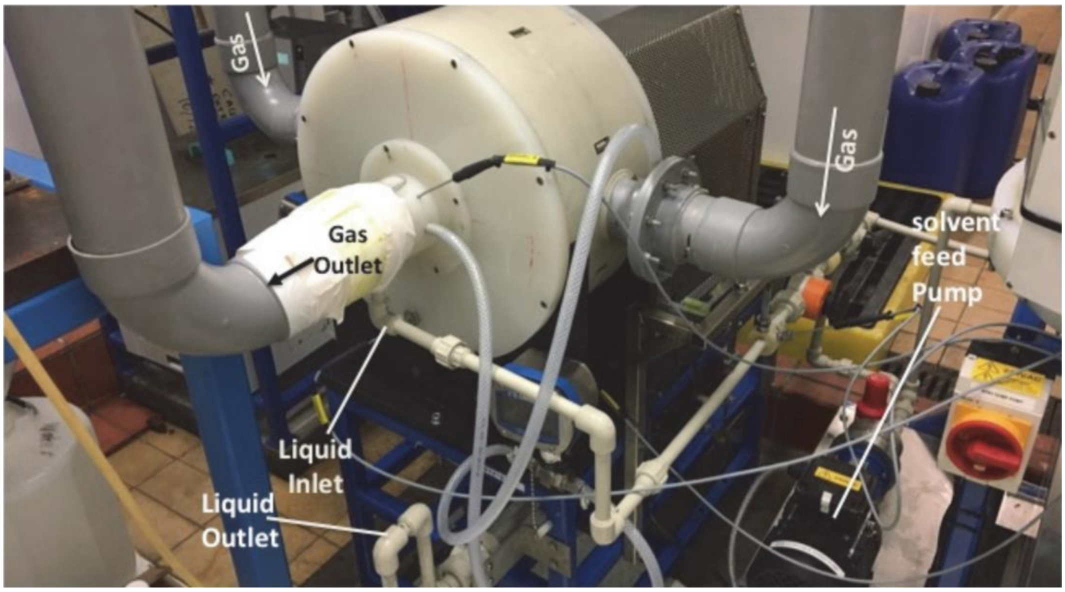

Figure 6-2 Photograph of the RPB test rig for CO_2 absorption by aqueous MEA solutions [31].

Table 6-1. Dimensions of the RPB and the packing specifications.

Name	Dimensions (or specifications)
Diameter of the casing	360 mm
Inner diameter of the packed bed	80 mm
Outer diameter of the packed bed	300 mm
Thickness of the packed bed	20 mm
Structure and material of the packing	stainless steel expanded mesh
Voidage of the packing	0.801
Specific surface area of the packing	663 m^2/m^3

A simplified flow diagram of the RPB test rig for CO_2 absorption by aqueous MEA solutions is shown in Figure 6-3. As can be seen, the mixed air and CO_2 in the ratio of 12 mol% CO_2 was used to simulate the actual flue gas in the experiments, and first it was preheated to 40 °C by a heating system and then it entered the RPB from the gas inlet that was mounted at the outer boundary of the RPB. After flowing through the RPB, the gas left the RPB through the pipe that was connected to the inner boundary of the RPB. The MEA solution was first preloaded to 0.1 mol CO_2 / mol MEA and was preheated to 40°C by a heating system, and then it was injected into the RPB through using a liquid distributor that was mounted at the centre of the RPB. After flowing through the packing area of the RPB, the liquid was collected by the case wall and flowed out of the RPB through a pipe that was situated at the bottom of the case.

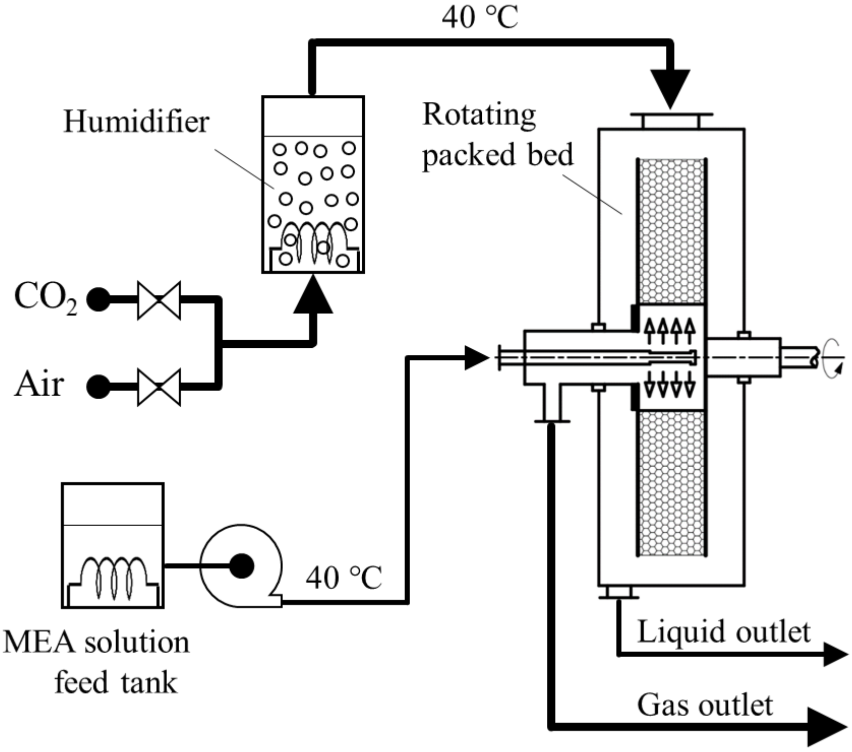

Figure 6-3 Simplified flow diagram of the RPB test rig for CO_2 absorption by aqueous MEA solutions based on [31].

6.2.2 Calculation domain and boundary conditions

The actual structure of the RPB is complicated, and it is very difficult to make the CFD model identical to the actual test rig. Therefore, only the prime functional region of the

RPB, that is the packing region, is investigated in this chapter, see Figure 6-4. In addition, some assumptions for simulating the gas-liquid flow and mass transfer in the packing region of the RPB are summarised as follows: (i) the liquid is assumed to be evenly injected into the packing region of the RPB in the circumferential direction; (ii) the gas is assumed to be evenly fed into the packing region in the circumferential direction from the outer edge of the packing; (iii) both the gas and the liquid are incompressible fluids; (iv) the gas and liquid flows in the RPBs are assumed to be in steady-state. Based on the above assumptions, an axisymmetric swirl flow model was performed in a 2D calculation domain in order to investigate the flow and mass transfer phenomena in the RPB.

A schematic diagram of the geometry employed in the CFD simulations is shown in Figure 6-4. The dimensions of the simulated packing region of the RPB is the same as that in the experimental RPB test rig [31]. The radial length and axial width of the porous media region, i.e. the packing region of the RPB, is 110 mm and 20 mm, respectively, and the inner boundary of the porous media region is 40 mm from the rotational axis. In addition, as has mentioned in Section 3.4.2, the liquid inlet and gas outlet, and the liquid outlet and gas inlet of the packing region are overlapped, respectively. In order to overcome the difficulties of setting the overlapped boundary conditions, two regions for the liquid generation and elimination have been designed. The liquid generation region is next to the inner boundary of the porous media region, which has a radial length of 1 mm, and the liquid elimination region is next to the outer boundary of the porous media region, which has a radial length of 1 mm.

The gas inlet and gas outlet are specified through using velocity inlet and pressure outlet boundary conditions, respectively. The pressure at the gas outlet is assumed to be the atmospheric pressure. In addition, it is worth mentioning that there is a transition region between the liquid generation region and the gas outlet, which is designed to avoid the generated liquid flow through the gas outlet directly. The left and right sides of the calculation domain are set as wall boundary conditions. In order to simulate the centrifugal field in the packing region, the calculation domain is fixed in a rotational reference frame with different rotational speeds.

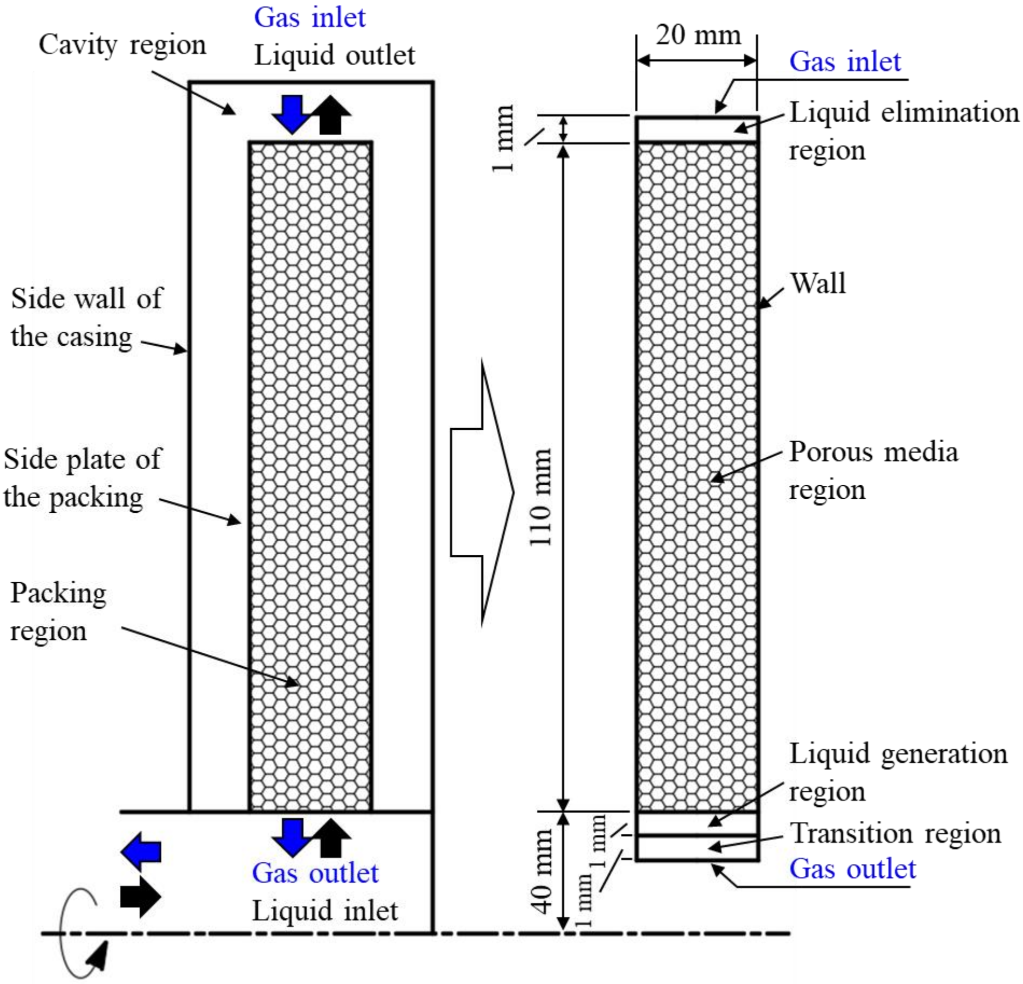

Figure 6-4 Schematic diagram of the simplified calculation domain of the RPB and its boundary conditions [172].

6.2.3 Properties of the fluids

In the simulation, the injected gas contains 12 mol% CO_2 and 88 mol% N_2, which can be used to simulate the real flue gas. The MEA solutions are preloaded to 0.1 mol CO_2/ mol MEA before being injected into the RPB as described in the experiments [31], and the preloaded CO_2 in the liquid phase is assumed to react with the MEA component and forms $MEAH^+$ and $MEACOO^-$ in the solutions (ref. Equation (3-55). Based on this assumption, the mass fraction of each chemical components in the MEA solutions are listed in Table 6-2.

Table 6-2 Mass fraction of the chemical components in the MEA solutions with different concentrations.

	Chemical components (mass fraction)			
MEA Concentration	MEA (C_2H_7ON)	$MEAH^+$ ($C_2H_8ON^+$)	$MEACOOH^-$ ($C_3H_6O_3N^-$)	H_2O
30 wt% MEA	0.2349	0.0298	0.0501	0.6852
40 wt% MEA	0.3110	0.0395	0.0663	0.5832
50 wt% MEA	0.3861	0.0491	0.0823	0.4826
70 wt% MEA	0.5331	0.0677	0.1136	0.2856
90 wt% MEA	0.6761	0.0859	0.1441	0.0939

The density of the liquid is assumed to be constant in each simulation, and the values are estimated from the experimental data of Amundsen et al. [137]. The viscosity varies greatly with temperature, therefore the values of viscosity are estimated by curve-fitting to the experimental data of Amundsen et al. [137], and the fitting correlations are listed in Table 6-3.

Table 6-3 Viscosity of the MEA solutions at different temperatures.

MEA Concentration	Viscosity (kg/m/s) 298K ≤ T ≤ 353K
30 wt%	$0.3083 - 2.621 \times 10^{-3}T + 7.488 \times 10^{-6}T^2 - 7.173 \times 10^{-9}T^3$
40 wt%	$0.4829 - 4.086 \times 10^{-3}T + 1.160 \times 10^{-5}T^2 - 1.103 \times 10^{-8}T^3$
50 wt%	$0.7963 - 6.744 \times 10^{-3}T + 1.915 \times 10^{-5}T^2 - 1.821 \times 10^{-8}T^3$
70 wt%	$2.398 - 2.056 \times 10^{-2}T + 5.897 \times 10^{-5}T^2 - 5.657 \times 10^{-8}T^3$
90 wt%	$4.377 - 3.776 \times 10^{-2}T + 1.090 \times 10^{-4}T^2 - 1.050 \times 10^{-7}T^3$

In addition, the thermal conductivity and specific heat for the gas and liquid phases are estimated by the mixing law based on the species in each phase. The mass diffusivity of the gas and liquid phases are calculated by the kinetic theory [129].

6.2.4 Interfacial area model

The wet ratio of the wire mesh is assumed to be equal to the fraction of the effective interfacial area to the total area of the dry packing, and it is expressed as follows:

$$f_e = \frac{A_{GL}}{a_S} = \frac{A_e}{a_S} \tag{6-1}$$

where A_e is the effective interfacial area as expressed in Equation (5-12), which is obtained from the numerical regression based on the results of the mesoscale 3D VOF simulations. The contact angle is set as $\gamma = 18°$, which means that the MEA solution easily spreads and contacts on the packing surface in the state of rotation. In addition, on considering the increment of the interfacial area from the side wall next to the packing, the interfacial area in the region that is close to the side wall is calculated as follows:

$$A_{GL,w} = \left(A_w f_e + a_S f_e V_{cell,w}\right) = f_e\left(\frac{1}{\Delta x_w} + a_S\right) V_{cell,w} \tag{6-2}$$

where the wet ratio of the wall is assumed to be the same as that in the packing region; A_w is the surface area of the wall in the cell next to the side wall, $V_{cell,w}$ is the volume of the cell next to the side wall, and Δx_w is the axial distance of the cell next to the wall.

6.2.5 Numerical scheme and solution procedures

For reducing the truncation errors, simulations are performed using the ANSYS® Fluent 17.2 software in a double precision mode, and it incorporates the in-house developed UDFs for setting the porous media model, drag force model, interfacial area model, mass transfer model and other self-defined functions, such as the properties of the gas and liquid. Further, the pressure-based solver and the relative velocity formulation are employed. The pressure-velocity coupling is resolved by the Coupled scheme, and the PRESTO! scheme is employed for the pressure discretization [129]. The gradient of the variables is calculated through using the least-squares cell based method. The QUICK scheme is applied for the spatial discretization of the volume fraction equation, the second-order upwind scheme is employed for solving the momentum equations, energy equations and species transport equations. Finally, the simulations are performed in two steps. First, the equations are solved without interfacial mass transfer. The gas and liquid velocities are gradually increased until the target velocities, and the pseudo transient method is employed to accelerate convergence. When the simulation reaches to a steady state, the interfacial mass transfer calculation begins to be performed by activing the mass transfer equation. All the equations with residuals less than 1×10^{-3} are considered as the convergence criterion. In addition, the CO_2 concentration at the gas outlet are monitored to ensure the simulation achieves the steady state.

6.3 Results and discussion

6.3.1 Effect of the rotational speed

6.3.1.1 Effect of the rotational speed on $K_G a$

The rotational speed, which is closely related to the power consumption, is a very important operating parameter of RPBs. Figure 6-5 (a) and (b) show the effect of the rotational speed, varying from 300 rpm to 1150 rpm, on the overall gas phase mass transfer coefficient $K_G a$ (defined by Eq. (2-2)) of the packing region of the RPB. In these investigations, the gas flow rate is fixed at 9.8 L/s, and the absorption solutions are 30 wt% and 90 wt% MEA solutions, which are the normal concentration as used in the traditional packed columns and the high concentration for RPBs, respectively. For each MEA solution, three different liquid flow rates have been used to make the MEA to CO_2 molar ratio at 3.3, 4.0 and 4.4. In order to achieve this, for the 30 wt% MEA (see Figure 6-5 (a)), the liquid to gas mass flow ratios are 2.8, 3.3 and 3.7, and for the 90 wt% MEA (see Figure 6-5 (b)), the liquid to gas mass flow ratios are 0.9, 1.0 and 1.2.

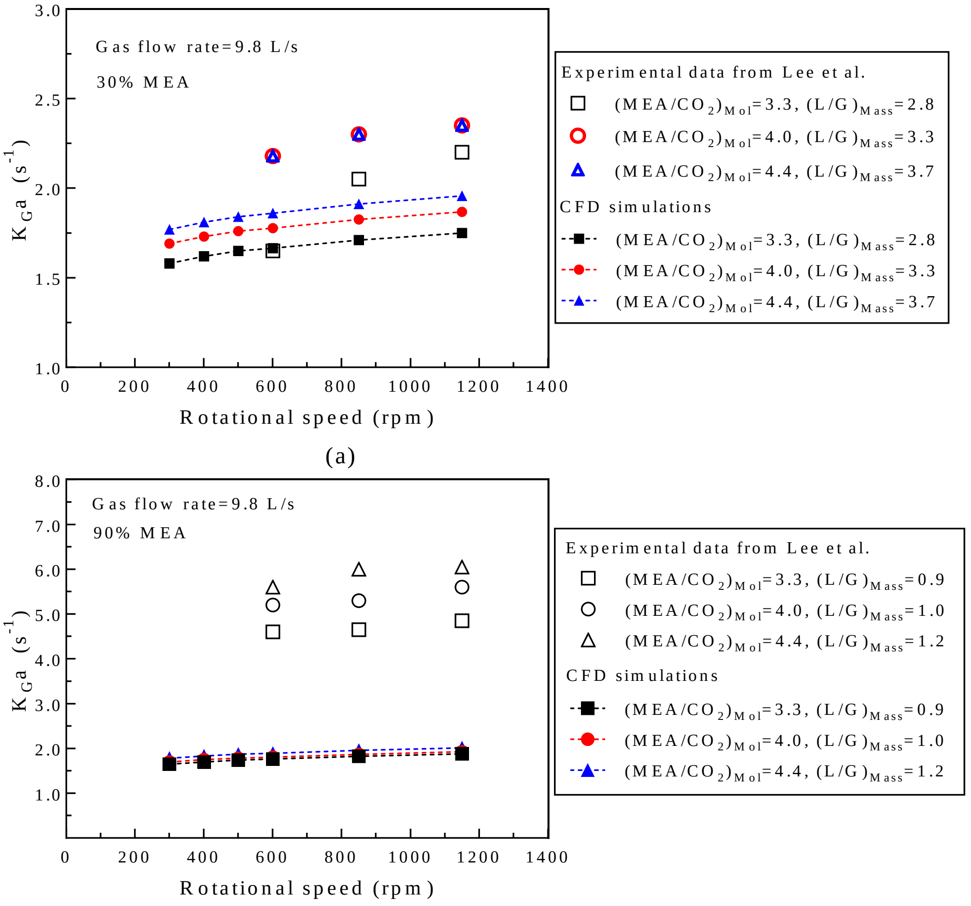

(a)

(b)

Figure 6-5 Effect of the rotational speed on the overall gas phase mass transfer coefficient K_Ga: (a) 30% MEA and (b) 90% MEA.

As can be seen from Figure 6-5 (a) and (b), a higher MEA to CO_2 molar ratio, as well as a higher liquid to gas mass flow rate ratio, results of a higher K_Ga. In addition, with the increasing of the rotational speed, the K_Ga increases slowly. For example, when the rotational speed increases from 300 rpm to 1200 rpm, the K_Ga only increases about 10% for each liquid flow rate condition. This means that the rotational speed has a weak effect on changing the K_Ga within the large range of speed variations studied. This is mainly because the effective interfacial area in the packing region of the RPB only slightly increases with the increasing of the rotational speed, and this has been discussed in detail in Section 5.4.2.2.

In order to validate the CFD model, the simulation results are compared with the experimental data from Lee et al. [31]. However, in their experiments [31], the $K_G a$ was calculated using Eq. (2-2) based on the CO_2 concentrations at the gas outlet pipe and gas inlet pipe of the RPB, and this means that the $K_G a$ is the parameter that reflects the CO_2 absorption in the whole RPB rather than only in the packing region of the RPB. Due to the CO_2 absorption occurring in the cavity region and the central region of the RPB has not been considered in the CFD model, the simulated results for the $K_G a$ are lower that the experimental data, especially in the 90% MEA case, as shown in Figure 6-5 (b). This is probably because the higher MEA concentration results in a longer contact time between the MEA and the CO_2, especially when the MEA solution attaches onto the case wall after it has been thrown away from the packing, which promotes the CO_2 absorption in the cavity region. In addition, when comparing the experimental data between Figure 6-5 (a) and (b), it can be seen, for the same MEA to CO_2 molar ratio, when using 90% MEA the $K_G a$ of the RPB is much higher than the $K_G a$ in the 30% MEA cases. The reason for this phenomenon was not clearly explained by Lee et al. [31]. While, in the CFD simulation, the $K_G a$ is very similar for the same MEA to CO_2 molar ratio, no matter what is the MEA concentration. Therefore, the increased $K_G a$ when using the 90wt% MEA is very possibly due to the CO_2 absorption in the cavity region of the RPB being higher than the 30wt% MEA solution. The variation trend and the slope of the $K_G a$ in the two cases are the same as in the experiments, and for the 30% MEA, the values of the simulated $K_G a$ is close to the experimental data. Therefore, the CFD model can be regarded to effectively predict and analyse the CO_2 absorption in the packing region of the RPB at different operating conditions. Further, it is worth mentioning that more attention should be paid to the central region and the cavity region of the RPB in future investigations.

6.3.1.2 Effect of the rotational speed on the pressure drop

The operating conditions, which have been used for the $K_G a$ investigations in Section 6.3.1.1, are adopted to investigate the pressure drop in the RPB. As shown in Figure 6-6 (a) and (b), the pressure drop is not sensitive to the change in the liquid flow rate (LFR) at different rotational speeds for the specified gas flow rate. This is because the liquid holdups at all the investigated operating conditions are very small, and they are far from making the RPB be in a flooding state, and therefore they have very weak effects on the gas pressure drop. Further, the effect of the rotational speed on the pressure drop can be clearly observed in Figure 6-6 (a) and (b). With the rotational speed increasing from 300 rpm to 1150 rpm, the pressure drop increases from about 160 Pa to about 310 Pa, which is mainly induced by the enhanced centrifugal field in the packing region of the RPB and the increased drag force between the gas and liquid.

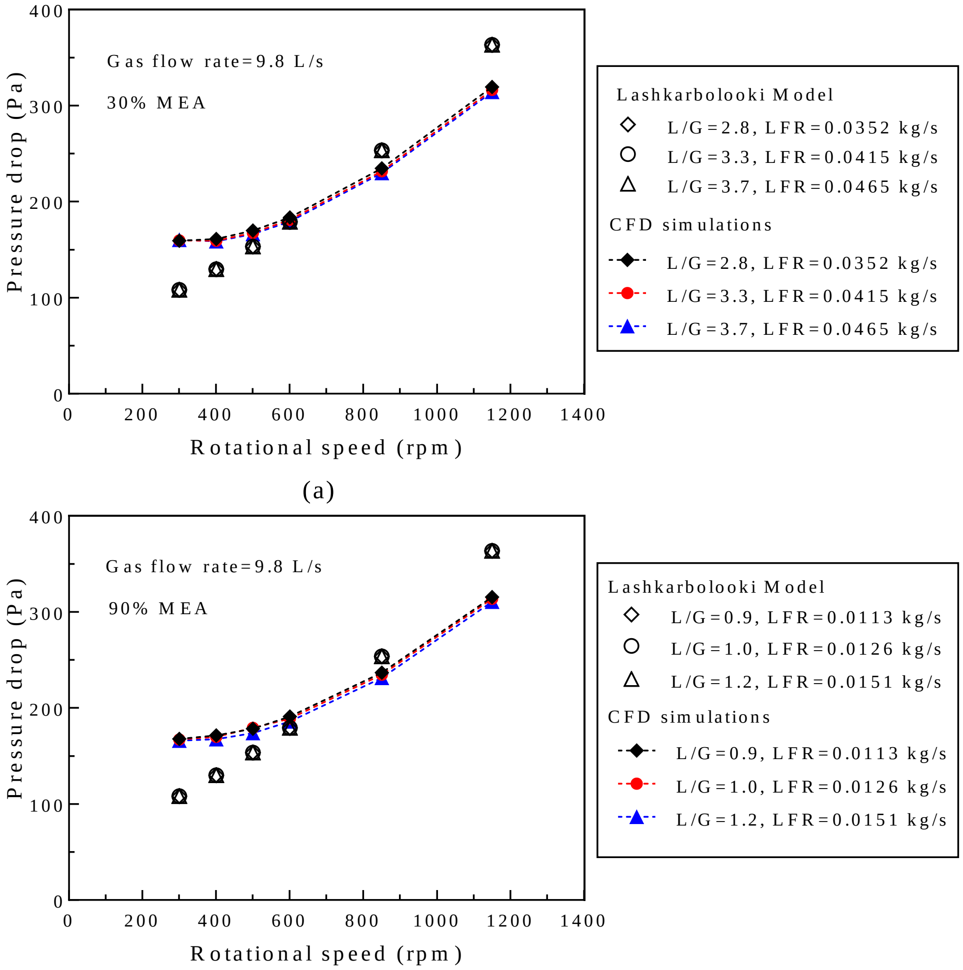

(a)

(b)

Figure 6-6 Effect of the rotational speed on the pressure drop: (a) 30% MEA and (b) 90% MEA.

Due to the lack of experimental data on the pressure drop in the investigated RPB, the simulation results are compared with the semi-empirical correlation [173]. The correlation that was proposed by Lashkarbolooki [173] for predicting the pressure drop across RPBs, was based on a theoretical analysis, and the pressure drop across the packing was considered as a sum of (i) the drag force pressure drop, which constitutes a viscous energy loss and an inertial loss, (ii) the pressure drop due to the centrifugal force and (iii) the gas-packing and the gas-liquid slip pressure drop. The coefficients in the empirical correlation were regressed based on three different RPB designs [73, 74, 174]. Therefore, the Lashkarbolooki model can be considered as a general model for predicting the pressure in RPBs. As shown in Figure 6-6 (a) and (b), the CFD simulation results are in a reasonable agreement with the results predicted by the Lashkarbolooki model. Therefore, we can conclude that the CFD model is effective for predicting the pressure drop in the RPB. The small deviation between the CFD predictions and the correlation is probably due to (i) the different dimensions and the different packing materials between the simulated RPB and the RPBs that were used for generating the empirical correlation; (ii) the pressure drop in the cavity region and central region of the RPB are not considered in the CFD model. It is worth mentioning that a 3D Eulerian CFD model, including all the regions of the RPB, has the potential to provide a more accurate prediction of the overall pressure in the RPB in the future.

6.3.2 Effect of the gas flow rate

As shown in Figure 6-7 (a)-(c), the RPB at two rotational speeds, 600 rpm and 800 rpm, has been employed to investigate the effect of the gas flow rate on $K_G a$, CO_2 removal efficiency, and pressure drop. In the investigation, the high-concentrated solution, 90 wt% MEA, which has the potential to be extensively employed in RPBs for CO_2 capture, is used as the absorbent. The liquid flow rate is fixed at 0.038 kg/s, and the gas flow rate varies from 4.9 L/s to 19.6 L/s, which results in the L/G mass flow rate ratio varying from 6.0 to 1.5, and these values are all within reasonable operating conditions. As can be seen from Figure 6-7 (a), a higher rotational speed results in a slightly higher $K_G a$ at all the gas flow rate conditions, and this is consistent with the conclusion in Section 6.3.1. In addition, the $K_G a$ slightly increases with the increasing of the gas flow rate is mainly due to the increased mass transfer coefficient in the gas side according to Eq. (3-42). However, as shown in Figure 6-7 (b), with the increasing of the gas flow rate, the CO_2 removal efficiency (defined in Eq. (2-3) decreases from about 0.5 to about 0.17. This is mainly due to the much reduced gas-liquid contact time that prevents the CO_2 from being fully absorbed by the MEA solutions, which can be clearly observed from Figure 6-8, where the distributions of the mole fraction of CO_2 in the gas phase at different gas flow rates are presented. In addition, as shown in Figure 6-7 (c), the pressure drop increases from about 100 Pa to 400 Pa with the increasing gas flow rate from 4.9 L/s to 19.6 L/s. Therefore, a comprehensive evaluation, including $K_G a$, CO_2 removal efficiency and pressure drop, should be performed in order to decide a suitable gas flow rate for achieving an optimized result.

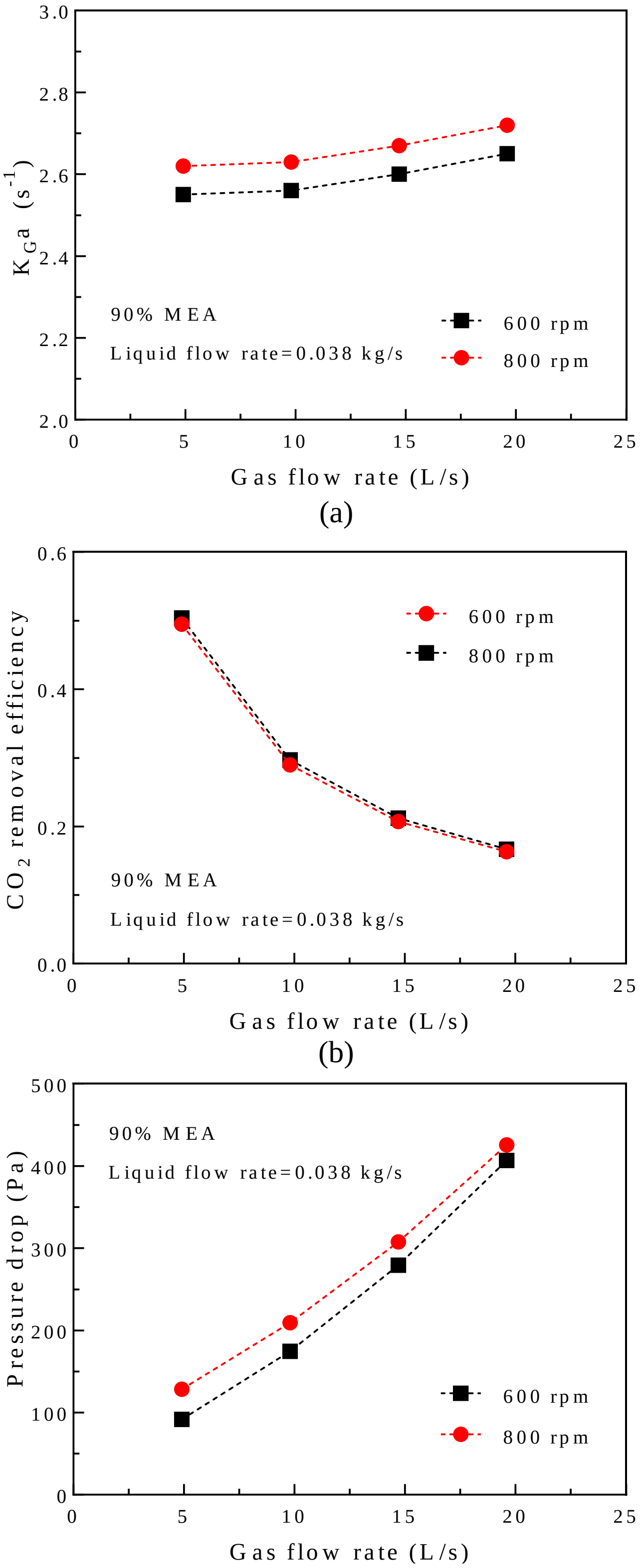

(a)

(b)

(c)

Figure 6-7 Effect of the gas flow rate on (a) the overall gas phase mass transfer coefficient K_Ga, (b) the CO_2 removal efficiency and (c) the pressure drop.

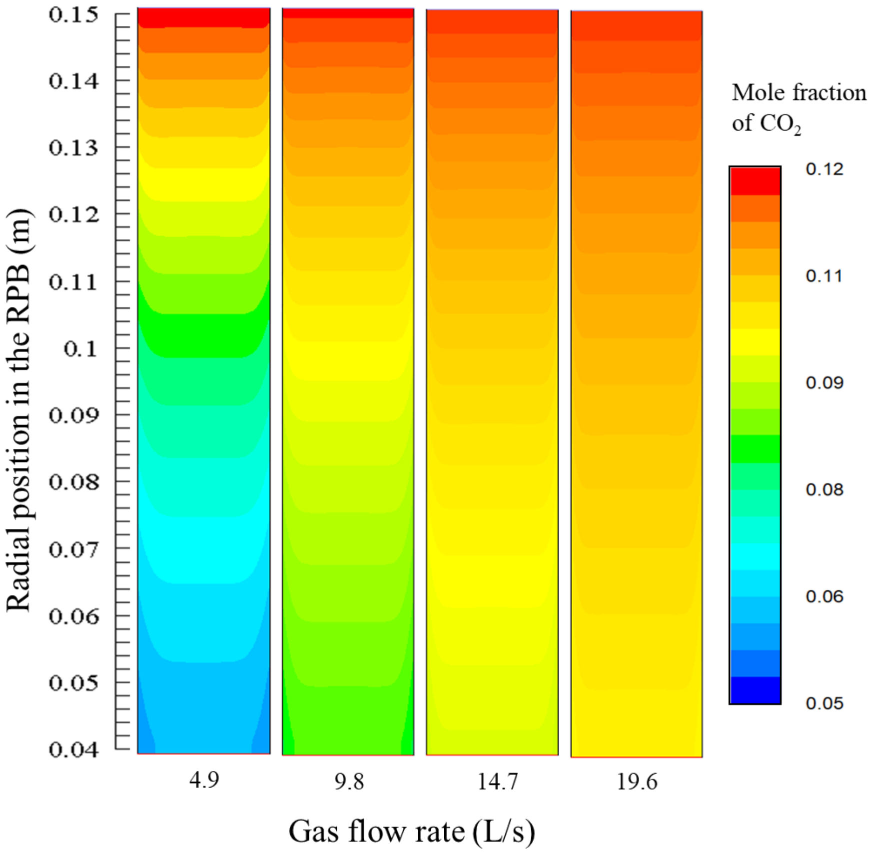

Figure 6-8 Distributions of the mole fraction of CO_2 in the gas phase in the RPB at different gas flow rates (90 wt% MEA, 600rpm, *LFR*=0.038 kg/s).

6.3.3 Effect of the liquid flow rate

The effect of the liquid flow rate on CO_2 absorption and pressure drop has been investigated using the Eulerian CFD model. In this investigation, the typical operating condition is set, where the gas flow rate is 9.8 L/s and the rotational speed is 600 rpm. Distributions of the axial-averaged CO_2 mole fraction in the gas phase along the radial direction of the RPB are shown in Figure 6-9. It can be seen that the CO_2 concentration is the same at the gas inlet, while it decreases gradually with the increasing of the liquid flow rate at the gas outlet. This is mainly due to the increased liquid flow rate increasing the effective interfacial area as has been discussed in Section 5.4.2.3, which enhances the CO_2 absorption in the RPB. In addition, the K_Ga has been calculated and presented in Figure 6-10 (a). It can be seen that with the increasing of the liquid flow rate from 0.011 to 0.050 kg/s, which means the L/G mass flow rate ratio changes from 0.9 to 4.0, the K_Ga increases from 1.76 to 2.85 s^{-1}.

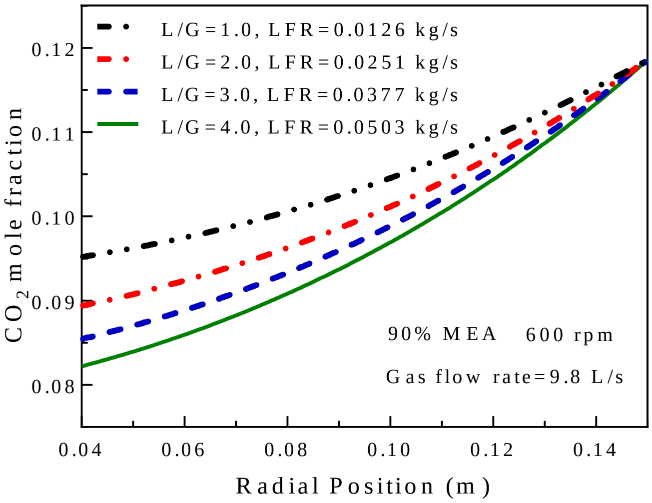

Figure 6-9 Effect of the liquid flow rate as well as the L/G ratio on the CO_2 mole fraction distribution in the gas phase alone the radial direction in the RPB.

The effect of the liquid flow rate on the pressure drop is shown in Figure 6-10 (b), where the pressure drop decreases slightly with the increasing of the liquid flow rate. This is mainly due to (i) more CO_2 being absorbed by the liquid with a higher liquid flow rate, which results in a lower average gas flow rate in the RPB; (ii) the drag force between the gas and liquid being lower than the drag force between the gas and packings, which results in a slightly lower resistance force for the gas phase with an increasing wetted area of the packings when increasing the liquid flow rate.

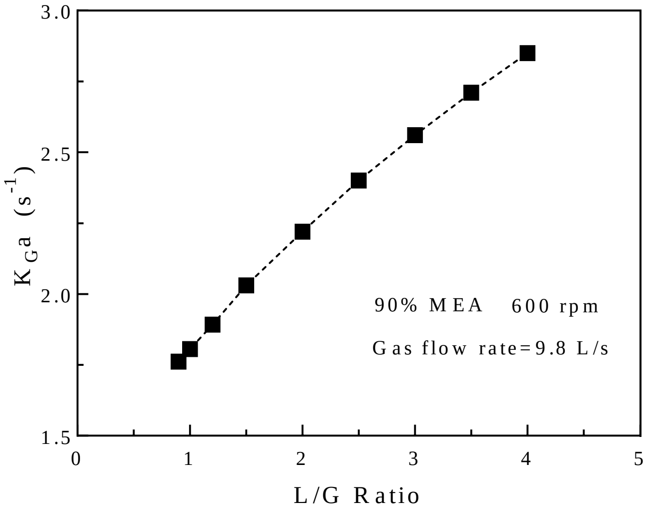

(a)

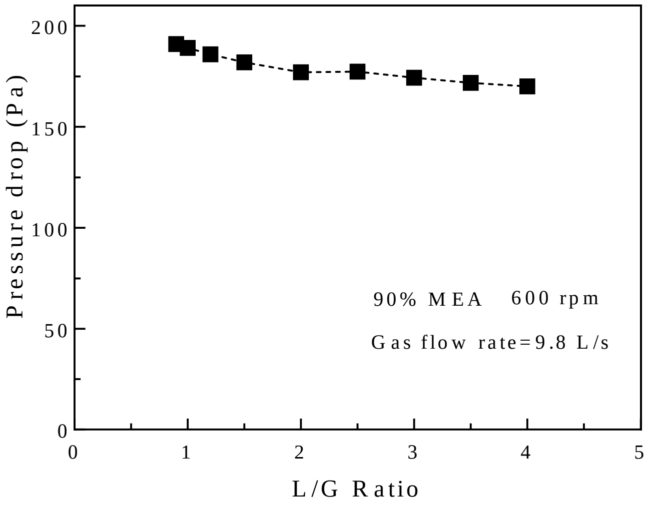

(b)

Figure 6-10 Effect of the liquid flow rate as well as the L/G ratio on (a) the overall gas phase mass transfer coefficient K_Ga and (b) the pressure drop.

6.3.4 Effect of the MEA concentration

One of the advantages of an RPB is its ability to deal with MEA solutions with high concentrations. Therefore, the effect of the MEA concentration on K_Ga and the pressure drop is investigated through using CFD simulations. In the simulations, the typical conditions are adopted, where the rotational speed of the RPB is set at 600 rpm, the gas flow rate is 9.8 L/s and the L/G mass flow rate ratio is fixed at 3.3. As shown in Figure

6-11 (a), the $K_G a$ almost increases linearly from 1.78 to 3.57 with the MEA concentration increasing from 30 wt% to 90 wt%. This is mainly because (i) the increased MEA concentration leads to a higher liquid viscosity, which increases both the liquid holdup and the effective interfacial area, (ii) a higher MEA concentration accelerates the chemical reaction between the MEA and the dissolved CO_2 in the liquid phase according to Eq. (3-56), which promotes the CO_2 diffusion from the gas side to the liquid side. In addition, as shown in Figure 6-11 (b), the pressure drop decreases slightly with the increasing of the MEA concentration, which is due to the wetted area of the packings increasing and the averaged gas flow rate slightly decreasing.

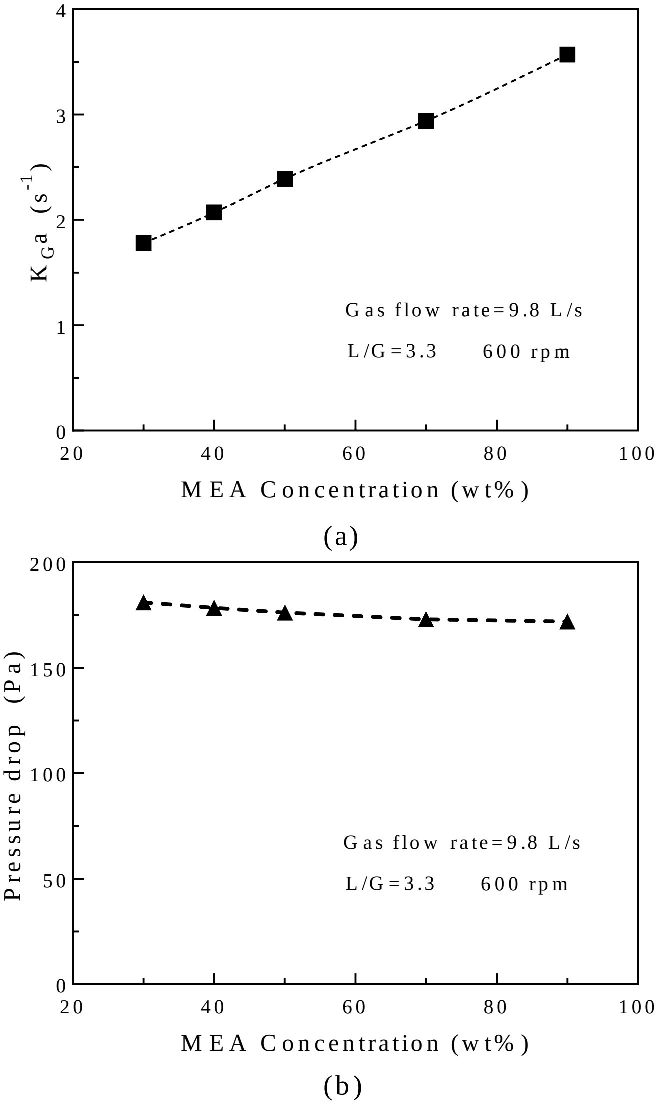

Figure 6-11 Effect of the MEA concentration on (a) the overall gas phase mass transfer coefficient K_Ga and (b) the pressure drop.

6.3.5 Effect of the liquid inlet temperature

The chemical reaction between CO_2 and MEA is influenced by the reaction temperature, and the temperature of the absorption liquid can be easily adjusted in the actual CO_2 absorption system. Therefore, the effect of the liquid inlet temperature from 30 to 70 ℃ on the CO_2 absorption is investigated in this section through using the Eulerian CFD model. In the simulation, the gas inlet temperature is fixed at 40 ℃, which is close to the temperature of the actual flue gas before connecting to the CO_2 absorption equipment. Typically 30 wt% MEA is used as the absorbent, the gas flow rate is fixed at 9.8 L/s, the L/G ratio is fix at 3.3, and the rotational speed is set as 600 rpm. For a better understanding of the temperature profile in the RPB, the axial-averaged liquid temperatures along the radial direction of the RPB at different liquid inlet temperatures are shown in Figure 6-12. It can be seen that all the temperatures have upward trends from the inner boundary (liquid inlet) to the outer boundary (liquid outlet) of the RPB, and this is due to the accumulation of the reaction heat in the liquid phase. For the relative high liquid inlet temperatures, such as 60 °C and 70 °C, there is a slight temperature decrease close to the outer boundary of the RPB, which is cooled down by the injected low temperature flue gas (40 °C). In addition, the K_Ga and the CO_2 removal efficiency with the increasing of the liquid inlet temperature are illustrated in Figure 6-13 (a) and (b), respectively. It can be seen that the K_Ga increases from 1.45 to 3.33, and the CO_2 removal efficiency increases from 0.18 to 0.36 with the liquid inlet temperature increasing from 30 °C to 70 °C. This is due to the chemical reaction rate between the MEA and CO_2 being increased with the increasing reaction temperature (ref. Eq. (3-58), and this promotes the mass transfer of the CO_2 from the liquid phase to the gas phase.

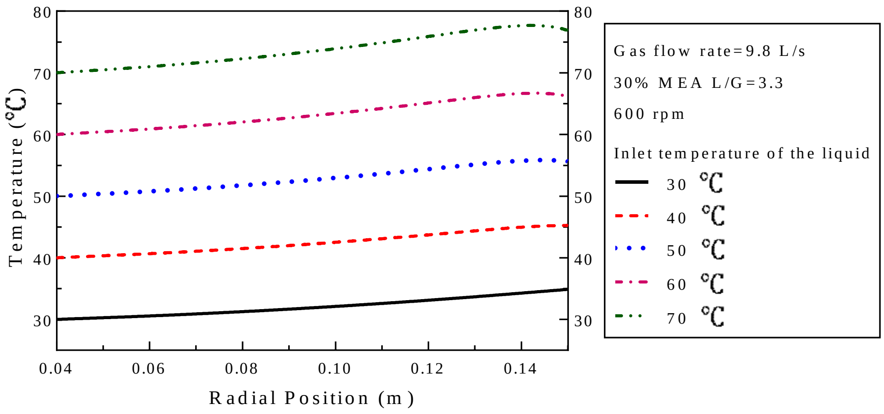

Figure 6-12 Axial-averaged liquid temperature along the radial direction of the RPB at different liquid inlet temperatures.

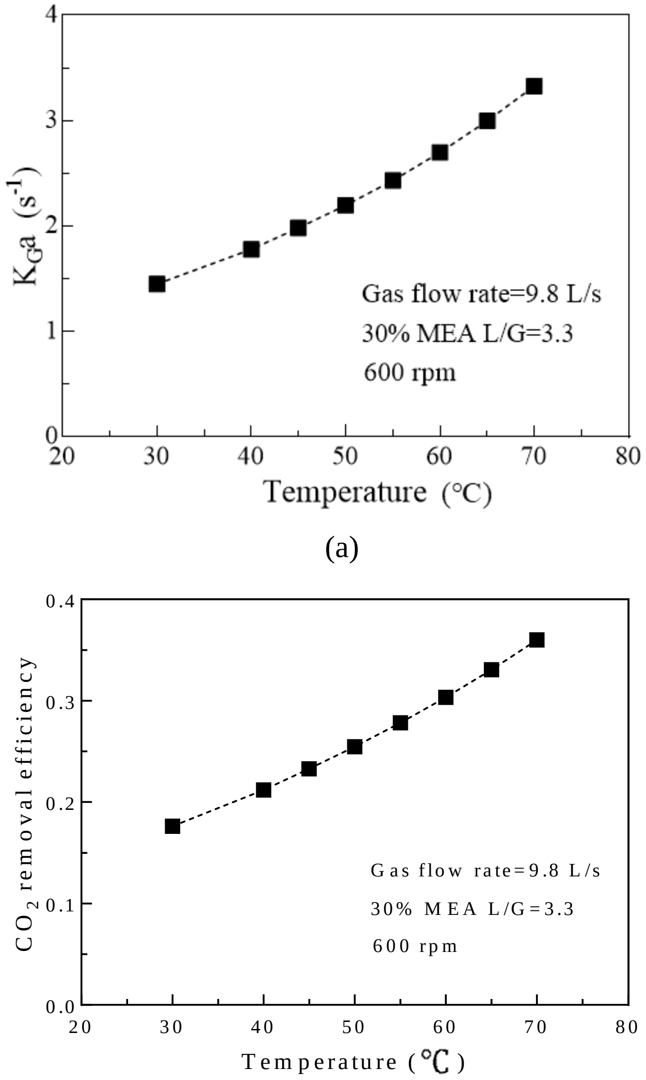

(a)

(b)

Figure 6-13 Effect of the liquid inlet temperature on (a) the overall gas phase mass transfer coefficient K_Ga and (b) the CO_2 removal efficiency.

6.4 Conclusions

In this chapter, an Eulerian CFD model, that incorporates the VOF-based gas-liquid interfacial area correlation, successfully simulates the CO_2 absorption by MEA solutions in the packing region of an RPB. The model has been validated through comparing the predicted K_Ga with the experimental data of Lee et al. [31], and comparing the predicted pressure drop with the semi-empirical correlation [173]. Further, the effects of the operating parameters on the $K_G a$, the CO_2 removal efficiency and/or the pressure drop are analysed. The results show that increasing the liquid flow rate, MEA concentration, and the liquid inlet temperature has a significant positive impact on $K_G a$ and no significant effect on the pressure drop. Therefore, these parameters can be used to adjust the CO_2 absorption efficiency in the RPB according to the actual condition without having too much influence on the pressure drop induced energy dissipation. While, with the increasing of the rotational speed and the gas flow rate, the $K_G a$ increases slightly but the pressure drop augment is significant. Therefore, a moderate rotational speed and gas flow rate is better for increasing the overall efficiency of the RPB. In conclusion, this chapter demonstrates the feasibility of the proposed modelling method for effectively predicting the CO_2 absorption and pressure drop in RPBs. Further, this modelling method can be used to assist the scaling up and the operation optimization of large-scale RPBs for CO_2 capture.

Chapter 7: Conclusions and future work

Carbon Capture and Storage (CCS) technology is a potential technical solution for thermal power plants to achieve a low carbon energy supply. However, high capital investment of the CO_2 capture facilities and high energy consumption during the carbon capture process are the key obstacles to the development of CCS technologies. Process intensification through using RPBs is a potential for reducing the capital investment and energy consumption during CO_2 capture. CFD simulations are effective methods to investigate the hydrodynamics and mass transfer performance of the RPBs. This thesis has focused on investigating the very important hydrodynamic characteristics and CO_2 absorption performance of the RPBs through using CFD methods. The CFD modelling is realised though using the ANSYS® Fluent software with UDFs. The conclusions are summarised in Section 7.1 and the recommendations for future work are discussed in Section 7.2.

7.1 Conclusions

7.1.1 A 2D CFD model for analysing the liquid flow in an RPB

Due to the complex structure of the packing in RPBs, the characteristics of the liquid flow within RPBs are very difficult to be fully investigated by experimental methods. In order to achieve an effective prediction of the liquid flow characteristics in an RPB, a new 2D computational framework of an RPB has been proposed based on the VOF method presented in Chapter 4. This model adopts the real round cross-section of the wire mesh as the packing characteristics and a non-uniform grid generation strategy has been employed to make the model available to capture the liquid films on the packing surface so that both the formation of the liquid droplet and the formation of the liquid film can be simulated. The setting of the inlet boundary condition is achieved through writing UDFs.

The simulation results show good agreements with the experimental data, and this indicates that the 2D CFD model is effective in analysing the liquid flow characteristics in the RPB. Both the overall and local liquid flow patterns in the RPB have been analysed, and the distinct liquid flow patterns in different regions of the RPB have been clearly observed. New findings from the simulations are summarised as follows: (i) The radial depth of the entrance region is about 10 mm from the inner boundary of the packing, and the depth of the entrance region increases with increasing the liquid jet velocity. (ii) In the entrance region of the RPB, the liquid flow is a ligament-dominated flow. In the bulk region, the flow pattern is a pore-dominated flow at a relative weak centrifugal field (80-320 m/s^2) and a droplet-dominated flow at a relative strong centrifugal field (320-720 m/s^2). (iii) With the increasing of the rotational speed, the liquid holdup dramatically decreases and the degree of the liquid dispersion increases. Further, the increasing liquid jet velocity decreases the liquid residence time but slightly increases the liquid holdup. (iv) With the increasing of the concentration of MEA solution, the liquid holdup increases and the degree of the liquid dispersion decreases, but the effects are weaker at a higher rotational speed. (v) The liquid holdup and flow pattern are sensitive to the contact angle. Larger contact angles can generate more liquid droplets while smaller contact angles can generate more liquid films. With the increasing of the contact angle, the liquid holdup is reduced.

In summary, the 2D VOF model can be used to analyse the liquid flow patterns, liquid holdup, liquid residence time as well as the degree of liquid dispersion in an RPB using a relatively small number of grids compared to a 3D model.

7.1.2 A 3D mesoscale CFD model for analysing the detailed liquid flow in an RPB

For obtaining the detailed and more accurate information of the liquid flow in RPBs, it is necessary to simulate the flow in the real geometrical structure of the packings. However, it is very difficult to perform a full 3D simulation of an RPB with appropriate accuracy due to the complexed and small-scale structure of the packing. Therefore, a mesoscale 3D CFD model has been proposed to simulate the liquid flow in the real packings of the RPB for CO_2 capture in Chapter 5. The mesoscale model is based on a small 3D REU with appropriate boundary conditions, being implemented at different locations in an RPB, so that the overall characteristics of the liquid flow in the RPB can be obtained. The model has been validated through comparing the simulation results with experimental data. Detailed liquid flow patterns, liquid holdup, volume fraction of the droplets, effective interfacial area, wetted wall area and specific surface area of the liquid in the RPB have been obtained numerically. The acquisition of the detailed parameters in the calculation domain is achieved through writing UDFs. The results show that the mesoscale CFD model is effective in analysing the local detailed liquid flow characteristics as well as the overall parameters of an RPB. The best fit correlations for predicting the liquid holdup ε_L, effective interfacial area A_e, and specific surface area A_s in the RPB based on the CFD simulations are as follows:

For the liquid holdup:

$$\varepsilon_L = 0.0188\left(\frac{g_\omega}{g_0}\right)^{-0.4764}\left(\frac{U}{U_0}\right)^{0.5716}\left(\frac{\nu}{\nu_0}\right)^{0.3197}\left(\frac{\gamma}{\Upsilon_0}\right)^{-0.7557}$$

For the effective interfacial area:

$$A_e = 202.3485\left(\frac{g_\omega}{g_0}\right)^{0.0435}\left(\frac{U}{U_0}\right)^{0.4275}\left(\frac{\nu}{\nu_0}\right)^{0.1200}\left(\frac{\gamma}{\Upsilon_0}\right)^{-0.5856}$$

For the specific surface area of the liquid:

$$A_s = 10517.1970\left(\frac{g_\omega}{g_0}\right)^{0.4946}\left(\frac{U}{U_0}\right)^{-0.1515}\left(\frac{\nu}{\nu_0}\right)^{-0.2921}\left(\frac{\gamma}{\Upsilon_0}\right)^{0.1658}$$

In general, the proposed model provides a feasible way to predict the detailed hydrodynamic performance of the RPB using much fewer grid numbers compared to a full 3D simulation, which could assist in the optimizing of the design and operation of the large-scale RPBs for CO_2 capture.

7.1.3 An Eulerian CFD model for analysing the CO_2 absorption in an RPB

The mass transfer performance and pressure drop are the most important characteristics of RPBs for influencing the CO_2 capture efficiency and the energy dissipation. Therefore, in Chapter 6, an Eulerian computational framework is developed through combining the multiphase porous media model, interfacial area model, and reactive mass transfer model, etc. to analyse the mass transfer and pressure drop in a CO_2 absorption process in an RPB. The specified submodels for RPBs are implemented in ANSYS® Fluent through writing UDFs. The model is validated through comparing the simulation results with experimental data and existing correlations. The results show that increasing the liquid flow rate, MEA concentration, and the liquid inlet temperature have a significant positive impact on $K_G a$ and no significant effect on the pressure drop.

While, with the increasing of the rotational speed and the gas flow rate, the K_Ga increases slightly but the pressure drop augment significantly. Therefore, the liquid flow rate, the MEA concentration, and the liquid inlet temperature can be appropriately increased to promote the CO_2 absorption in the RPB without having too much influence on the energy dissipation due to the pressure drop. In addition, a moderate rotational speed and gas flow rate is better for increasing the overall efficiency of the RPB both by considering the K_Ga and the pressure drop. In summary, the proposed Eulerian model is feasible for effectively predicting the CO_2 absorption and pressure drop in RPBs. Further, this modelling method can be used to assist the scaling up and the operation optimization of large-scale RPBs for CO_2 capture.

7.2 Recommendations for future work

In this thesis, some progress has been made in the CFD simulations of RPBs for CO_2 capture. However, there are still many aspects that require further investigation in order to further improve the simulation accuracy and efficiency, and deepen the understanding of the mechanism of the RPB for CO_2 capture. Therefore, some recommendations for future work are listed as follows:

7.2.1 Improvement of the VOF modelling method

(i) The liquid behaviour in the RPB is very sensitive to the wettability of the packing surface, which is usually specified by the contact angle. Currently, due to lack of detailed experimental data on the dynamic contact angle for stainless steel packings with different concentrated MEA solutions, the static contact angle is specified in the VOF simulation. In order to achieve a more accurate prediction of the liquid flow on the packing surface, a dynamic contact angle model for stainless steel with MEA solutions is suggested to be employed in the VOF simulation. In addition, in order to achieve an accurate tracking of the gas-liquid interfaces and the gas-liquid-solid contact lines, very small computational grids are required in these regions, and therefore a dynamic local grid refinement technology is suggested to be employed for reducing the total number of the grids. Further, detailed measurements of the dynamic contact angle between the packing and solutions are also suggested.

(ii) At present, the local hydrodynamic characteristics of the gas-liquid flow in an RPB has been investigated by using the mesoscale 3D VOF model. The local mass transfer characteristics in an RPB is highly dependent on the local gas-liquid flow, but this has not been investigated in detail. Therefore, a direct numerical simulation of the inter-phase mass transfer by using the VOF-based method is suggested, and this can provide the detailed information of the local mass transfer rates. This local information can be used to develop accurate mass transfer models that may be integrated into large-scale Eulerian simulations or process simulations and used for RPB design and optimization.

7.2.2 Improvement of the Eulerian modelling method

(i) Currently, the CO_2 absorption in the RPB is investigated by using a simplified 2D axisymmetric swirl model based on the assumption that the flow is uniform in the circumference direction. The gas-liquid flow and mass transfer in the central cavity region and the outer annular cavity region are not considered. In order to achieve a more accurate simulation, a full 3D Eulerian mass transfer simulation of the RPB with the consideration of the effect of the gas inlet and the liquid distributor is suggested. In the 3D Eulerian model, the effect of the packings can be simulated through using a porous media model. Also, the 3D Eulerian model can be better used to optimize the overall structure of the RPB for improving the mass transfer performance and decrease the overall pressure drop.

(ii) For the Eulerian modelling method, submodels are crucial for modelling the hydrodynamics and mass transfer of RPBs. The development of new submodels with higher accuracy and wider applicability are very important for improving the accuracy and the scope of application of the Eulerian model for modelling RPBs. Therefore, it is suggested to develop new porous media models, new gas-liquid drag models, and new interfacial area models for RPBs with different types of packings and different flow configurations. In addition, developing new mass transfer models, new heat transfer models, and new chemical reaction models that are suitable for RPBs with different solvents are encouraged.

7.2.3 Development of new RPB simulation and experimental methods

(i) CFD simulations are effective in modelling the details of the CO_2 absorption in RPBs, which can produce accurate results of the pressure drop, absorption efficiency, etc. Therefore, it can be used to optimise the structure and operational conditions of the RPB absorbers. However, CFD is incapable of efficiently modelling all components of a complex CO_2 capture system. In order to take advantage of the accuracy of the CFD simulation and the efficiency of the process modelling, it is suggested to build a CFD-process co-simulation model to simulate the whole CO_2 capture system. The CFD simulation results should be connected to the process model through using a suitable method, such as a reduced order model. In this way, optimization of the RPB and the system can be achieved from evaluating the overall efficiency of the CO_2 capture system.

(ii) CO_2 desorption from the amine-based solutions using RPBs has great potentials to reduce the volume of the regenerator in a post-combustion CO_2 capture process. Therefore, the development of CFD models for simulating the gas-liquid flow, heat and mass transfer of the CO_2 desorption in RPBs is suggested. Due to the solution in the RPB regenerator continues to undergo a phase change during the CO_2 desorption process, special considerations should be given to the phase change heat transfer and pressure variation.

(iii) CFD models require reliable experimental validations, however, detailed experimental data, such as liquid flow patterns, liquid holdup distributions, pressure distributions and CO_2 concentration distributions in RPBs, are rare. Therefore, developing advanced measurement technologies for obtaining the detailed information in RPBs is highly suggested, and this can promote the development of highly reliable CFD models.

Appendix

Lists of all conducted simulations with boundary/operating conditions in Chapter 5.

Table A-1 CFD simulation results with boundary/operating conditions (training data)*

No.	**Liquid**	R	N	LFR	g_ω	U	v	γ	ε_L	A_e	A_s	A_w
		m	*rpm*	m^3/h	m/s^2	*m/s*	mm^2/s	*deg*		m^{-1}	m^{-1}	m^{-1}
1	50% MEA	0.3	100	7.2	32.90	0.0053	3.35	75	0.0303	148	4874	70
2	50% MEA	0.3	150	7.2	74.02	0.0053	3.35	75	0.0211	152	7211	68
3	50% MEA	0.3	200	7.2	131.59	0.0053	3.35	75	0.0161	136	8461	54
4	50% MEA	0.3	300	7.2	296.09	0.0053	3.35	75	0.0118	158	13394	42
5	50% MEA	0.3	100	14.4	32.90	0.0106	3.35	75	0.0503	191	3794	95
6	50% MEA	0.3	150	14.4	74.02	0.0106	3.35	75	0.0324	206	6379	92
7	50% MEA	0.3	200	14.4	131.59	0.0106	3.35	75	0.0239	182	7629	74
8	50% MEA	0.3	300	14.4	296.09	0.0106	3.35	75	0.0177	209	11785	69
9	50% MEA	0.3	150	10.8	74.02	0.0080	3.35	75	0.0279	181	6494	80
10	50% MEA	0.3	150	18	74.02	0.0133	3.35	75	0.0395	229	5790	94
11	50% MEA	0.3	150	21.6	74.02	0.0159	3.35	75	0.0444	236	5306	107
12	50% MEA	0.3	250	7.2	205.62	0.0053	3.35	75	0.0125	146	11693	47

13	50% MEA	0.3	250	10.8	205.62	0.0080	3.35	75	0.0160	182	11391	58
14	50% MEA	0.3	250	18	205.62	0.0133	3.35	75	0.0229	229	10008	73
15	50% MEA	0.3	250	21.6	205.62	0.0159	3.35	75	0.0250	252	10066	79
16	30% MEA	0.3	150	14.4	74.02	0.0106	1.66	75	0.0215	162	7527	65
17	70% MEA	0.3	150	14.4	74.02	0.0106	6.85	75	0.0360	191	5518	97
18	90% MEA	0.3	150	14.4	74.02	0.0106	10.12	75	0.0420	208	4965	113
19	30% MEA	0.3	250	14.4	205.62	0.0106	1.66	75	0.0152	195	12819	52
20	70% MEA	0.3	250	14.4	205.62	0.0106	6.85	75	0.0228	238	8106	90
21	90% MEA	0.3	250	14.4	205.62	0.0106	10.12	75	0.0276	241	6782	97
22	50% MEA	0.3	150	14.4	74.02	0.0106	3.35	30	0.0500	310	6200	350
23	50% MEA	0.3	150	14.4	74.02	0.0106	3.35	60	0.0370	233	6306	129
24	50% MEA	0.3	150	14.4	74.02	0.0106	3.35	75	0.0324	206	6379	92
25	50% MEA	0.3	150	14.4	74.02	0.0106	3.35	90	0.0256	177	6899	55
26	50% MEA	0.3	150	14.4	74.02	0.0106	3.35	120	0.0180	127	7062	13
27	50% MEA	0.3	250	14.4	205.62	0.0106	3.35	30	0.0350	317	9050	347
28	50% MEA	0.3	250	14.4	205.62	0.0106	3.35	60	0.0240	245	10211	129
29	50% MEA	0.3	250	14.4	205.62	0.0106	3.35	75	0.0196	203	10367	70
30	50% MEA	0.3	250	14.4	205.62	0.0106	3.35	90	0.0137	179	13097	38
31	50% MEA	0.3	250	14.4	205.62	0.0106	3.35	120	0.0105	139	13198	16

Table A-2: CFD simulation results with boundary/operating conditions (test data)*

No.	**Liquid**	***R***	***N***	***LFR***	g_ω	***U***	***ν***	***γ***	ε_L	A_e	A_s	A_w
		m	*rpm*	m^3/h	m/s^2	*m/s*	mm^2/s	*deg*		m^{-1}	m^{-1}	m^{-1}
1	50% MEA	0.11	150	14.4	27.14	0.0289	3.35	75	0.0903	275	3048	133
2	50% MEA	0.38	150	14.4	93.76	0.0084	3.35	75	0.0229	167	7283	79
3	50% MEA	0.49	150	14.4	120.90	0.0065	3.35	75	0.0163	157	9661	66
4	50% MEA	0.11	250	14.4	75.39	0.0289	3.35	75	0.0464	233	5028	105
5	50% MEA	0.38	250	14.4	260.45	0.0084	3.35	75	0.0137	190	13799	68
6	50% MEA	0.49	250	14.4	335.84	0.0065	3.35	75	0.0107	159	14930	52
7	50% MEA	0.11	300	14.4	108.57	0.0289	3.35	75	0.0420	258	6144	113
8	50% MEA	0.3	300	14.4	296.09	0.0106	3.35	75	0.0177	209	11785	69
9	50% MEA	0.38	300	14.4	375.04	0.0084	3.35	75	0.0131	201	15326	58

*The simulations are based on an RPB with a bed of 0.1 m inner radius, 0.5 m outer radius and 0.2 m thickness. The specific surface area of the packing is 546.5 m^2/m^3 and the void fraction is 0.84.

List of references

[1] IPCC, *Climate Change 2014: Synthesis Report. Contribution of Working Groups I, II and III to the Fifth Assessment Report of the Intergovernmental Panel on Climate Change [Core Writing Team, R.K. Pachauri and L.A. Meyer (eds.)]*. 2014, IPCC: Geneva, Switzerland. pp. 151.

[2] NOAA/ESRL. *Trends in Atmospheric Carbon Dioxide*. 2018 [cited 2018 July 20]; Available from: http://www.esrl.noaa.gov/gmd/ccgg/trends/global.html.

[3] *International Energy Outlook 2017 (IEO2017)*. 2017, U.S. Energy Information Administration.

[4] Freund, P., *Making deep reductions in CO_2 emissions from coal-fired power plant using capture and storage CO_2*. Proceedings of the Institution of Mechanical Engineers Part a-Journal of Power and Energy, 2003. **217**(A1): pp. 1-7.

[5] Gibbins, J. and H. Chalmers, *Carbon capture and storage*. Energy Policy, 2008. **36**(12): pp. 4317-4322.

[6] Metz, B., O. Davidson, H. De Coninck, M. Loos, and L. Meyer, *IPCC, 2005: IPCC special report on carbon dioxide capture and storage. Prepared by Working Group III of the Intergovernmental Panel on Climate Change*. Cambridge, United Kingdom and New York, NY, USA, 2005. **442**.

[7] Hoffmann, B.S. and A. Szklo, *Integrated gasification combined cycle and carbon capture: A risky option to mitigate CO_2 emissions of coal-fired power plants*. Applied Energy, 2011. **88**(11): pp. 3917-3929.

[8] Yang, X., A. Clements, J. Szuhánszki, X. Huang, O. Farias Moguel, J. Li, J. Gibbins, Z. Liu, C. Zheng, D. Ingham, L. Ma, B. Nimmo, and M. Pourkashanian, *Prediction of the radiative heat transfer in small and large scale oxy-coal furnaces*. Applied Energy, 2018. **211**: pp. 523-537.

[9] Institute, T.G.C. *Large-scale CCS facilities*. 2018 [cited 2018 July 20]; Available from: https://www.globalccsinstitute.com/projects/large-scale-ccs-projects.

[10] Kvamsdal, H.M., J.P. Jakobsen, and K.A. Hoff, *Dynamic modeling and simulation of a CO_2 absorber column for post-combustion CO2 capture.* Chemical Engineering and Processing, 2009. **48**(1): pp. 135-144.

[11] Wang, M., A.S. Joel, C. Ramshaw, D. Eimer, and N.M. Musa, *Process intensification for post-combustion CO_2 capture with chemical absorption: A critical review.* Applied Energy, 2015. **158**: pp. 275-291.

[12] Biliyok, C., A. Lawal, M.H. Wang, and F. Seibert, *Dynamic modelling, validation and analysis of post-combustion chemical absorption CO_2 capture plant.* International Journal of Greenhouse Gas Control, 2012. **9**: pp. 428-445.

[13] Lawal, A., M.H. Wang, P. Stephenson, and O. Obi, *Demonstrating full-scale post-combustion CO_2 capture for coal-fired power plants through dynamic modelling and simulation.* Fuel, 2012. **101**: pp. 115-128.

[14] Wang, M., A. Lawal, P. Stephenson, J. Sidders, and C. Ramshaw, *Post-combustion CO_2 capture with chemical absorption: A state-of-the-art review.* Chemical Engineering Research & Design, 2011. **89**(9): pp. 1609-1624.

[15] Chambers, H.H.a.W., M. A, *Some factors affecting the design of centrifugal gas absorbers.* Trans. Inst. Chem. Eng.,, 1954. **32**: pp. S96-S91O97.

[16] Ramshaw, C. and R.H. Mallinson, *Mass transfer process, US Patent No. 4283255*. 1981.

[17] Cheng, H.H. and C.S. Tan, *Removal of CO_2 from indoor air by alkanolamine in a rotating packed bed.* Separation and Purification Technology, 2011. **82**: pp. 156-166.

[18] Yi, F., H.K. Zou, G.W. Chu, L. Shao, and J.F. Chen, *Modeling and experimental studies on absorption of CO_2 by Benfield solution in rotating packed bed.* Chemical Engineering Journal, 2009. **145**(3): pp. 377-384.

[19] Chen, Y.S. and H.S. Liu, *Absorption of VOCs in a rotating packed bed.* Industrial & Engineering Chemistry Research, 2002. **41**(6): pp. 1583-1588.

[20] Bai, S., G.W. Chu, S.C. Li, H.K. Zou, Y. Xiang, Y. Luo, and J.F. Chen, *SO_2 Removal in a Pilot Scale Rotating Packed Bed.* Environmental Engineering Science, 2015. **32**(9): pp. 806-815.

[21] Yuan, Z.G., W. Song, Y.Z. Liu, X.F. Kang, B. Peng, and T. Wang, *Regeneration of SO_2-Loaded Sodium Phosphate Solution in Rotating Packed Bed.* Journal of Chemical Engineering of Japan, 2014. **47**(10): pp. 777-781.

[22] Wu, H.G., M. Jin, F. Wang, G.X. Yu, and P. Lu, *Performance of Sodium Chlorite/Urea on Simultaneous Desulfurization and Denitrification in a Rotating Packed Bed.* Materials Science, Environment Protection and Applied Research, 2014. **908**: pp. 183-186.

[23] Jin, M., G.X. Yu, F. Wang, and P. Lu, *Simultaneous Absorption of SO_2 and NO using Sodium Chlorate/Urea Absorbent in a Rotating Packed Bed.* Materials Science, Environment Protection and Applied Research, 2014. **908**: pp. 187-190.

[24] Chu, G.W., Y. Luo, C.Y. Shan, H.K. Zou, Y. Xiang, L. Shao, and J.F. Chen, *Absorption of SO_2 with ammonia-based solution in a cocurrent rotating packed bed.* Industrial & Engineering Chemistry Research, 2014. **53**(40): pp. 15731-15737.

[25] Zhang, Y.H., Y.Z. Liu, and Z.B. Ouyang, *Pilot test study on desulfurization and dust removing of rotating packed bed.* Frontiers on Separation Science and Technology, 2004: pp. 873-878.

[26] Li, W.Y., W. Wu, H.K. Zou, G.W. Chu, L. Shao, and J.F. Chen, *A Mass Transfer Model for Devolatilization of Highly Viscous Media in Rotating Packed Bed.* Chinese Journal of Chemical Engineering, 2010. **18**(2): pp. 194-201.

[27] Chen, J.F., H. Gao, H.K. Zou, G.W. Chu, L. Zhang, L. Shao, Y. Xiang, and Y.X. Wu, *Cationic Polymerization in Rotating Packed Bed Reactor: Experimental and Modeling.* Aiche Journal, 2010. **56**(4): pp. 1053-1062.

[28] Ding., J.S., *A method to synthesis MDI*, C. Patent, Editor. 2007.

[29] Chen, J.F., Y.H. Wang, F. Guo, X.M. Wang, and C. Zheng, *Synthesis of nanoparticles with novel technology: High-gravity reactive precipitation.* Industrial & Engineering Chemistry Research, 2000. **39**(4): pp. 948-954.

[30] Jassim, M.S., G. Rochelle, D. Eimer, and C. Ramshaw, *Carbon dioxide absorption and desorption in aqueous monoethanolamine solutions in a rotating packed bed.* Industrial & Engineering Chemistry Research, 2007. **46**(9): pp. 2823-2833.

[31] Lee, J., T. Kolawole, and P. Attidekou, *Carbon Capture from a Simulated Flue Gas Using a Rotating Packed Bed Adsorber and Mono Ethanol Amine (MEA).* Energy Procedia, 2017. **114**(Supplement C): pp. 1834-1840.

[32] Yu, C.H., H.H. Cheng, and C.S. Tan, *CO_2 capture by alkanolamine solutions containing diethylenetriamine and piperazine in a rotating packed bed.* International Journal of Greenhouse Gas Control, 2012. **9**: pp. 136-147.

[33] Lin, C.C. and Y.W. Kuo, *Mass transfer performance of rotating packed beds with blade packings in absorption of CO2 into MEA solution.* International Journal of Heat and Mass Transfer, 2016. **97**: pp. 712-718.

[34] Chu, G.W., L. Sang, X.K. Du, Y. Luo, H.K. Zou, and J.F. Chen, *Studies of CO_2 absorption and effective interfacial area in a two-stage rotating packed bed with nickel foam packing.* Chemical Engineering and Processing, 2015. **90**: pp. 34-40.

[35] Zhao, B.T., W.W. Tao, M. Zhong, Y.X. Su, and G.M. Cui, *Process, performance and modeling of CO2 capture by chemical absorption using high gravity: A review.* Renewable & Sustainable Energy Reviews, 2016. **65**: pp. 44-56.

[36] Zhao, B.T., Y.X. Su, and W.W. Tao, *Mass transfer performance of CO2 capture in rotating packed bed: Dimensionless modeling and intelligent prediction.* Applied Energy, 2014. **136**: pp. 132-142.

[37] Pan, S.Y., E.G. Eleazar, E.E. Chang, Y.P. Lin, H. Kim, and P.C. Chiang, *Systematic approach to determination of optimum gas-phase mass transfer rate for high-gravity carbonation process of steelmaking slags in a rotating packed bed.* Applied Energy, 2015. **148**: pp. 23-31.

[38] Yu, C.-H., M.-T. Chen, H. Chen, and C.-S. Tan, *Effects of process configurations for combination of rotating packed bed and packed bed on CO2 capture.* Applied Energy, 2016. **175**: pp. 269-276.

[39] Joel, A.S., M.H. Wang, C. Ramshaw, and E. Oko, *Modelling, simulation and analysis of intensified regenerator for solvent based carbon capture using rotating packed bed technology.* Applied Energy, 2017. **203**: pp. 11-25.

[40] Agarwal, L., V. Pavani, D.P. Rao, and N. Kaistha, *Process Intensification in HiGee Absorption and Distillation: Design Procedure and Applications.* Industrial & Engineering Chemistry Research, 2010. **49**(20): pp. 10046-10058.

[41] Joel, A.S., M.H. Wang, C. Ramshaw, and E. Oko, *Process analysis of intensified absorber for post-combustion* CO_2 *capture through modelling and simulation.* International Journal of Greenhouse Gas Control, 2014. **21**: pp. 91-100.

[42] Chamchan, N., J.-Y. Chang, H.-C. Hsu, J.-L. Kang, D.S.H. Wong, S.-S. Jang, and J.-F. Shen, *Comparison of rotating packed bed and packed bed absorber in pilot plant and model simulation for CO2 capture.* Journal of the Taiwan Institute of Chemical Engineers, 2017. **73**: pp. 20-26.

[43] Sang, L., Y. Luo, G.W. Chu, J.P. Zhang, Y. Xiang, and J.F. Chen, *Liquid flow pattern transition, droplet diameter and size distribution in the cavity zone of a rotating packed bed: A visual study.* Chemical Engineering Science, 2017. **158**: pp. 429-438.

[44] Burns, J.R. and C. Ramshaw, *Process intensification: Visual study of liquid maldistribution in rotating packed beds.* Chemical Engineering Science, 1996. **51**(8): pp. 1347-1352.

[45] Guo, K., F. Guo, Y.D. Feng, J.F. Chen, C. Zheng, and N.C. Gardner, *Synchronous visual and RTD study on liquid flow in rotating packed-bed contactor.* Chemical Engineering Science, 2000. **55**(9): pp. 1699-1706.

[46] Yang, K., G.W. Chu, H.K. Zou, and J.F. Chen, *Visualization of micro-fluid flow in a rotating packed bed using particle image velocimetry method.* Journal of Beijing University of Chemical Technology (Natural Science Edition), 2011. **38**(2): pp. 7-11.

[47] Yang, Y.C., Y. Xiang, G.W. Chu, H.K. Zou, Y. Luo, M. Arowo, and J.F. Chen, *A noninvasive X-ray technique for determination of liquid holdup in a rotating packed bed.* Chemical Engineering Science, 2015. **138**: pp. 244-255.

[48] Yan, Z.Y., C. Lin, and Q. Ruan, *Hydrodynamics in a Rotating Packed Bed. I. A Novel Experimental Method.* Industrial & Engineering Chemistry Research, 2012. **51**(31): pp. 10472-10481.

[49] Guo, K., J.W. Wen, Y. Zhao, Y. Wang, Z.Z. Zhang, Z.X. Li, and Z. Qian, *Optimal Packing of a Rotating Packed Bed for* H_2S *Removal.* Environmental Science & Technology, 2014. **48**(12): pp. 6844-6849.

[50] Luo, Y., Y. Chen, H. Yang, and Y. Wang, *Study on an internally-cooled liquid desiccant dehumidifier with CFD model.* Applied Energy, 2017. **194**: pp. 399-409.

[51] Raynal, L. and A. Royon-Lebeaud, *A multi-scale approach for CFD calculations of gas-liquid flow within large size column equipped with structured packing.* Chemical Engineering Science, 2007. **62**(24): pp. 7196-7204.

[52] Tung, H.H. and R.S.H. Mah, *Modeling Liquid Mass-Transfer in Higee Separation Process.* Chemical Engineering Communications, 1985. **39**(1-6): pp. 147-153.

[53] Munjal, S., M.P. Dudukovic, and P. Ramachandran, *Mass-transfer in rotating packed beds-I. Development of gas-liquid and liquid-solid mass-transfer correlations.* Chemical Engineering Science, 1989. **44**(10): pp. 2245-2256.

[54] Kumar, M.P. and D.P. Rao, *Studies on a High-Gravity Gas-Liquid Contactor.* Industrial & Engineering Chemistry Research, 1990. **29**(5): pp. 917-920.

[55] Basic, A. and M.P. Dudukovic, *Liquid Holdup in Rotating Packed-Beds - Examination of the Film Flow Assumption.* Aiche Journal, 1995. **41**(2): pp. 301-316.

[56] Burns, J.R., J.N. Jamil, and C. Ramshaw, *Process intensification: operating characteristics of rotating packed beds - determination of liquid hold-up for a high-voidage structured packing.* Chemical Engineering Science, 2000. **55**(13): pp. 2401-2415.

[57] Lin, C.C., Y.S. Chen, and H.S. Liu, *Prediction of liquid holdup in countercurrent-flow rotating packed bed.* Chemical Engineering Research & Design, 2000. **78**(A3): pp. 397-403.

[58] Chen, Y.H., C.Y. Chang, W.L. Su, C.C. Chen, C.Y. Chiu, Y.H. Yu, P.C. Chiang, and S.I.M. Chiang, *Modeling ozone contacting process in a rotating packed bed.* Industrial & Engineering Chemistry Research, 2004. **43**(1): pp. 228-236.

[59] Buchanan, J.E., *Holdup in Irrigated Ring-Packed Towers below the Loading Point.* Industrial & Engineering Chemistry Fundamentals, 1967. **6**(3): pp. 400-407.

[60] Buchanan, J.E., *Operating Holdup on Film-Type Packings.* Aiche Journal, 1988. **34**(5): pp. 870-872.

[61] Keyvani, M. and N.C. Gardner, *Operating characteristics of rotating beds.* Chemical Engineering Progress, 1989. **85**(9): pp. 48-52.

[62] Munjal, S., M.P. Dudukovic, and P. Ramachandran, *Mass-Transfer in Rotating Packed-Beds-II. Experimental Results and Comparison with Theory and Gravity Flow.* Chemical Engineering Science, 1989. **44**(10): pp. 2257-2268.

[63] Rajan, S., M. Kumar, M.J. Ansari, D.P. Rao, and N. Kaistha, *Limiting Gas Liquid Flows and Mass Transfer in a Novel Rotating Packed Bed (HiGee).* Industrial & Engineering Chemistry Research, 2011. **50**(2): pp. 986-997.

[64] Yang, K., G.W. Chu, H.K. Zou, B.C. Sun, L. Shao, and J.F. Chen, *Determination of the effective interfacial area in rotating packed bed.* Chemical Engineering Journal, 2011. **168**(3): pp. 1377-1382.

[65] Luo, Y., G.W. Chu, H.K. Zou, F. Wang, Y. Xiang, L. Shao, and J.F. Chen, *Mass Transfer Studies in a Rotating Packed Bed with Novel Rotors: Chemisorption of CO_2.* Industrial & Engineering Chemistry Research, 2012. **51**(26): pp. 9164-9172.

[66] Luo, Y., G.W. Chu, H.K. Zou, Z.Q. Zhao, M.P. Dudukovic, and J.F. Chen, *Gas-Liquid Effective Interfacial Area in a Rotating Packed Bed.* Industrial & Engineering Chemistry Research, 2012. **51**(50): pp. 16320-16325.

[67] Guo, K., Z.Z. Zhang, H.J. Luo, J.X. Dang, and Z. Qian, *An Innovative Approach of the Effective Mass Transfer Area in the Rotating Packed Bed.* Industrial & Engineering Chemistry Research, 2014. **53**(10): pp. 4052-4058.

[68] Onda, K., H. Takeuchi, and Y. Okumoto, *Mass transfer coefficients between gas and liquid phases in packed columns.* Journal of Chemical Engineering of Japan, 1968. **1**(1): pp. 56-62.

[69] Luo, Y., J.Z. Luo, G.W. Chu, Z.Q. Zhao, M. Arowo, and J.F. Chen, *Investigation of effective interfacial area in a rotating packed bed with structured stainless steel wire mesh packing.* Chemical Engineering Science, 2017. **170**: pp. 347-354.

[70] Llerena-Chavez, H. and F. Larachi, *Analysis of flow in rotating packed beds via CFD simulations-Dry pressure drop and gas flow maldistribution.* Chemical Engineering Science, 2009. **64**(9): pp. 2113-2126.

[71] Liu, H.S., C.C. Lin, S.C. Wu, and H.W. Hsu, *Characteristics of a rotating packed bed.* Industrial & Engineering Chemistry Research, 1996. **35**(10): pp. 3590-3596.

[72] Chandra, A., P.S. Goswami, and D.P. Rao, *Characteristics of flow in a rotating packed bed (HIGEE) with split packing.* Industrial & Engineering Chemistry Research, 2005. **44**(11): pp. 4051-4060.

[73] Sandilya, P., D.P. Rao, A. Sharma, and G. Biswas, *Gas-phase mass transfer in a centrifugal contactor.* Industrial & Engineering Chemistry Research, 2001. **40**(1): pp. 384-392.

[74] Zheng, C., K. Guo, Y.D. Feng, C. Yang, and N.C. Gardner, *Pressure drop of centripetal gas flow through rotating beds.* Industrial & Engineering Chemistry Research, 2000. **39**(3): pp. 829-834.

[75] Lin, C.C., T.J. Ho, and W.T. Liu, *Distillation in a rotating packed bed.* Journal of Chemical Engineering of Japan, 2002. **35**(12): pp. 1298-1304.

[76] Li, Y.M., J.B. Ji, Z.C. Xu, G.Q. Wang, X.H. Li, and X.J. Liu, *Pressure Drop Model on Rotating Zigzag Bed as a New High-Gravity Technology.* Industrial & Engineering Chemistry Research, 2013. **52**(12): pp. 4638-4649.

[77] Wu, W., Y. Luo, G.-W. Chu, Y. Liu, H.-K. Zou, and J.-F. Chen, *Gas Flow in a Multiliquid-Inlet Rotating Packed Bed: Three-Dimensional Numerical Simulation and Internal Optimization.* Industrial & Engineering Chemistry Research, 2018. **57**(6): pp. 2031-2040.

[78] Liu, Y., Y. Luo, G.W. Chu, J.Z. Luo, M. Arowo, and J.F. Chen, *3D numerical simulation of a rotating packed bed with structured stainless steel wire mesh packing.* Chemical Engineering Science, 2017. **170**: pp. 365-377.

[79] Yang, Y.C., Y. Xiang, Y.G. Li, G.W. Chu, H.K. Zou, M. Arowo, and J.F. Chen, *3D CFD modelling and optimization of single-phase flow in rotating packed beds.* Canadian Journal of Chemical Engineering, 2015. **93**(6): pp. 1138-1148.

[80] Sheng, M.P., B.C. Sun, F.M. Zhang, G.W. Chu, L.L. Zhang, C.G. Liu, J.F. Chen, and H.K. Zou, *Mass-Transfer Characteristics of the CO2 Absorption Process in a Rotating Packed Bed.* Energy & Fuels, 2016. **30**(5): pp. 4215-4220.

[81] Lewis, W.K. and W.G. Whitman, *Principles of gas absorption.* Industrial and Engineering Chemistry, 1924. **16**: pp. 1215-1220.

[82] Higbie, R., *The rate of absorption of a pure gas into a still liquid during short periods of exposure.* Transactions of the American Institute of Chemical Engineers, 1935. **31**: pp. 365-389.

[83] Danckwerts, P.V., *Significance of Liquid-Film Coefficients in Gas Absorption.* Industrial and Engineering Chemistry, 1951. **43**(6): pp. 1460-1467.

[84] Chen, Y.S., C.C. Lin, and H.S. Liu, *Mass transfer in a rotating packed bed with viscous newtonian and non-Newtonian fluids.* Industrial & Engineering Chemistry Research, 2005. **44**(4): pp. 1043-1051.

[85] Chen, Y.S., C.C. Lin, and H.S. Liu, *Mass transfer in a rotating packed bed with various radii of the bed.* Industrial & Engineering Chemistry Research, 2005. **44**(20): pp. 7868-7875.

[86] Jiao, W.Z., Y.Z. Liu, and G.S. Qi, *Gas Pressure Drop and Mass Transfer Characteristics in a Cross-flow Rotating Packed Bed with Porous Plate Packing.* Industrial & Engineering Chemistry Research, 2010. **49**(8): pp. 3732-3740.

[87] Saha, D., *Prediction of mass transfer coefficient in rotating bed contactor (Higee) using artificial neural network.* Heat and Mass Transfer, 2009. **45**(4): pp. 451-457.

[88] Lashkarbolooki, M., B. Vaferi, and D. Mowla, *Using Artificial Neural Network to Predict the Pressure Drop in a Rotating Packed Bed.* Separation Science and Technology, 2012. **47**(16): pp. 2450-2459.

[89] Kang, J.L., K. Sun, D.S.H. Wong, S.S. Jang, and C.S. Tan, *Modeling studies on absorption of CO2 by monoethanolamine in rotating packed bed.* International Journal of Greenhouse Gas Control, 2014. **25**: pp. 141-150.

[90] Joel, A.S., M.H. Wang, and C. Ramshaw, *Modelling and simulation of intensified absorber for post-combustion* CO_2 *capture using different mass transfer correlations.* Applied Thermal Engineering, 2015. **74**: pp. 47-53.

[91] Shi, X., Y. Xiang, L.X. Wen, and J.F. Chen, *CFD analysis of liquid phase flow in a rotating packed bed reactor.* Chemical Engineering Journal, 2013. **228**: pp. 1040-1049.

[92] Guo, T.Y., X. Shi, G.W. Chu, Y. Xiang, L.X. Wen, and J.F. Chen, *Computational Fluid Dynamics Analysis of the Micromixing Efficiency in a Rotating-Packed-Bed Reactor.* Industrial & Engineering Chemistry Research, 2016. **55**(17): pp. 4856-4866.

[93] Yang, Y.C., Y. Xiang, G.W. Chu, H.K. Zou, B.C. Sun, M. Arowo, and J.F. Chen, *CFD modeling of gas-liquid mass transfer process in a rotating packed bed.* Chemical Engineering Journal, 2016. **294**: pp. 111-121.

[94] Guo, T.Y., K.P. Cheng, L.X. Wen, R. Andersson, and J.F. Chen, *Three-Dimensional Simulation on Liquid Flow in a Rotating Packed Bed Reactor.* Industrial & Engineering Chemistry Research, 2017. **56**(28): pp. 8169-8179.

[95] Attou, A., C. Boyer, and G. Ferschneider, *Modelling of the hydrodynamics of the cocurrent gas-liquid trickle flow through a trickle-bed reactor.* Chemical Engineering Science, 1999. **54**(6): pp. 785-802.

[96] Lappalainen, K., V. Alopaeus, M. Manninen, and J. Aittamaa, *Improved Hydrodynamic Model for Wetting Efficiency, Pressure Drop, and Liquid Holdup in Trickle-Bed Reactors.* Industrial & Engineering Chemistry Research, 2008. **47**(21): pp. 8436-8444.

[97] Iliuta, I., C.F. Petre, and F. Larachi, *Hydrodynamic continuum model for two-phase flow structured-packing-containing columns.* Chemical Engineering Science, 2004. **59**(4): pp. 879-888.

[98] Pham, D.A., Y.I. Lim, H. Jee, E. Ahn, and Y. Jung, *Porous media Eulerian computational fluid dynamics (CFD) model of amine absorber with structured-packing for CO2 removal.* Chemical Engineering Science, 2015. **132**: pp. 259-270.

[99] Kim, J., D.A. Pham, and Y.-I. Lim, *Gas−liquid multiphase computational fluid dynamics (CFD) of amine absorption column with structured-packing for CO2 capture.* Computers & Chemical Engineering, 2016. **88**: pp. 39-49.

[100] Pham, D.A., Y.I. Lim, H. Jee, E. Ahn, and Y. Jung, *Effect of ship tilting and motion on amine absorber with structured-packing for CO2 removal from natural gas.* Aiche Journal, 2015. **61**(12): pp. 4412-4425.

[101] Lu, X., P. Xie, D.B. Ingham, L. Ma, and M. Pourkashanian, *A porous media model for CFD simulations of gas-liquid two-phase flow in rotating packed beds.* Chemical Engineering Science, 2018. **189**: pp. 123-134.

[102] Asendrych, D., P. Niegodajew, and S. Drobniak, *Cfd Modelling of Co2 Capture in a Packed Bed by Chemical Absorption.* Chemical and Process Engineering-Inzynieria Chemiczna I Procesowa, 2013. **34**(2): pp. 269-282.

[103] Singh, R.K., J.E. Galvin, and X. Sun, *Three-dimensional simulation of rivulet and film flows over an inclined plate: Effects of solvent properties and contact angle.* Chemical Engineering Science, 2016. **142**: pp. 244-257.

[104] Sebastia-Saez, D., S. Gu, P. Ranganathan, and K. Papadikis, *Micro-scale CFD modeling of reactive mass transfer in falling liquid films within structured packing materials.* International Journal of Greenhouse Gas Control, 2015. **33**: pp. 40-50.

[105] Sebastia-Saez, D., S. Gu, P. Ranganathan, and K. Papadikis, *3D modeling of hydrodynamics and physical mass transfer characteristics of liquid film flows in structured packing elements.* International Journal of Greenhouse Gas Control, 2013. **19**: pp. 492-502.

[106] Sebastia-Saez, D., S. Gu, P. Ranganathan, and K. Papadikis, *Micro-scale CFD study about the influence of operative parameters on physical mass transfer within structured packing elements.* International Journal of Greenhouse Gas Control, 2014. **28**: pp. 180-188.

[107] Haroun, Y., L. Raynal, and D. Legendre, *Mass transfer and liquid hold-up determination in structured packing by CFD.* Chemical Engineering Science, 2012. **75**: pp. 342-348.

[108] Hosseini, S.M., R. Alizadeh, E. Fatehifar, and A. Alizadehdakhel, *Simulation of gas absorption into string-of-beads liquid flow with chemical reaction.* Heat and Mass Transfer, 2014. **50**(10): pp. 1393-1403.

[109] Galledari, S.A., R. Alizadeh, E. Fatehifar, and E. Soroush, *Simulation of carbon dioxide absorption by monoethanolamine solution in wetted-wire column.* Chemical Engineering and Processing, 2016. **102**: pp. 59-69.

[110] Huang, J.C., M. Li, Z.H. Sun, M.Q. Gong, and J.F. Wu, *Hydrodynamics of Layered Wire Gauze Packing.* Industrial & Engineering Chemistry Research, 2015. **54**(17): pp. 4871-4878.

[111] Szulczewska, B., I. Zbicinski, and A. Gorak, *Liquid flow on structured packing: CFD simulation and experimental study.* Chemical Engineering & Technology, 2003. **26**(5): pp. 580-584.

[112] Sebastia-Saez, D., S. Gu, and P. Ranganathan, *Volume of fluid modeling of the reactive mass transfer of CO2 into aqueous amine solutions in structured packed elements at microscale.* Energy Procedia, 2014. **63**: pp. 1229-1242.

[113] Haroun, Y., L. Raynal, and P. Alix, *Prediction of effective area and liquid hold-up in structured packings by CFD.* Chemical Engineering Research & Design, 2014. **92**(11): pp. 2247-2254.

[114] Haroun, Y., D. Legendre, and L. Raynal, *Direct numerical simulation of reactive absorption in gas-liquid flow on structured packing using interface capturing method.* Chemical Engineering Science, 2010. **65**(1): pp. 351-356.

[115] Wehinger, G.D., J. Peeters, S. Muzaferija, T. Eppinger, and M. Kraume, *Numerical simulation of vertical liquid-film wave dynamics.* Chemical Engineering Science, 2013. **104**: pp. 934-944.

[116] Raynal, L., C. Boyer, and J.P. Ballaguet, *Liquid holdup and pressure drop determination in structured packing with CFD simulations.* Canadian Journal of Chemical Engineering, 2004. **82**(5): pp. 871-879.

[117] Haroun, Y., D. Legendre, and L. Raynal, *Volume of fluid method for interfacial reactive mass transfer: Application to stable liquid film.* Chemical Engineering Science, 2010. **65**(10): pp. 2896-2909.

[118] Haelssig, J.B., A.Y. Tremblay, J. Thibault, and S.G. Etemad, *Direct numerical simulation of interphase heat and mass transfer in multicomponent vapour-liquid flows.* International Journal of Heat and Mass Transfer, 2010. **53**(19-20): pp. 3947-3960.

[119] Sun, B., L. He, B.T. Liu, F. Gu, and C.J. Liu, *A new multi-scale model based on CFD and macroscopic calculation for corrugated structured packing column.* Aiche Journal, 2013. **59**(8): pp. 3119-3130.

[120] Sebastia-Saez, D., S. Gu, P. Ranganathan, and K. Papadikis, *Meso-scale CFD study of the pressure drop, liquid hold-up, interfacial area and mass transfer in structured packing materials.* International Journal of Greenhouse Gas Control, 2015. **42**: pp. 388-399.

[121] Li, Q.S., T. Wang, C.N. Dai, and Z.G. Lei, *Hydrodynamics of novel structured packings: An experimental and multi-scale CFD study.* Chemical Engineering Science, 2016. **143**: pp. 23-35.

[122] Liu, B., Y. Wen, C. Liu, B. Sun, and X. Yuan, *Multiscale Calculation on Perforated Sheet Structured Packing To Predict the Liquid Distribution Based on Computational Fluid Dynamics Simulation.* Industrial & Engineering Chemistry Research, 2016. **55**(28): pp. 7810-7818.

[123] Singh, R.K., J.E. Galvin, and X. Sun, *Multiphase flow studies for microscale hydrodynamics in the structured packed column.* Chemical Engineering Journal, 2018. **353**: pp. 949-963.

[124] Armstrong, L.M., S. Gu, and K.H. Luo, *Dry Pressure Drop Prediction within Montz-pak B1-250.45 Packing with Varied Inclination Angles and Geometries.* Industrial & Engineering Chemistry Research, 2013. **52**(11): pp. 4372-4378.

[125] Hosseini, S.H., S. Shojaee, G. Ahmadi, and M. Zivdar, *Computational fluid dynamics studies of dry and wet pressure drops in structured packings.* Journal of Industrial and Engineering Chemistry, 2012. **18**(4): pp. 1465-1473.

[126] Said, W., M. Nemer, and D. Clodic, *Modeling of dry pressure drop for fully developed gas flow in structured packing using CFD simulations.* Chemical Engineering Science, 2011. **66**(10): pp. 2107-2117.

[127] Larachi, F., C.F. Petre, I. Iliuta, and B. Grandjean, *Tailoring the pressure drop of structured packings through CFD simulations.* Chemical Engineering and Processing, 2003. **42**(7): pp. 535-541.

[128] Tao, W.-Q., *Numerical heat transfer*. 2001, Xi’an Jiaotong University Press, Xi’an.

[129] ANSYS Inc, *Theory Guide of ANSYS Fluent 17.2* 2016.

[130] Hirt, C.W. and B.D. Nichols, *Volume of Fluid (Vof) Method for the Dynamics of Free Boundaries.* Journal of Computational Physics, 1981. **39**(1): pp. 201-225.

[131] Osher, S. and J.A. Sethian, *Fronts Propagating with Curvature-Dependent Speed - Algorithms Based on Hamilton-Jacobi Formulations.* Journal of Computational Physics, 1988. **79**(1): pp. 12-49.

[132] Youngs, D.L., *Time-dependent multi-material flow with large fluid distortion*. Numerical methods for fluid dynamics. Vol. 24. 1982, New York: Academic Press. 273-285.

[133] Brackbill, J.U., D.B. Kothe, and C. Zemach, *A Continuum Method for Modeling Surface-Tension.* Journal of Computational Physics, 1992. **100**(2): pp. 335-354.

[134] Yan, Z.Y., C. Lin, and Q. Ruan, *Dynamics of droplets and mass transfer in a rotating packed bed.* Aiche Journal, 2014. **60**(7): pp. 2705-2723.

[135] Menter, F.R., *Two-equation eddy-viscosity turbulence models for engineering applications.* AIAA journal, 1994. **32**(8): pp. 1598-1605.

[136] Abu-Zahra, M.R.M., L.H.J. Schneiders, J.P.M. Niederer, P.H.M. Feron, and G.F. Versteeg, *CO2 capture from power plants. Part I. A parametric study of the technical-performance based on monoethanolamine.* International Journal of Greenhouse Gas Control, 2007. **1**(1): pp. 37-46.

[137] Amundsen, T.G., L.E. Oi, and D.A. Eimer, *Density and Viscosity of Monoethanolamine plus Water plus Carbon Dioxide from (25 to 80) degrees C.* Journal of Chemical and Engineering Data, 2009. **54**(11): pp. 3096-3100.

[138] Kolodziej, A. and J. Lojewska, *Experimental and modelling study on flow resistance of wire gauzes.* Chemical Engineering and Processing, 2009. **48**(3): pp. 816-822.

[139] Penttila, A., C. Dell'Era, P. Uusi-Kyyny, and V. Alopaeus, *The Henry's law constant of N2O and CO2 in aqueous binary and ternary amine solutions (MEA, DEA, DIPA, MDEA, and AMP).* Fluid Phase Equilibria, 2011. **311**: pp. 59-66.

[140] Hughmark, G.A., *Mass and heat transfer from rigid spheres.* AIChE Journal, 1967. **13**(6): pp. 1219-1221.

[141] Mooney, K.G., M.A. Mintun, K.J. Himmelstein, and V.J. Stella, *Dissolution Kinetics of Carboxylic-Acids .1. Effect of Ph under Unbuffered Conditions.* Journal of Pharmaceutical Sciences, 1981. **70**(1): pp. 13-22.

[142] Jeannot, M.A. and F.F. Cantwell, *Mass transfer characteristics of solvent extraction into a single drop at the tip of a syringe needle.* Analytical Chemistry, 1997. **69**(2): pp. 235-239.

[143] Wegner, K., *Mass Transfer: Theories for Mass Transfer Coefficients*. 2017, Swiss Federal Institute of Technology Zurich.

[144] Wellek, R., R. Brunson, and F. Law, *Enhancement factors for gas‐absorption with second‐order irreversible chemical reaction.* The Canadian Journal of Chemical Engineering, 1978. **56**(2): pp. 181-186.

[145] Snijder, E.D., M.J.M. te Riele, G.F. Versteeg, and W.P.M. van Swaaij, *Diffusion coefficients of several aqueous alkanolamine solutions.* Journal of Chemical & Engineering Data, 1993. **38**(3): pp. 475-480.

[146] Liu, G.B., K.T. Yu, X.G. Yuan, C.J. Liu, and Q.C. Guo, *Simulations of chemical absorption in pilot-scale and industrial-scale packed columns by computational mass transfer.* Chemical Engineering Science, 2006. **61**(19): pp. 6511-6529.

[147] Ma, C.R., F. Pietrucci, and W. Andreoni, *Capture and Release of CO2 in Monoethanolamine Aqueous Solutions: New Insights from First-Principles Reaction Dynamics.* Journal of Chemical Theory and Computation, 2015. **11**(7): pp. 3189-3198.

[148] Versteeg, G.F., L.A.J. Van Dijck, and W.P.M. Van Swaaij, *On the kinetics between CO2 and alkanolamines both in aqueous and non-aqueous solutions. An overview.* Chemical Engineering Communications, 1996. **144**: pp. 113-158.

[149] Mishra, D.P., *Simulation of carbon dioxide-monoethanolamine-water system using equilibrium approach*. 2014.

[150] Chen, Y.S., F.Y. Lin, C.C. Lin, C.Y.D. Tai, and H.S. Liu, *Packing characteristics for mass transfer in a rotating packed bed.* Industrial & Engineering Chemistry Research, 2006. **45**(20): pp. 6846-6853.

[151] Kang, J.L., D.S.H. Wong, S.S. Jang, and C.S. Tan, *A comparison between packed beds and rotating packed beds for CO2 capture using monoethanolamine and dilute aqueous ammonia solutions.* International Journal of Greenhouse Gas Control, 2016. **46**: pp. 228-239.

[152] Zheng, X.H., G.W. Chu, D.J. Kong, Y. Luo, J.P. Zhang, H.K. Zou, L.L. Zhang, and J.F. Chen, *Mass transfer intensification in a rotating packed bed with surface-modified nickel foam packing.* Chemical Engineering Journal, 2016. **285**: pp. 236-242.

[153] Yuan, Y. and T.R. Lee, *Contact angle and wetting properties*, in *Surface science techniques*. 2013, Springer. pp. 3-34.

[154] Lan, H., J.L. Wegener, B.F. Armaly, and J.A. Drallmeier, *Developing Laminar Gravity-Driven Thin Liquid Film Flow Down an Inclined Plane.* Journal of Fluids Engineering-Transactions of the Asme, 2010. **132**(8).

[155] Qi, W.Z., K. Guo, H.D. Ding, D. Li, and C.J. Liu, *Model prediction and optimization of dry pressure drop within Winpak.* Chemical Engineering and Processing, 2017. **118**: pp. 62-70.

[156] Ouyang, Y., H.-K. Zou, X.-Y. Gao, G.-W. Chu, Y. Xiang, and J.-F. Chen, *Computational fluid dynamics modeling of viscous liquid flow characteristics and end effect in rotating packed bed.* Chemical Engineering and Processing: Process Intensification, 2018. **123**: pp. 185-194.

[157] Jassim, M.S., *Process Intensification: Absorption and Desorption of Carbon Dioxide from Monoethanolamine Solutions Using Higee Technology*. PhD Thesis Newcastle University, 2002.

[158] Smith, D., C. Graciano, and G. Martinez, *Recent Patents on Expanded Metal.* Recent Patents on Materials Science, 2009. **2**(3): pp. 209-225.

[159] Nijemeisland, M. and A.G. Dixon, *Comparison of CFD simulations to experiment for convective heat transfer in a gas-solid fixed bed.* Chemical Engineering Journal, 2001. **82**(1-3): pp. 231-246.

[160] Lopes, R.J.G. and R.M. Quinta-Ferreira, *Volume-of-Fluid-Based Model for Multiphase Flow in High-Pressure Trickle-Bed Reactor: Optimization of Numerical Parameters.* Aiche Journal, 2009. **55**(11): pp. 2920-2933.

[161] Xu, Z., W.Q. Sun, Y. Lu, Y.H. Mao, and Y.C. Xie, *Experimental Study of Falling-film Mode Transitions between Horizontal Tubes in CaCl2/Water Absorber.* Journal of Thermal Science, 2014. **23**(4): pp. 338-345.

[162] Ding, H., P. Xie, D. Ingham, L. Ma, and M. Pourkashanian, *Flow behaviour of drop and jet modes of a laminar falling film on horizontal tubes.* International Journal of Heat and Mass Transfer, 2018. **124**: pp. 929-942.

[163] Sebastia-Saez, D., S. Gu, and M. Ramaioli, *Effect of the contact angle on the morphology, residence time distribution and mass transfer into liquid rivulets: A CFD study.* Chemical Engineering Science, 2018. **176**: pp. 356-366.

[164] Zhang, J.P., Y. Luo, G.W. Chu, L. Sang, Y. Liu, L.L. Zhang, and J.F. Chen, *A hydrophobic wire mesh for better liquid dispersion in air.* Chemical Engineering Science, 2017. **170**: pp. 204-212.

[165] Xing, T. and F. Stern, *Factors of Safety for Richardson Extrapolation.* Journal of Fluids Engineering-Transactions of the Asme, 2010. **132**(6).

[166] Xing, T. and F. Stern, *Closure to "Discussion of 'Factors of Safety for Richardson Extrapolation'" (2011, ASME J. Fluids Eng., 133, p. 115501).* Journal of Fluids Engineering-Transactions of the Asme, 2011. **133**(11).

[167] Zhang, J., K. Guo, F. Guo, J. Zhu, and C. Zheng, *Experimental Study about Flow of Liquid in Rotating Packed Bed.* Journal of Chemical Engineering of Chinese University, 2000. **14**(4): pp. 378-381.

[168] Xu, Y.Y., S. Paschke, J.U. Repke, J.Q. Yuan, and G. Wozny, *Computational Approach to Characterize the Mass Transfer between the Counter-Current Gas-Liquid Flow.* Chemical Engineering & Technology, 2009. **32**(8): pp. 1227-1235.

[169] Thiels, M., D.S.H. Wong, C.H. Yu, J.L. Kang, S.S. Jang, and C.S. Tan, *Modelling and Design of Carbon Dioxide Absorption in Rotating Packed Bed and Packed Column.* Ifac Papersonline, 2016. **49**(7): pp. 895-900.

[170] Yang, X., D. Ingham, L. Ma, N. Srinivasan, and M. Pourkashanian, *Ash deposition propensity of coals/blends combustion in boilers: a modeling analysis based on multi-slagging routes.* Proceedings of the Combustion Institute, 2017. **36**(3): pp. 3341-3350.

[171] Uchiyama, K., H. Migita, R. Ohmura, and Y.H. Mori, *Gas absorption into "string-of-beads" liquid flow with chemical reaction: application to carbon dioxide separation.* International Journal of Heat and Mass Transfer, 2003. **46**(3): pp. 457-468.

[172] Lu, X., P. Xie, D.B. Ingham, L. Ma, and M. Pourkashanian, *Modelling of CO2 absorption in a rotating packed bed using an Eulerian porous media approach.* Chemical Engineering Science, 2019. **199**: pp. 302-318.

[173] Lashkarbolooki, M., *A general model for pressure drop prediction across a rotating packed bed.* Separation Science and Technology, 2017. **52**(11): pp. 1843-1851.

[174] Singh, S.P., J.H. Wilson, R.M. Counce, J.F. Villiersfisher, H.L. Jennings, A.J. Lucero, G.D. Reed, R.A. Ashworth, and M.G. Elliott, *Removal of Volatile Organic-Compounds from Groundwater Using a Rotary Air Stripper.* Industrial & Engineering Chemistry Research, 1992. **31**(2): pp. 574-580.